# HYPERSONIC PHONONIC CRYSTAL STRUCTURES FOR INTEGRATED NANO-ELECTROMECHANICAL/OPTOMECHANICAL DEVICES

A Dissertation
Presented to
The Academic Faculty

By

Razi Dehghannasiri

In Partial Fulfillment
of the Requirements for the Degree
Doctor of Philosophy in the
School of Electrical and Computer Engineering

Georgia Institute of Technology

August 2018

**HYPERSONIC PHONONIC CRYSTAL STRUCTURES FOR INTEGRATED NANO-ELECTROMECHANICAL/OPTOMECHANICAL DEVICES**

Approved by:


Professor Ali Adibi, Advisor
School of Electrical and Computer Engineering
*Georgia Institute of Technology*

Professor Stephen E. Ralph
School of Electrical and Computer Engineering
*Georgia Institute of Technology*

Professor F. Levent Degertekin
School of Mechanical Engineering
School of Electrical and Computer Engineering
*Georgia Institute of Technology*

Professor Massimo Ruzzene
School of Aerospace Engineering
School of Mechanical Engineering
*Georgia Institute of Technology*

Professor Gee-Kung Chang
School of Electrical and Computer Engineering
*Georgia Institute of Technology*



Date Approved: May 3, 2018

"Enthusiasm is one of the most powerful engines of success. When you do a thing, do it with all your might. Put your whole soul into it. Stamp it with your own personality. Be active, be energetic, be enthusiastic and faithful, and you will accomplish your object. Nothing great was ever achieved without enthusiasm."

*–Ralph Waldo Emerson*

*To my parents and brother:*

*Atifeh, Hamid, and Roozbeh*

## ACKNOWLEDGEMENTS

First and foremost, I would like to thank my doctoral advisor, Professor Ali Adibi, for giving me the opportunity to join his research group. I am greatly indebted to him for creating a relaxed environment for me with freedom to pursue my research interests and providing his constant support during my PhD at Georgia Tech. His patience and generous support allow me to work on my research without stress and funding restriction and to be courageous to explore new research areas. Ali Adibi is truly a gracious, warm, and knowledgeable person. Many thanks to him for guiding and supporting me through my PhD journey at Georgia Tech.

I would also like to give my special thanks to Dr. Ali Eftekhar for many fruitful and stimulating discussions on developing research ideas and attacking challenges of fabrication and characterization of my devices. I have been always amazed by his breadth of knowledge. His availability, days and nights, weekdays and weekends, for discussion significantly expedited many steps of fabrication and characterization. Many thanks to him for being a good mentor and colleague for me and giving me the starting project on integrated electro-optomechanical resonators.

I was also very fortunate to join the phononics team in the group and work closely with Dr. Reza Pourabolghasem. I would like to give him my special thanks for being a good colleague and mentor. He shared with me all his experience, expertise, and knowledge on phononic crystals, which substantially influenced and enriched my PhD research. I enjoyed the days we worked together on the phononics projects in the lab and cleanroom, and I benefited a lot from every discussion we had–from simulation to fabrication and characterization of phononic crystal devices.

I have enjoyed a lot from the interaction and discussion with former Photonics Research Group (PRG) members, specially Dr. Amir Atabaki, Dr. Farshid Ghasemi, Dr. Payam Alipour, Dr. Hossein Taheri, and Dr. Hesam Moradinejad. Many thanks to them for

sharing their time, knowledge, expertise on fabrication, and life experience with me.

My appreciation also goes to current members of PRG. I would like to begin by thanking soon-to-be Dr. Ahmad Usman, one of my good friends at Georgia Tech, who has been my officemate since the very beginning of my stay at Georgia Tech. I enjoyed every discussion that we had from research-related topics to diverse non-scientific discussion. I also enjoyed the interaction and companionship with Dr. Amir Hosseinia, Hossein Taghinejad, soon-to-be Dr. Hamed Mousavi, Tianren Fan, Iman Taghavi, Ali Eshaghian Dorche, and other members of the group. I am looking forward to seeing you all be successful in your future endeavors.

I would also like to thank my friends in and outside Georgia Tech, particularly Rouhollah Mousavi Iraei and Danial Moeinzadeh. Thank you for the companionship and the good times we spent together.

I would also like to thank all my professors at Georgia Tech and University of Tehran for their dedication, high standard of teaching, and substantial influence on shaping my scientific personality.

Last but definitely not least, I would like to express my deepest gratitude to my dear mom and dad, Atifeh and Hamid, and my dear brother, Roozbeh, who have always supported and encouraged me to move forward and to excel in all my efforts as long as I remember. Words fail to express how grateful I am to have you in my life. This dissertation is heartfully dedicated to you.

*Razi Dehghannasiri*

*Atlanta, Georgia*

*Ordibehesht 1397–May 2018*

## TABLE OF CONTENTS

**Acknowledgments** . . . . . v

**List of Tables** . . . . . x

**List of Figures** . . . . . xi

**Chapter 1: Introduction** . . . . . 1

1.1 Theory of elastic waves in piezoelectric materials . . . . . 3

1.2 Surface acoustic waves . . . . . 6

1.3 Phononic crystals . . . . . 7

1.3.1 Membrane phononic crystals . . . . . 8

1.3.2 Surface phononic crystals . . . . . 10

1.4 Stimulated Brillouin scattering . . . . . 11

1.5 Cavity optomechanics . . . . . 14

**Chapter 2: Hypersonic surface phononic bandgap in CMOS-compatible pillar-based piezoelectric structures on silicon** . . . . . 17

2.1 Phononic material loss in PnC structures: Metallic pillars versus nonmetallic pillars . . . . . 19

2.2 Surface phononic crystal band structure and wideband IDT design . . . . . 20

2.2.1 Elastic wave simulations in surface PnC structures . . . . . 21

2.2.2 Designing wideband surface slanted IDTs . . . . . 24

2.3 Fabrication and experimental results . . . . . 27

**Chapter 3: CMOS-Compatible hypersonic surface phononic waveguides on silicon Chips with piezoelectric excitation . . . . . 34**

3.1 Motivations for the development of surface phononic waveguiding . . . . . 34

3.2 Surface elastic waves on half-space substrates . . . . . 35

3.3 Surface acoustic waveguiding in AlN on Si . . . . . 37

3.4 Surface phononic crystals in AlN on Si . . . . . 40

3.4.1 Surface phononic band structure in pillar-based AlN periodic structures on Si . . . . . 41

3.5 Surface waveguiding in pillar-based AlN-on-Si phononic crystal . . . . . 41

3.5.1 Type 1: line defect created by removing AlN pillars . . . . . 45

3.5.2 Type 2: line defect created by introducing a ridge AlN structure . . 47

**Chapter 4: Integrated mode-gap waveguide-based phononic crystal resonators . 48**

4.1 Proposed resonator structure . . . . . 49

4.2 Design and simulation of the mode-gap resonator . . . . . 52

4.3 High-Q surface phononic crystal resonator . . . . . 55

4.3.1 Designing mode-gap termination in the pillar-based SAW-PnC platform . . . . . 56

4.3.2 Etching AlN PnC devices using FOx hard mask . . . . . 58

**Chapter 5: Stimulated Brillouin scattering in phononic-crystal-assisted silicon nitride waveguides . . . . . 60**

5.1 Theory of stimulated Brillouin scattering . . . . . 60

5.2 Design of the phononic crystal structure . . . . . 63

5.3 Optical forces and SBS gain calculations . . . . . 68

5.4 Fabrication of membrane-based SBS PnC devices . . . . . 75

**Chapter 6: On-chip optomechanical photonic resonators in double-layer silicon platforms . . . . . 77**

6.1 On-chip optomechanical oscillators . . . . . 79

6.1.1 Fabrication of double-layer optomechanical Si devices . . . . . 80

6.1.2 RF characterization of on-chip optomechanical oscillators . . . . . 83

6.2 Wideband-tunable resonators using electrostatic actuation . . . . . 86

6.2.1 Proposed wideband-tunable devices . . . . . 86

6.2.2 Theory and simulations . . . . . 88

**Chapter 7: Epilogue . . . . . 91**

7.1 Brief summary of contributions . . . . . 91

7.2 Future directions . . . . . 92

7.2.1 On-chip surface-based SBS devices . . . . . 93

**References . . . . . 93**

**Vita . . . . . 106**

## LIST OF TABLES


1.1 Elastic and dielectric coefficients of Si with cubic (m3m) symmetry [6]. . . 4

1.2 Elastic, dielectric, and piezoelectric coefficients of AlN with hexagonal (6mm) symmetry [6]. $c_{66}^E$=($c_{11}^E$− $c_{12}^E$)/2. . . . . 4

1.3 Material constants of AlN and Si. [7] . . . . . 5

2.1 Nominal material properties and the level of thermoelastic damping for selected dielectrics and metals [95, 94]. . . . . 19

5.1 Comparison of SBS gain and linear optical loss between different optical structures. . . . . 72

## LIST OF FIGURES

1.1 The phononic spectrum [5]. . . . . 2

1.2 Pictorial representaion of surface acoustic waves [10] propagating in half-space isotropic substrates, so called Rayleigh waves. The amplitude of vibration decays exponentially with distance from the surface. . . . . 6

1.3 Different types of PnCs covering operation frequencies from sound and hypersound waves to heat waves for bulk waves, membrane waves, and surface waves. [42, 27, 43, 32, 44]. . . . . 9

1.4 High-frequency surface PnCs in different platforms. (a) hole-based surface PnCs in lithium niobate [45], (b) hole-based surface PnCs in Si [46], (c) and (d) all dielectric pillar-based surface PnCs in lithium niobate [47, 48], and (e) metallic pillar-based surface PnCs on lithium niobate [17]. . . . . 10

1.5 (a) Dispersion diagram of optical and acoustic modes engaged in backward SBS. (b) Amplitude and phase response of the SBS process showing a narrow-band gain and loss spectrum along with a strong phase variation for an optical signal placing at $\Omega$ (acoustic frequency) away from the optical pump. . . . . 11

1.6 On-chip SBS demonstration in various platforms. (a) Silica micro-wedge-resonators [49], (b) Si nanowires supported by SiN membrane [50], (c) Chalcogenide waveguides [51], (d) photonic crystal fibers [52, 53], (e) partially-undercut Si nanowires [54], and (f) $CaF_2$ crystalline resonators [55]. . . . . 12

1.7 Integrated optical structures for enabling SBS devices. (a) Si nanowire as the building block of waveguides/resonators in the SOI platform. (b) LPCVD SiN nanowire structure on thick SiO2. (c) SBS Si nanowire partially undercut. (d) SBS Si nanowire on a SiN PnC membrane. (e) SBS Si nanowire with supporting arms. . . . . 13

1.8 Different types of optical forces [70] that are utilized for studying optomechanical interactions in microcavities: (a) optical gradient forces, (b) optical electrostrictive forces, and (c) optical radiation pressure. . . . . 15

1.9 A gallery of on-chip optomechanical cavities: (a) Silica microtoroids [71], (b) double-layer SiN microring resonators [72], (c) double-layer silica ring resonators [73], (d) silica microsphere [74], (e) silica spoked-microtoroid [75], and (f) optomechanical crystal cavities [76]. . . . . 16

2.1 (a) Simulated surface phononic band structure of the fabricated SAW-PnC, which is a triangular lattice of cone-like AlN pillars on a (100)-oriented Si substrate (see the schematic of the lattice primitive unit cell in (a)) over the edges of the IBZ. The shaded yellow region specifies the extent of the theoretical complete surface PnBG from 1.6 GHz to 1.74 GHz. The lattice constant (a) (i.e., the distance between the nearest adjacent pillars) of the simulated PnC is 1.4 $\mu$m, and the angle, height, and top radius of the cone (i.e., $r'$) are 80 degrees, 530 nm, and 340 nm, respectively. (b) Displacement profiles of the selected points from the primary dispersion bands of the PnC structure in (a). (c) The acoustic power flow inside the SAW-PnC unit cell corresponding to the points (or modes) specified in (a) and the associated displacement profiles in (b). Little red arrows show the density and direction of the power flow in the mid-plane of the unit cell (i.e., in the plane of $x = 0$ for modes A, B, and C, and in the plane of $y = 0$ for modes D, E, and F). For the modes propagating in the $\Gamma-K$ and $\Gamma-X$ directions, the flow of the acoustic power is along the y- and x-directions, respectively, as seen from (c). . . . . 22

2.2 Simulated surface acoustic wave transmission through the fabricated SAW-PnC along: (a) $\Gamma - K$ (11 layers: $11\times a$) and (b) $\Gamma - X$ (9 layers: $9\times a\sqrt{3}$). 24

2.3 Wideband band-pass SAW filters. (a) Chirped IDTs, and (b) slanted IDTs. . 25

2.4 Optical image of the SAW-PnC device showing a ribbon of the SAW-PnC between a pair of wideband slanted IDTs (emitter and receiver transducers) connected to Cu contact pads. The crossed arrows show the crystallography orientation of (100) silicon substrate with respect to the SAW-PnC. . . . . 26

2.5 Fabricated pillar-based SAW-PnC structures. (a) SEM image of the cross-section of the starting substrate for the SAW-PnCs showing the material stack of 1 $\mu m$ AlN/ 100 $nm$ Mo/ 520 $\mu m$ Si. (b) Zoom-in SEM image of the SAW-PnC shown in Fig. 2.4 for studying SAW-PnBG in the $\Gamma-X$ direction. (c) Tilted SEM image of the cross-section of the SAW-PnC. The cone-like AlN pillars were etched by 530nm using plasma dry etching. (d) SEM image of the cross-section of the slanted IDTs showing 80-nm-thick Al metal strips fabricated on 470-nm-thick AlN after I etched 530 nm of AlN to form the pillars on the substrate. . . . . 28

2.6 AFM measurement of fabricated pillar-based SAW-PnC in Fig. 2.5(c). The inset provides the height variation averaged over three paths highlighted by the white dashed lines, which show that the height of the fabricated pillars is 530 nm. . . . . 29

2.7 $S_{21}$ characterization of the fabricated SAW-PnC. (a) The acoustic response of the three reference slanted IDTs utilized for measuring the surface PnBG. (b) and (c) illustrate the transmission of the reference IDTs with SAW-PnC in between along $\Gamma-X$ and $\Gamma-K$, respectively, as defined in (d). (e) and (f) show the transmission of surface acoustic wave through the surface PnC normalized to the response of the reference IDTs. The transmission drop in (e) and (f) indicates the existence of surface PnBG that considerably attenuates the passing SAW. The dashed line in (d) shows the edge of the calculated directional PnBG along $\Gamma-X$. . . . . 30

2.8 Displacement profiles for modes B, E, and F, as specified in Fig. 2.1, on the central cut perpendicular to the flow of the acoustic power propagating along the $\Gamma-K$ direction (or the y-axis, mode B) and the $\Gamma-X$ direction (or the x-axis, modes E and F). $U_x$, $U_y$, and $U_z$ show mode profiles of vibration along x-, y-, and z-axes, respectively. . . . . 32

3.1 Surface acoustic waveguides with finite lateral spreading created by surface micro-machining. (a) Slot-based structures for high-acoustic-velocity thin-film material deposited on the substrate, (b) ridge-based thin-film structure for low-acoustic-velocity material deposited on the substrate, and (c) ridge structures formed by directly etching the substrate. . . . . 36

3.2 Slowness diagrams for bulk acoustic waves in Si and AlN for $k_z = 0$. The contours show $v^{-1} = k/\omega$ as a function of the angle in (100) plane with respect to [100] direction. The $c$-axis of AlN points in z-direction. . . . . 38

3.3 Phase velocity of confined Rayleigh-like wave inside the slot created in $1\mu$m-thick AlN on (100) Si, normalized to the Rayleigh wave ($v_R$) on Si along the same direction. The slot is along the [100] direction. The insets show the total displacement profile of the Rayleigh-type SAW for selected widths of $5\mu$m, $10\mu$m, and $15\mu$m. . . . . 39

3.4 Surface Phononic band structure of a pillar-based triangular lattice of AlN on Si. The yellow shaded region specifies the range of the complete surface PnBG form 1550 MHz to 1800 MHz. AlN thickness is 1 $\mu$m and pillars' height is 500 nm. The distance between nearest-neighbor pillars is 1.3 $\mu$m. . 42

3.5 (a) Phononic waveguiding by introducing a line-defect along $\Gamma - K$ or y-direction. "d" identifies the spacing between the two PnCs. (b) Top view of the simulated PnC structure (i.e., the half of the structure) with boundary conditions labeled. . . . . 43

3.6 Surface phononic waveguiding in the pillar-based PnC formed by introducing a pillar-free defect (see Fig. 3.5). (a) Dispersion bands of the selected defects for $d/a = \{1, 1.4, 2\}$ (label A: Asymmetric modes and label S: Symmetric modes). (b) and (C) total displacement profiles of the guided modes in the surface phononic waveguide with $d/a = 2$ at $k_y = 0.436(2\pi/a)$ obtained by the symmetric boundary condition ($f = 1745.3$ MHz) and asymmetric boundary conditions ($f = 1833.1$ MHz), respectively. . . . . 44

3.7 Surface phononic waveguiding in the pillar-based PnC formed by introducing a ridge AlN structure. (a) Top-view of the designed ridge structure with the same height as of the pillars of the PnC structure. (b) Dispersion bands of the ridge structure (label A: Asymmetric modes and label S: Symmetric modes). (c) and (d) total displacement profiles of the surface guided modes at $k_y = 0.484(2\pi/a)$ obtained by the symmetric boundary condition ($f = 1819.6$ MHz) and asymmetric boundary conditions ($f = 1725.0$ MHz), respectively. . . . . 46

4.1 Different schemes for PnC resonators. (a) Transversal resonances between two arrays of PnC. (b) Multi-mode waveguide-based resonators without dislocating adjacent unit cells to the waveguide. (c) Single-mode waveguide that is abruptly connected to PnC. (d) Single-mode waveguide that is adiabatically terminated to mode-gap waveguides. . . . . 50

4.2 Schematic of the mode-gap waveguide-based resonators. (a) The mechanism of confinement in mode-gap termination and the frequency ranges the phononic mode is propagating or confined. (b) The acoustic resonance mode with mode-gap termination. . . . . 51

4.3 Unit cell phononic band structure. (a) The composition of the PnC and the dimensions. (b) The band structure of the phononic unit cell on the edges of the irreducible Brillouin zone showing two complete phononic bandgaps at 1.07 GHz and 1.45 GHz. . . . . 52

4.4 (a) The schematic of the waveguide unit cell formed by removing a row of pillars and the vectorial displacement profile of a vibration mode inside the mode-gap region (i.e., point A in (b)). (b) Phononic dispersion of the designed single-mode PnC waveguide and the mode-gap PnC waveguide. The shaded region specifies the range of mode-gap frequencies if the waveguide width $w_i$ varies to $w_f$. The blue dash lines specify the extent of the single-mode range of frequencies for $w_i$. . . . . 53

4.5 Mode-gap phononic resonators at different lengths. (a)-(b) k-domain and real domain of two acoustic resonance modes for the out-of-plane displacement profile shown in (c)-(d) with normalized length of 12 (red curve) and 16 (blue curve) and the same termination profile. . . . . 54

4.6 AlN waveguide structures patterned by FOx and etched in an ICP etching tool. (a) The top-view SEM of the fabricated AlN waveguides. (b) Cross-section of the fabricated AlN waveguides (from top to bottom: FOx/10 nm Cr/AlN/Si). Evaporated Cr was initially used to protect AlN structures in TMAH (TMAH is the developer for FOx). Later, I used ALD $SiO_2$ to protect AlN in TMAH. (c) and (d) show the roughness on the sidewall of the fabricated AlN waveguides. The sidewalls are close to vertical. . . . . 57

4.7 ICP etching of AlN PnC structure using a chromium (Cr) lift-off mask. (a) and (b) show the side-view SEMs from an AlN sample patterned with a Cr mask prior to ICP etching. (c) and (d) provide side SEMs from the AlN sample after 500 nm etching of AlN and removing the residue of Cr in a wet process. . . . . 58

4.8 ICP etching of AlN PnC resonators using the FOx e-beam resist with the thickness of 700 nm. (a) and (b) show the top-view SEMs from an AlN sample patterned with FOx prior to ICP etching. (c) and (d) provide side SEMs from the AlN sample after 500 nm etching of AlN and removing the residue of FOx with BOE. . . . . 59

5.1 Phononic dispersion diagram of a free-standing SiN nanowire. (a) Phononic dispersion bands of a nanowire with ($w$, $h$) = (600, 400) nm and ($E$, $\nu$, $\rho$) = (250 GPa, 0.25, 3100 kg/m$^3$). $E$, $\nu$, and $\rho$ are Young's modulus, Poisson's ratio, and mass density, respectively. The acoustic wavenumber is normalized to "$a$", which is the length of the simulated portion of the waveguide (i.e., $a$ = 500 nm ); Dispersion bands can be classified as Brillouin-like acoustic phonons and Raman-like acoustic phonons based on the starting frequency at $K_m a = 0$. (b) Vibration profiles and propagation direction (i.e., along the y direction) of the acoustic modes of the SiN nanowire at $K_m a = 0.3$ for bands 1–4 and $K_m a = 0.01$ for band 5 in (a). White arrows depict the dominant vibration direction. . . . . 64

5.2 Proposed SiN structure for the SBS interaction. (a) The schematic of the pillar-based SiN waveguide for SBS generation, showing the phononic crystal and the optical ridge waveguide along with the vibration profile of the breathing acoustic mode confined inside the phononic bandgap of the PnC. The PnC is formed by a triangular lattice of SiN pillars standing on a thin SiN membrane. The phononic line defect is designed such that the breathing vibration is maximized inside the optical waveguide. The displacement profile in (a) is at normalized wavenumber $K_m a \approx 0$. (b) Phononic dispersion diagram of a primitive unit cell of the PnC (highlighted in (a)) over an irreducible Brillouin zone (shown in the inset of (b)). The pillars' height, radius, and membrane thickness are ($h/a$, $r/a$, $t/a$)=(0.64, 0.44, 0.16), respectively. . . . . 67

5.3 FSBS gain in SiN nanowires and PnC-assisted SiN waveguides. (a) Variation of the FSBS gain in the SiN nanowire for the acoustic mode shown in (b) as a function of its width (w) for three different heights ($h = 0.3$ $\mu$m, $h = 0.4$ $\mu$m, and $h = 0.45$ $\mu$m). In addition, the FSBS gain for a PnC-assisted waveguide with the total thickness of 400 nm is compared with that of different nanowires. The gain slightly reduces because of the extension of the acoustic waves to the pedestal. (b) The acoustic breathing vibration mode and the electric field of the fundamental TE optical mode (i.e., $TE_1$ whose electric field lies in the plane of the nanowire) used in the simulation of the FSBS gain of nanowires. In addition, the breathing-like acoustic vibration mode inside the PnC-assisted waveguide is depicted, which is a combination of two primary vibrations: breathing and flexural. . 71

5.4 Properties of a SiN nanowire on a membrane without PnC. (a) The cross-section of the nanowire (height = 400 nm and width = 600 nm) on a membrane with the width of $w$ and the height of 80 nm. (b) The breathing-like acoustic modes of the structure shown in (a) at $K_m = 0$ for different membrane widths. The color code for the representation of the acoustic resonances is the "breathing-like parameter". (c) Zoomed version of a resonance mode of the structure in (a) in the region identified by the dashed black square in (b) demonstrating mode-splitting (or avoided crossing) due to the coupling between a breathing-like acoustic branch and other acoustic branches of the structure. (d) The FSBS gain calculated for the closest mode of the structure in (a) to the breathing mode of an ideal nanowire (i.e., the mode with the largest "breathing-like parameter" in (b)) as a function of $w$. . . . . 73

5.5 (a) Etching SiN devices using an RIE recipe [149]. (b) Etching SiN using the developed ICP etching recipe. It clearly shows the sidewalls of the ICP etching are much more vertical compared to the RIE recipe. . . . . 75

5.6 KOH wet releasing of SiN structures on Si after 22 hours in normal temperature at cleanroom. (a) Different SiN devices patterned on Si. (b) Releasing a double-disk SiN structure. (c) and (d) releasing waveguides patterned at different angles with respect to [100] direction. . . . . 76

6.1 An optical microdisk resonator in the double-layer Si platform [156]. The thickness of the top and bottom Si layers are 110 nm that are vertically spaced by a 60-nm $SiO_2$ layer. . . . . 77

6.2 Optomechanical interaction between an (electro)mechanical and optical resonator along with the underlying classical equations. . . . . 78

6.3 Overview of the process flow for the fabrication of the on-chip optomechanical devices in double-layer Si platforms. . . . . 81

6.4 Fabricated double-layer optomechanical devices. SEMs show the devices in step 3 of the process flow (see Fig. 6.3). . . . . 81

6.5 Fabricated double-layer optomechanical cavity after releasing (or partially undercutting the $SiO_2$ interlayer). All SEMs were taken at different angles from a single double-layer optomechanical cavity. . . . . 82

6.6 Characterization setup for the optomechanical oscillation when the input laser power is above the oscillation threshold. . . . . 83

6.7 Lowest-order (standing-wave) flexural resonance modes of a double-layer structure. (a) Out-of-plane displacement profile of several flexural resonance modes in a microdisk double-layer Si resonator with the radius of 4.5$\mu$m. The bottom layer is fixed while the top layer is free to deform. (b) Variation of the resonance frequency of the fundamental flexural resonance mode as a function of the undercut. . . . . 84

6.8 Characterization of an optomechanical double-layer Si microdisk with the radius of 4.5$\mu$m. (a) Optical transmission of the device at low input power, and (b) RF characterization of mechanical resonating mode at input laser power above the oscillation threshold. . . . . 85

6.9 Characterization of an optomechanical double-layer Si microdisk with the radius of 4.5$\mu$m. (a) Linear optical transmission (at low power), and (b) RF characterization of mechanical resonating mode ($P_{i,1} < P_{i,2} < P_{i,3}$). . . . . 85

6.10 An electrostatically actuated wideband tunable optical resonator. (a) The schematic cross section view of the microdisk cavity and the location of the tuning electrodes. The top and bottom Si layers both have 110 nm thickness including a 50 nm pedestal for the bottom layer, with the initial gap of 60 nm. (b) SEM Image of the the fabricated double-layer optomechanical resonator after releasing. (c) and (d) optical and zoom-in SEM of the fabricated double-layer structure along with the electrical pads before releasing. (e) The schematic cross-section of the fabricated structures shown in (c) and (d) . . . . . 87

6.11 (a) and (b): Schematics of the proposed double-layer resonators for wideband tunable optical resonators. (c) and (d): Variation of the optical wavelength (red curve, left axis) and the resonance frequency of the first mechanical flexural mode (green curve, right axis) as a function of the applied voltage between the two Si layers for a double-layer microdisk shown in 6.11(a) and a double-layer microring shown in 6.11(b), respectively. Schematics shown in 6.11(a) and 6.11(b) scaled for clarity in mode-profile demonstrations. . . . . 89

## SUMMARY

All my efforts during the course of my Ph.D. have been devoted to the study of phononic-based devices to gain a deep understanding of their rich physics and to design new phononic devices that overcome the limitations of the previous phononic devices. Some of these major limitations include low efficiency, not being CMOS-compatible, material/structural losses, and difficulty of integration with integrated optics and electronics systems. Overcoming these challenges demands innovations in design and fabrication.

The studied devices in this dissertation aim to enable practical integrated phononic devices, which benefit to the field of integrated optics and micro-electromechanical systems (MEMS) with unprecedented on-chip functionalities. The designed structures were extensively simulated and optimized in terms of key parameters prior to the fabrication.

In particular, I designed, simulated, optimized, and fabricated novel integrated phononic devices that interact with optical modes and/or high-frequency electrical signals. The employed optical modes inside my phononic structures are either the waveguide modes or the resonance modes that are actuating (or *shaking*) the phononic structure by applying the radiation pressure forces to enable novel on-chip radio frequency (RF)-photonic applications. The high-frequency electrical signals, on the other hand, vibrates my phononic structures through the piezoelectric effect and the capacitive actuation to enable new on-chip CMOS-compatible devices with lower losses for RF/optical signal processing.

The fabrication of the presented devices in this dissertation demands expertise in diverse fabrication techniques including electron-beam (e-beam) lithography, optical lithography, alignment, dielectric deposition techniques [atomic layer deposition (ALD), low-pressure chemical vapor deposition (LPCVD), and plasma-enhanced chemical vapor deposition (PECVD)], metalization techniques (sputtering and evaporation), wet and dry etching [reactive-ion etching (RIE) and inductively-coupled plasma(ICP)-RIE], releasing, and scanning electron microscopy (SEM). The fabricated devices have gone through many

rounds of fabrication optimization (specially in e-beam lithography and ICP etching) to maximize their performance.

The studied phononic devices in this dissertation include:

- hypersonic CMOS-compatible surface phononic crystal (PnC) structures with piezoelectric excitation [as detailed in Chapter 2], for enabling low-loss surface acoustic wave waveguides [as studied in Chapter 3] and high-Q surface acoustic resonators [as discussed in Chapter 4] in AlN-on-Si substrates,

- hypersonic membrane PnC devices in SiN substrates for the realization of on-chip stimulated Brillouin scattering devices for microwave photonics applications, with all-optical excitation and detection of the engaged phononic mode [as presented in Chapter 5],

- flexural vibrating structures in an extremely thin Si layer with optical and/or capacitive excitation for RF-photonics as well as high-speed wide-band reconfigurable optical devices [as investigated in Chapter 6].

This dissertation aims to pave the way towards advancing the field of phononics and improving the performance of the existing integrated photonic-phononic devices. I hope this dissertation stimulates new directions and ideas for device designs in the realm of phononics.

# CHAPTER 1
# INTRODUCTION

Much of the remarkable technological advances (from semiconductor to lightwave technology) within the last several decades stem from the understanding of how to manipulate the electrons and the photons. Today our life without cellphones, laptops, and the Internet seems impossible. Phonon—the quanta energy of the mechanical waves—is another elementary particle that exists everywhere around us. The melodious sound of the piano, the tiny ripples generated by throwing a stone to a pond, and the destructive vibrations of seismic waves are just a very few daily examples of the mechanical waves. Although, phononic devices (e.g., $\mu$-disks, $\mu$-cantilevers, etc.) have integrated into commercial devices as radio-frequency (RF) filters and inertial sensors, they are still under intensive research owing to their rich and complex physics. Phononic devices are yet to be explored to perfectly complement the existing technologies and to emerge new technologies.

The field of *phononic crystals* (PnCs) [1, 2, 3]–periodic structures designed to manipulate and tailor the propagation of the acoustic/elastic waves in the bulk materials–has witnessed a growing attention over the last two decades to enable superior phononic devices that are not offered by natural materials. The early research efforts in this field were primarily devoted to the modeling and understanding of the rich physics of PnCs and studying their phononic band structures. Later, with the technological advances in micro/nano-fabrication techniques, fruition in the micro/nano-electromechanical systems (MEMS/NEMS), and along with the intense research in photonic crystals devices [4] (its *optical* counterpart), the interest in PnCs has gained momentum. Many research groups has begun to experimentally study PnCs at (ultra-)high frequencies with the focus on the phononic bandgap. Despite the promising demonstrated PnC platforms, these platforms are limited and not suitable for the practical applications because they are not CMOS-

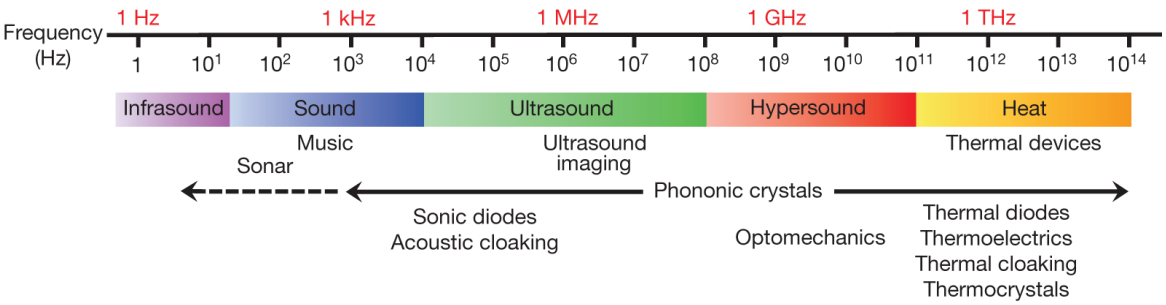


Figure 1.1: The phononic spectrum [5].

compatible (owing to the utilization of crystalline piezoelectric materials) or they incorporate metallic pillar-based structures to form the PnC, which is known to have a high phononic material loss. Therefore, there is still a clear need for developing a high-frequency PnC platform that is CMOS-compatible with low phononic material loss for advanced MEMS/NEMS applications.

The phononic spectrum (shown in Fig. 1.1) covers a wide range of frequencies from the infrasound waves (e.g., seismic waves with a few Hertz frequencies) to the heat waves (with terahertz frequencies). Over such a wide range of frequencies, this dissertation focuses on the study of the integrated PnC devices exhibiting PnBGs at hypersonic regimes (i.e., GHz frequencies) for designing new integrated electromechanical devices (e.g., micro-electromechanical filters integrated with RF electronics circuits) as well as designing novel optomechanical devices which scatter light to other frequencies by the self-induced acoustic waves for new on-chip high-performance RF-photonics applications. In particular, this dissertation covers the theoretical and experimental investigation of the integrated hypersonic surface phononic devices realized in CMOS-compatible aluminum-nitride-on-silicon (AlN-on-Si) platforms and the theoretical investigation of Raman-like stimulated Brillouin scattering in a thin membrane of silicon nitride (SiN) pillar-based PnC. Moreover, the experimental and theoretical investigation of optomechanical interaction in double-layer Si platforms will be also presented in this dissertation. In the remainder of this introductory chapter the main topics of this dissertation are discussed.

## 1.1 Theory of elastic waves in piezoelectric materials

The piezoelectric stress-charge relations that link the second-rank stress (**T**) and strain (**S**) tensors to the first-rank electric field (**E**) and electric displacement field (**D**) are [6]

$$\begin{aligned} \mathbf{T} &= \mathbf{c}^E : \mathbf{S} - \underline{\mathbf{e}} \cdot \mathbf{E} \\ \mathbf{D} &= \mathbf{e} : \mathbf{S} + \epsilon^S \cdot \mathbf{E}, \end{aligned} \tag{1.1}$$

in which, **e** is the third-rank piezoelectric tensor, $\mathbf{c}^E$ and $\epsilon^S$ are the fourth-rank elastic stiffness tensor and second-rank dielectric matrix, respectively, which are measured under the constant electric field and strain. Dot and double dot products in Eqs. (1.1) represent the summation over single subscripts and the pairs of subscripts, respectively. Structural lattice symmetries in the elastic materials allow us to incorporate the abbreviated notation in which the mathematical description of a higher-rank tensor is simplified to a lower-rank matrix. Hence, the relations in Eqs. (1.1) can be rewritten as:

$$\begin{aligned} T_I &= c_{IJ}^E S_J - \underline{e}_{Ij} E_j \\ D_i &= e_{iJ} S_J + \epsilon_{ij}^S E_j, \end{aligned} \tag{1.2}$$

where $I, J = 1, 2, \cdots, 6$ (the Voigt notation) and $i, j = x, y, z$. Also, $\underline{e}_{Ij}$=$e_{jI}$. Tables 1.2 and 1.1 provide the abbreviated representation of all elastic, electrical, and electromechanical coefficients in Si and AlN, respectively. Identical elements due to symmetry has been labeled the same. The values of the relevant (non-zero) coefficients are summarized in Table 1.3.

The coupled equations governing the elastic and electromagnetic waves propagating in a piezoelectric material free of any sources and external forces has been formulated in [6]

Table 1.1: Elastic and dielectric coefficients of Si with cubic (m3m) symmetry [6].

| | $S_1$ | $S_2$ | $S_3$ | $S_4$ | $S_5$ | $S_6$ | $E_x$ | $E_y$ | $E_z$ |
|---|---|---|---|---|---|---|---|---|---|
| $T_1$ | $c_{11}$ | $c_{12}$ | $c_{12}$ | 0 | 0 | 0 | 0 | 0 | 0 |
| $T_2$ | $c_{12}$ | $c_{11}$ | $c_{12}$ | 0 | 0 | 0 | 0 | 0 | 0 |
| $T_3$ | $c_{12}$ | $c_{12}$ | $c_{11}$ | 0 | 0 | 0 | 0 | 0 | 0 |
| $T_4$ | 0 | 0 | 0 | $c_{44}$ | 0 | 0 | 0 | 0 | 0 |
| $T_5$ | 0 | 0 | 0 | 0 | $c_{44}$ | 0 | 0 | 0 | 0 |
| $T_6$ | 0 | 0 | 0 | 0 | 0 | $c_{44}$ | 0 | 0 | 0 |
| $D_x$ | 0 | 0 | 0 | 0 | 0 | 0 | $\epsilon_{xx}$ | 0 | 0 |
| $D_y$ | 0 | 0 | 0 | 0 | 0 | 0 | 0 | $\epsilon_{xx}$ | 0 |
| $D_z$ | 0 | 0 | 0 | 0 | 0 | 0 | 0 | 0 | $\epsilon_{xx}$ |

Table 1.2: Elastic, dielectric, and piezoelectric coefficients of AlN with hexagonal (6mm) symmetry [6]. $c_{66}^E$=($c_{11}^E$– $c_{12}^E$)/2.

| | $S_1$ | $S_2$ | $S_3$ | $S_4$ | $S_5$ | $S_6$ | $E_x$ | $E_y$ | $E_z$ |
|---|---|---|---|---|---|---|---|---|---|
| $T_1$ | $c_{11}^E$ | $c_{12}^E$ | $c_{13}^E$ | 0 | 0 | 0 | 0 | 0 | -$\underline{e}_{1z}$ |
| $T_2$ | $c_{12}^E$ | $c_{11}^E$ | $c_{13}^E$ | 0 | 0 | 0 | 0 | 0 | -$\underline{e}_{1z}$ |
| $T_3$ | $c_{13}^E$ | $c_{13}^E$ | $c_{33}^E$ | 0 | 0 | 0 | 0 | 0 | -$\underline{e}_{3z}$ |
| $T_4$ | 0 | 0 | 0 | $c_{44}^E$ | 0 | 0 | 0 | -$\underline{e}_{5x}$ | 0 |
| $T_5$ | 0 | 0 | 0 | 0 | $c_{44}^E$ | 0 | -$\underline{e}_{5x}$ | 0 | 0 |
| $T_6$ | 0 | 0 | 0 | 0 | 0 | $c_{66}^E$ | 0 | 0 | 0 |
| $D_x$ | 0 | 0 | 0 | 0 | $e_{x5}$ | 0 | $\epsilon_{xx}^S$ | 0 | 0 |
| $D_y$ | 0 | 0 | 0 | $e_{x5}$ | 0 | 0 | 0 | $\epsilon_{xx}^S$ | 0 |
| $D_z$ | $e_{z1}$ | $e_{z1}$ | $e_{z3}$ | 0 | 0 | 0 | 0 | 0 | $\epsilon_{zz}^S$ |

(by incorporating Eqs. 1.1)

$$\begin{aligned} \nabla \cdot \mathbf{c}^E : \nabla_s(\partial_t \mathbf{u}) &= \rho\, \partial_t^3 \mathbf{u} + \nabla \cdot (\underline{\mathbf{e}} \cdot \partial_t \mathbf{E}) \\ -\nabla \times \nabla \times \mathbf{E} &= \mu_0 \epsilon^S \cdot \partial_t^2 \mathbf{E} + \mu_0 \mathbf{e} : \nabla_s \partial_t^2 \mathbf{u}, \end{aligned} \tag{1.3}$$

where $\nabla = \hat{x}\partial_x + \hat{y}\partial_y + \hat{z}\partial_z$, and $(\nabla_s \mathbf{u})_{ij} = S_{ij} = (\partial_i u_j + \partial_j u_i)/2$. $\partial_\beta \alpha = \partial\alpha/\partial\beta$ describes a partial derivative. The constants $\rho$ and $\mu_0$ are the mass density and the free-space permeability, respectively. It is worth mentioning that by setting **e** to zero in Eqs. (1.3), the corresponding propagating elastic and electromagnetic waves equations in the non-piezoelectric elastic materials are obtained. The application of quasi-static approximation (i.e., $\mathbf{E} = -\nabla\Phi$ with $\Phi$ being the electrostatic potential) simplifies the coupled Eqs. (1.3)

Table 1.3: Material constants of AlN and Si. [7]

| | Symbol | AlN | Si |
|---|---|---|---|
| Elastic constants (GPa) | $c_{11}$ | 345 | 166 |
| | $c_{12}$ | 125 | 64 |
| | $c_{13}$ | 120 | 64 |
| | $c_{33}$ | 395 | 166 |
| | $c_{44}$ | 118 | 80 |
| | $c_{66}$ | 110 | 80 |
| Piezoelectric constants ($C/m^2$) | $e_{x5}$ | -0.48 | – |
| | $e_{z1}$ | -0.58 | – |
| | $e_{z3}$ | 1.55 | – |
| Mass density ($kg/m^3$) | $\rho$ | 3260 | 2330 |
| Relative permittivities | $\epsilon_{xx}/\epsilon_0$ | 8 | 11.7 |
| | $\epsilon_{zz}/\epsilon_0$ | 9.5 | 11.7 |

to

$$\begin{aligned} \nabla \cdot \mathbf{c}^E : \nabla_s \mathbf{u} - \rho\, \partial_t^2 \mathbf{u} &= -\nabla \cdot (\underline{\mathbf{e}} \cdot \nabla \Phi), \\ \nabla \cdot (\epsilon^S \cdot \nabla \Phi) &= \nabla \cdot (\mathbf{e} : \nabla_s \mathbf{u}). \end{aligned} \tag{1.4}$$

The coupled Eqs. 1.4 have been used in the literature [8, 9] as the starting point for studying the propagation of the acoustic waves in the piezoelectric materials. In a multi-layer platform, Eqs. 1.4 are solved in each layer (for a non-piezoelectric material **e** is set to zero), then the solution in each layer is matched other layers via the continuity boundary conditions of the electrical and elastic fields. The total stress has to also vanish on stress-free surfaces. Equations (1.4) have been used for extracting the band structure of the piezoelectric pillar-based surface PnCs in this dissertation, which have been implemented using the piezoelectric package in the COMSOL software platform (version 5.2a).

It is worth noting that the presented phononic study throughout this dissertation assumes a small motion (i.e., *elastic motion*). This means that the nonlinear (or quadratic) term of the strain tensor is assumed negligible and any phononic wave-packet can be constructed

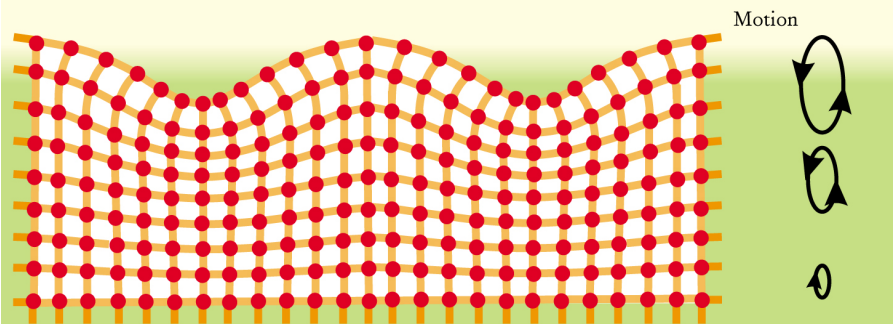


Figure 1.2: Pictorial representaion of surface acoustic waves [10] propagating in half-space isotropic substrates, so called Rayleigh waves. The amplitude of vibration decays exponentially with distance from the surface.

by the superposition of the distinct monochromatic acoustic waves. In other words,

$$S_{ij} = \frac{1}{2}\left(\frac{\partial u_i}{\partial x_j} + \frac{\partial u_j}{\partial x_i} + \frac{\partial u_l}{\partial x_j}\frac{\partial u_l}{\partial x_i}\right) \cong \frac{1}{2}\left(\frac{\partial u_i}{\partial x_j} + \frac{\partial u_j}{\partial x_i}\right) \tag{1.5}$$

where $S_{ij}$ and $u_i$ represent the strain field and displacement vector, respectively, and $x_i$ forms the coordinate systems.

## 1.2 Surface acoustic waves

Surface acoustic waves (SAWs)—a class of acoustic waves confined within a few wavelengths from the surface of a semi-infinite elastic medium—range from the giant seismic waves with kilometer wavelengths on the surface of the Earth [10] to the tiny traveling ripples on the surface of a chip with micron wavelengths [11]. Micro-fabricated SAW-based devices are integral parts of numerous filtering and duplexing applications in wireless communications [11, 12] owing to the ease of surface micro-machining for mass production and the scalability of the operating frequency by adjusting the lateral dimensions. As the working frequency of SAW devices is defined by the surface feature sizes, wireless devices supporting a multitude of spectral bands (e.g., LTE, GPS, Wi-Fi, etc.) can be fabricated by co-integration of SAW devices on a single chip. SAW devices have also been investigated in the quantum studies [13, 14, 15, 16, 17, 18] and in conjunction with the photonic crystal

cavities for the dynamic modulation of the optical signals [19, 20, 21].

On the surface of a homogeneous isotropic elastic solid, a single class of acoustic waves, namely Rayleigh waves [22], is allowed to propagate. This acoustic wave is formed by a mixture of longitudinal and shear vertical bulk acoustic waves (see Fig. 1.2) satisfying the stress-free surface condition of the host solid. The phase velocity of the Rayleigh waves on the surface of the stress-free half-space isotropic substrates is dispersion-less and can be approximated by [6]

$$\frac{v_R}{v_s} = \frac{0.87 + 1.12\sigma}{1 + \sigma}, \tag{1.6}$$

where $\sigma = (1 - 2(v_s/v_l)^2)/(2(1 - (v_s/v_l)^2))$, $v_l$, $v_s$, and $v_R$ denote the Poisson's ratio, longitudinal phase velocity, shear phase velocity, and Rayleigh phase velocity, respectively. As Eq. 1.6 reveals, the phase velocity of Rayleigh waves is always less than that of bulk acoustic waves whose phase velocity is given by $v = \sqrt{c/\rho}$ (where $\rho$ is the mass density, $c = \lambda + 2\mu$ is the stiffness coefficient for longitudinal waves, and $c = \mu$ for shear waves in isotropic materials; $\lambda$ and $\mu$ denote Lam$\acute{e}$ constants). The lower phase velocity of the Rayleigh waves is due to the smaller effective stiffness on the surface compared to the bulk (i.e., $c_{eff} < c_{bulk}$ where $c_{eff} = \rho v_R^2$) [23], which results in the exponential decay of acoustic power density in the direction perpendicular to the surface of the solid.

## 1.3 Phononic crystals

Phononic crystals (PnCs) have attracted a lot of attention due to their ability to harness the propagation of acoustic waves [3, 24]. The periodic structure of the PnCs can result in phononic bandgaps (PnBGs). A complete PnBG is a range of frequencies at which no acoustic mode is allowed to propagate inside the structure at any direction within the Brillouin zone. Even though the majority of early experimental demonstrations of PnC are based on etching a periodic array of holes into the host materials (i.e., hole-based PnCs) [25, 26, 27], a great deal of later research effort has been focused on the pillar-based structures

[28, 29, 30, 31] realized by an array of metallic or dielectric pillars on top of host materials after the seminal work on locally resonant sonic materials [32]. Pillar-based PnCs offer extra design flexibilities (e.g., material and height of pillars) and mitigate the stringent fabrication constraints of wideband PnBGs at GHz frequencies imposed by the hole-based structures [33].

By adding point and line defects to a perfect PnC, PnC resonators [34, 35] and waveguides [36, 37] with unique properties can be created. The possibility of guiding and confining acoustic waves by PnBGs in PnC waveguides and resonators can be used to form more complex integrated phononic devices [38] (e.g., filters and multiplexers), where special attention is dedicated to PnC resonators due to their frequency selective properties. In comparison to conventional micro-electromechanical systems (MEMS)-based resonators [39] (e.g., $\mu$-cantilevers and bulk-mode resonators), PnC resonators offer considerably less support loss (due to utilization of PnBG and elimination of phonons leakage) and thus, potentially higher mechanical Qs. PnC resonators with high Qs have been demonstrated in the membranes on different materials [35, 40, 41]. In addition, PnC resonators can be designed to support only a single resonance frequency without any spurious modes that usually exist in conventional MEMS structures.

### 1.3.1 Membrane phononic crystals

Membrane-based phononic crystals (MPnCs) are attractive because the elastic waves are bounded to the membrane. Therefore, creating a point defect can perfectly confine the elastic waves within the PnBG frequencies in three dimensions (3D) inside the MPnCs mimicking a confinement obtained in 3D PnCs (see e.g., Fig. 1.3(d)) whose fabrication is becoming challenging with increasing the operation frequency. The 3D confinement in MPnCs allows for the fabrication of very high-quality-factor (high-Q) mechanical resonators. This is necessary for forming practical frequency-selective devices with relatively low motional resistance by eliminating anchor losses in the conventional MEMS without

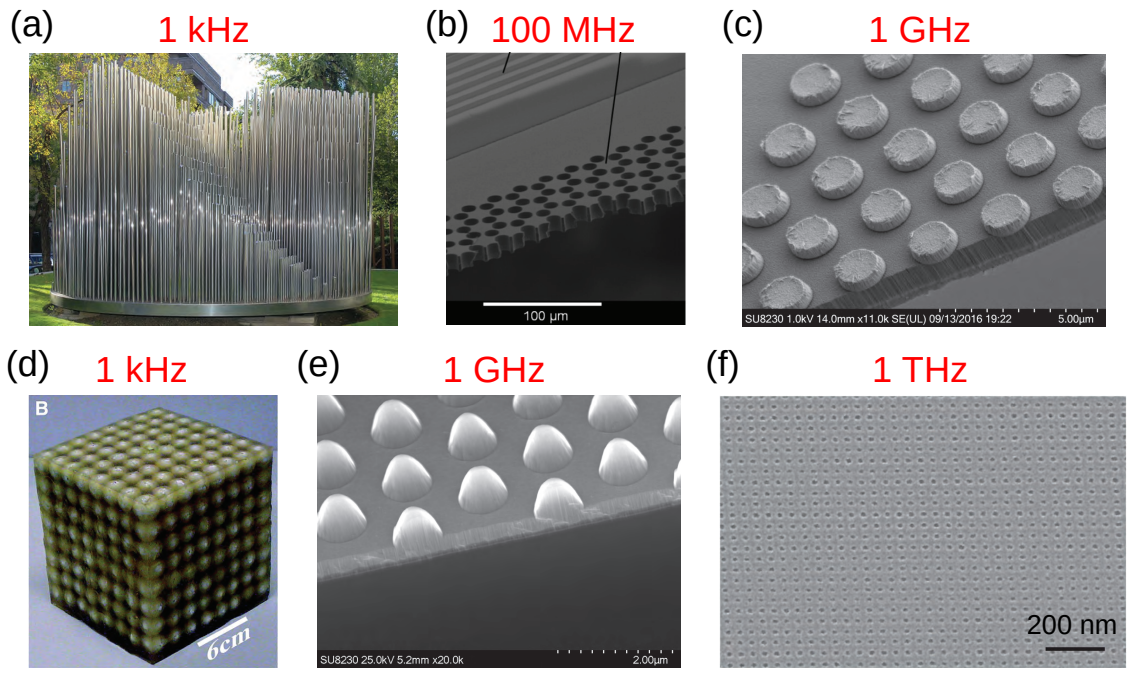


Figure 1.3: Different types of PnCs covering operation frequencies from sound and hypersound waves to heat waves for bulk waves, membrane waves, and surface waves. [42, 27, 43, 32, 44].

sacrificing mechanical stability. The realization of MPnCs is based on forming a periodic lattice of air holes (or inclusions) inside a free-standing membrane [27] or a periodic lattice of metallic pillars on a free-standing membrane [30, 33] as shown in Fig. 1.3(b) and Fig. 1.3(c), respectively. The metallic pillar-based MPnCs are specifically attractive because of : 1) the additional degree of flexibility in design of the MPnCs (i.e., height of pillars in addition to the shape and filling material for the holes or inclusion inside the membrane) that can be used to adjust the PnC properties such as bandgap, 2) the possibility of opening a wider bandgap (with less fabrication constrains as compared to the hole-based MPnCs) by using metals with larger mass density such as nickel ($\rho = 8.9\ g/cm^3$) or tungsten ($\rho = 19.350\ g/cm^3$), and 3) formation of the PnBG through the interplay between the Bragg scattering and the local resonance of the pillars [31], allowing for a richer physics for mode engineering as compared to the hole-based MPnCs. These three distinctions in the metallic pillars-based MPnCs allow for wider PnBGs using less fabrication-constrained geometries.

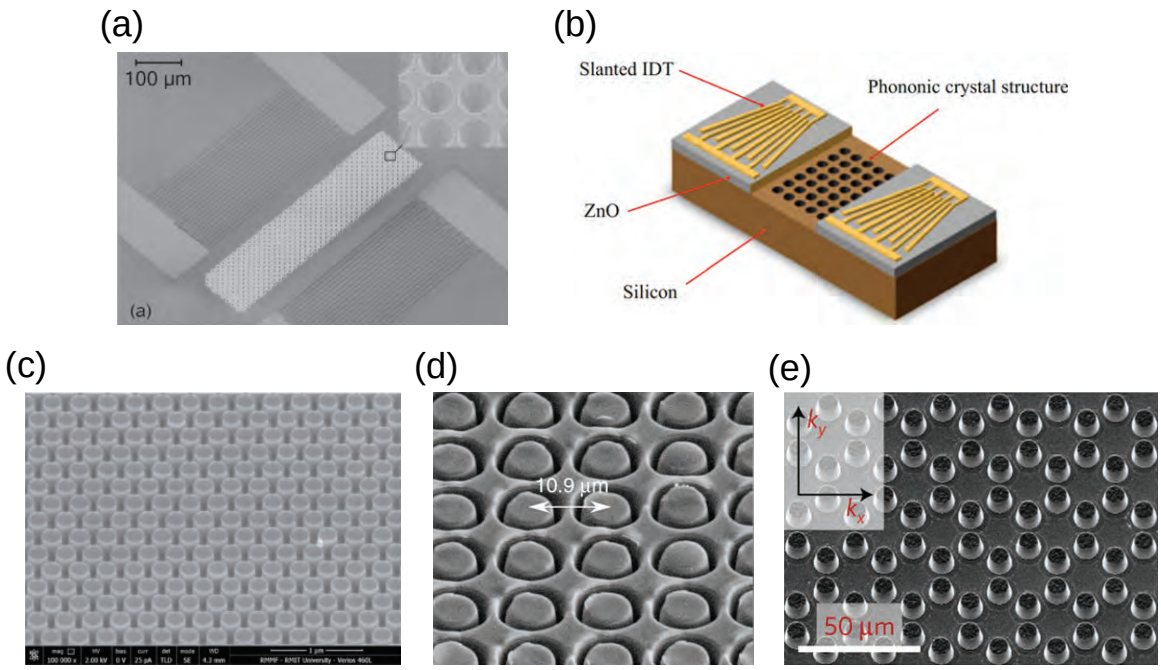


Figure 1.4: High-frequency surface PnCs in different platforms. (a) hole-based surface PnCs in lithium niobate [45], (b) hole-based surface PnCs in Si [46], (c) and (d) all dielectric pillar-based surface PnCs in lithium niobate [47, 48], and (e) metallic pillar-based surface PnCs on lithium niobate [17].

### 1.3.2 Surface phononic crystals

Despite the superior acoustic confinement in MPnC devices, these devices usually require multi steps of fabrications (in particular for active devices), and therefore are less attractive for mass production. A promising alternative to the MPnCs devices is the surface PnCs fabricated on the surface of a substrate, and provide PnBGs for surface acoustic waves (SAWs) that are highly confined to the surface. Surface PnCs are also compatible with the surface-oriented integrated optics and electronics fabrications, which often needs to a few steps of surface micro-machining such as lithography and metalization. However, the acoustic modes inside a surface-PnC-based device may suffer from radiation loss if not designed carefully.

Surface PnCs are realized either by etching a lattice of holes on the surface of a substrate (see Figs. 1.4(a) and 1.4(b)), or fabricating an array of dielectric or metallic pillars

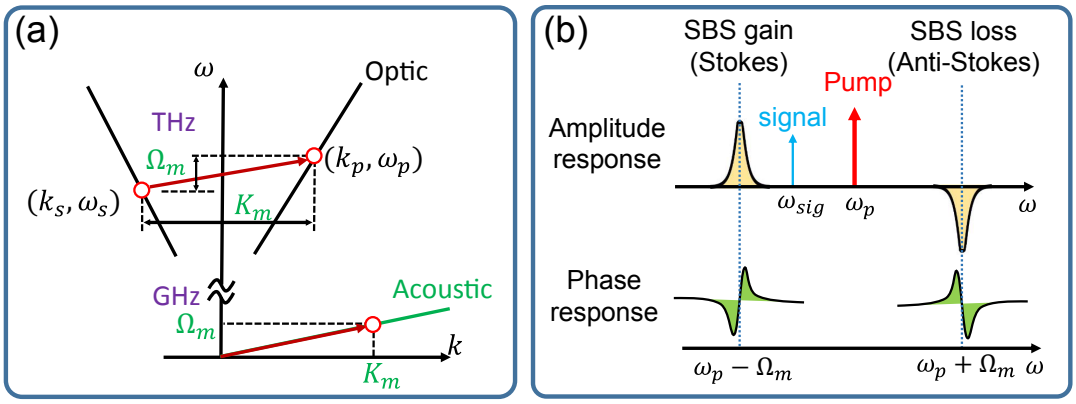


Figure 1.5: (a) Dispersion diagram of optical and acoustic modes engaged in backward SBS. (b) Amplitude and phase response of the SBS process showing a narrow-band gain and loss spectrum along with a strong phase variation for an optical signal placing at Ω (acoustic frequency) away from the optical pump.

on the surface (see Figs. 1.4(c), 1.4(d), and 1.4(e)). Compared to the hole-based surface platforms, the pillar-based platforms have shown a wider PnBG, thanks to the local resonances of the pillars and the additional degrees of freedom allowed in the designing of the surface PnCs (i.e., dimensions and materials of the pillars). Nowadays, most of the surface PnCs are designed in the form of pillar-based structures.

## 1.4 Stimulated Brillouin scattering

Stimulated Brillouin scattering (SBS) is an important nonlinear optical phenomenon based on coherent interaction of two optical waves with an acoustic wave under the phase-matched condition (see Fig. 1.5(a)), inside a properly engineered structure. In SBS, the light passing through a medium fuels an acoustic wave by the optical forces (i.e., the radiation pressure and the electrostrictive forces). If the generated acoustic wave stays confined to the optically active region, it leads to an oscillation in the refractive index and accordingly scatters the incident light to a down-converted frequency.

The prerequisite for the efficiency of this process is the perfect phase matching between two optical waves (i.e., pump and Stokes) and an acoustic wave, that is the conservation of momentum and energy exchange among the waves. Additionally, the structure for SBS

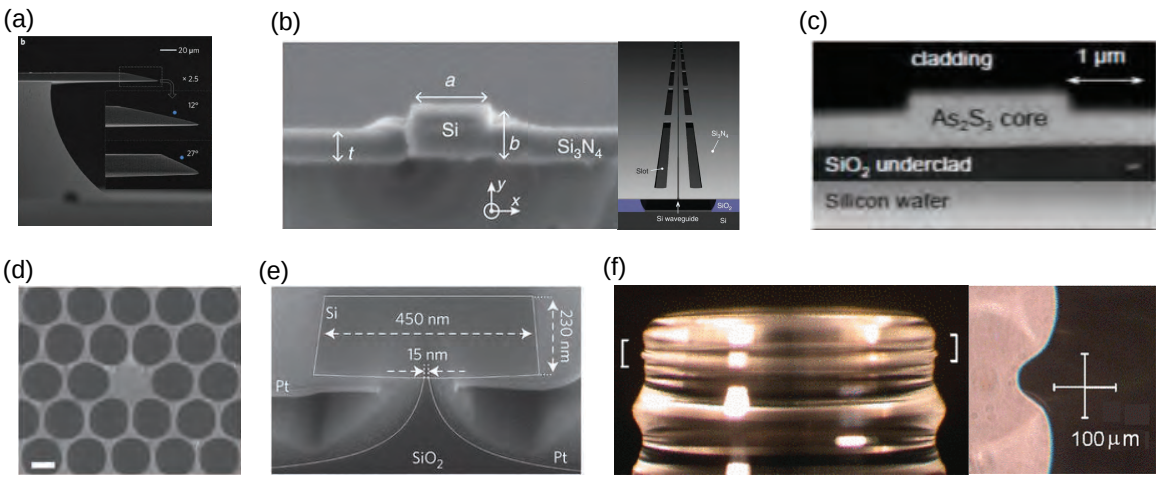


Figure 1.6: On-chip SBS demonstration in various platforms. (a) Silica micro-wedge-resonators [49], (b) Si nanowires supported by SiN membrane [50], (c) Chalcogenide waveguides [51], (d) photonic crystal fibers [52, 53], (e) partially-undercut Si nanowires [54], and (f) $CaF_2$ crystalline resonators [55].

interaction has to be both optically and acoustically low-loss. Figure 1.5(a) shows the dispersion diagram for the phase-matching condition between optical and acoustic waves engaged in a backward SBS (i.e., counter-propagating optical modes) and Fig. 1.5(b) depicts the gain and loss spectrum of an SBS interaction for respectively red-shifted Stokes wave and blue-shifted anti-Stokes wave that can amplify or attenuate a signal.

Although the SBS was initially considered an undesirable phenomena that degrades the integrity of the transmitted optical signal in long-haul fiber optic communications [56, 57], SBS was later investigated in optical fibers to enable several promising applications such as narrow-linewidth lasers [58], inertial sensors [59], non-reciprocal optical devices, and slow light [60], and optical memories [61] thanks to the simultaneous localization of the phase-matched optical and acoustic waves in fibers with very long interaction lengths. More recently, there has been extensive research in extending these promising applications to more chip-scale solutions by using material and device platforms that greatly enhance photon-phonon interactions compared to optical fibers. This has resulted in the formation of SBS-based structures in chalcogenide glasses [51, 62], Si [54, 50, 63], silica [52, 64, 53, 49, 65], and calcium fluoride ($CaF_2$) [55] with reasonably large SBS gains and low

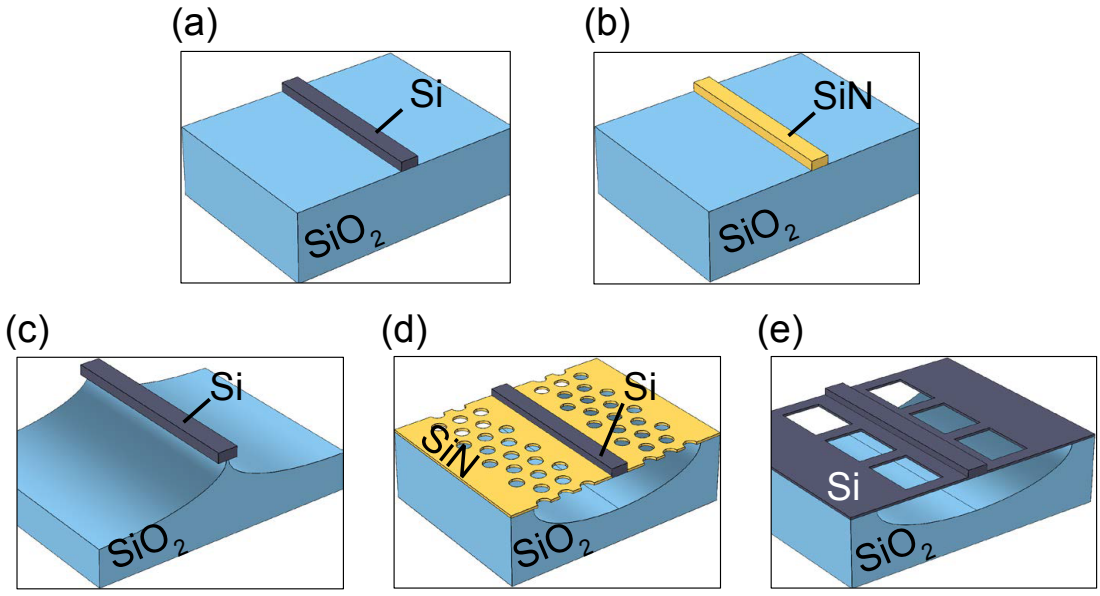


Figure 1.7: Integrated optical structures for enabling SBS devices. (a) Si nanowire as the building block of waveguides/resonators in the SOI platform. (b) LPCVD SiN nanowire structure on thick SiO2. (c) SBS Si nanowire partially undercut. (d) SBS Si nanowire on a SiN PnC membrane. (e) SBS Si nanowire with supporting arms.

threshold powers. However, ultimate on-chip SBS-based systems require compatibility with both integrated optics and electronics platforms and the CMOS fabrication processes. This essentially limits the material platform of choice to a few including Si, SiN, and $SiO_2$.

The major shortcoming of the conventional integrated optics structures (i.e., Figs. 1.7(a) and 1.7(b) ) is their failure to confine acoustic waves inside optical waveguides (or resonators) to facilitate efficient photon-phonon interaction. This is primarily caused by the fact that in sharp contrast to light (which is confined to the Si or SiN waveguides with weak evanescent tails in the underneath $SiO_2$), the acoustic waves tend to be confined in the oxide layer with lower acoustic velocity than that of Si or SiN.

To address this challenge, solutions using Si nanowires have been proposed as depicted in Figs. 1.7(c)-(e) using basic integrated photonic structures in Si-on-insulator (SOI) platform (Fig. 1.7(a)). In these structures, the acoustic waves are confined inside a Si nanowire either by total internal reflection (TIR) inside the structure (Figs. 1.7(c) and 1.7(e)) or by using a membrane-based SiN PnC (Fig 1.7(d)). Despite large optical forces resulting in an

efficient SBS, these Si structures eventually suffer from linear losses (e.g., scattering loss) and nonlinear losses (e.g., two-photon absorption (TPA) and TPA-induced free-carrier absorption) that limit the maximum input optical power and may stifle efficient on-chip SBS generation. On the other hand, SiN is a promising material for SBS due to its relatively large refractive index, wide transparency window, and extremely low optical losses. Wider transparency window in SiN permits SBS interaction at shorter optical wavelengths (not possible in Si and chalcogenide structures) and allows the use of low-noise solid-state lasers at these wavelengths. High-power handling in SiN allows for achieving high SBS gain without clamping by intrinsic nonlinear optical losses. Moreover, recent studies [66] have shown LPCVD SiN is capable of demonstrating extremely low phononic losses due to its intrinsic high-tensile stress. Therefore, the use of SiN nanowires (Fig. 1.7(b)) in conjunction with the SiN PnCs provides a promising platform for the on-chip generation and utilization of the SBS with unprecedented performance in a wide range of wavelengths.

## 1.5 Cavity optomechanics

The first observation of the optomechanical interaction in optical microcavities [67] was unexpectedly happened during the study of the nonlinear optical properties of such cavities [68]. This observation, however, stimulated a surge of interest to explore the rich physics of the so called *dynamical backaction* with the advent of ultra-high-Q optical microcavities [69]. Optomechanical cavities are primarily referred to those deformable structures capable of co-localizing high-Q optical and mechanical resonance modes. In these structures, the mechanical resonance modes (usually in radio frequencies) are excited by an optical force generated from the confided optical resonance modes. Figure 1.8 illustrates the various kinds of optical forces observed in optical microcavities that *shaking* the structure.

In these deformable cavities, the optical path length ($OPL = n_{eff}$L, the product of the effective refractive index and the round-trip length of the cavity) is a function of a me-

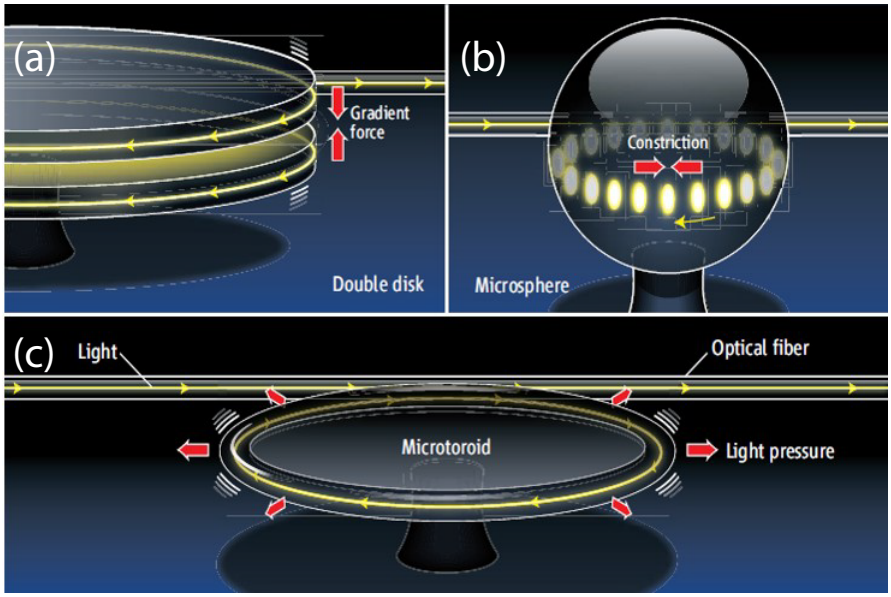


Figure 1.8: Different types of optical forces [70] that are utilized for studying optomechanical interactions in microcavities: (a) optical gradient forces, (b) optical electrostrictive forces, and (c) optical radiation pressure.

chanical degree of freedom ($x$), for instance, through the radius of microdisk, the length of Fabry-Perot cavities, or the vertical gap between the stacked layers in double-layer structures. As a result, the optical resonance frequency ($\omega_{opt}/2\pi$) links to the deformation ($x$) (through the resonance condition: $OPL = m\lambda_{opt}$, m is an integer number) and can be expanded as

$$\omega_{opt}(x) = \omega_{opt,0} + x\partial\omega_{opt}/\partial x + \cdots \approx \omega_{opt,0} + g_{OM}x, \tag{1.7}$$

where $g_{OM} = \partial\omega_{opt}/\partial x$ quantifies the optomechanical interaction and suffices for most experimental optomechanical studies. Therefore, $g_{OM}$ connects the mechanical degree of freedom of the optomechanical cavities to the optical degree of freedom and indicates the strength of coupling.

The interaction of a slightly-detuned resonating optical wave with the mechanical resonance mode results in the modification (or shift) in the mechanical resonance frequency. The vibration of the structure accordingly scattered light and creates optical side-lobes with frequency spacing identical to the mechanical resonance frequency. Dynamical back-

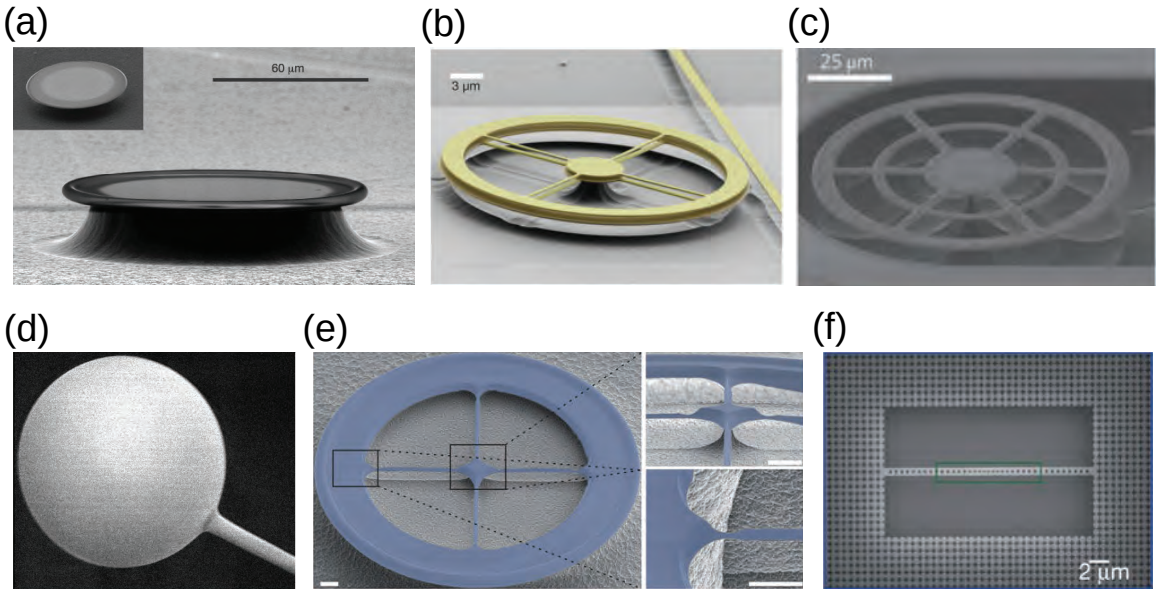


Figure 1.9: A gallery of on-chip optomechanical cavities: (a) Silica microtoroids [71], (b) double-layer SiN microring resonators [72], (c) double-layer silica ring resonators [73], (d) silica microsphere [74], (e) silica spoked-microtoroid [75], and (f) optomechanical crystal cavities [76].

action has been utilized for the demonstration of quantum effects such as laser cooling of a micromechanical object to its ground state [77, 78], squeezing light [79], regenerative oscillation instabilities [80, 81], and inertial sensing [82]. Optomechanical interaction has been investigated in various types of high-Q optical microcavities that support high-Q mechanical resonance modes. Figure 1.9 illustrates such optical microcavities from microtoroids [71] and microspheres [74] to microdisks [73] and nanobeams [83, 76] in material platforms such as silica ($SiO_2$) [71], silicon (Si) [76], and silicon nitride (SiN) [72].

# CHAPTER 2

# HYPERSONIC SURFACE PHONONIC BANDGAP IN CMOS-COMPATIBLE PILLAR-BASED PIEZOELECTRIC STRUCTURES ON SILICON

In this chapter, a new phononic crystal (PnC) platform with wideband hypersonic phononic bandgaps (PnBGs) for surface acoustic waves (SAWs) is demonstrated. These SAW-PnCs are fabricated on a CMOS-compatible substrate and constructed by a two-dimensional periodic array of piezoelectric aluminium nitride (AlN) pillars on silicon (Si) to achieve a lowloss all-dielectric PnC platform. My experimental PnBG results acquired by integrated wideband SAW filters (i.e., two slanted interdigital transducers (IDTs) as an emitter and a receiver) show a surface PnBG from 1.6 GHz to 1.75 GHz for the fabricated surface PnC enabling lowloss hypersonic PnC-based devices for a wide range of ultra-high-frequency applications including wireless communications. Since, the pillars in my platform are non-metallic, they can reduce the overall phononic material loss and enable practical SAW-PnC devices for commercial applications requiring monolithic integration as well as scientific applications seeking for lowloss SAW waveguides and high-quality SAW resonators. Because of the fewer fabrication steps of the proposed SAW-PnC and the selection of the materials (i.e., AlN and Si), the platform is an ideal candidate for SAW devices integrated with CMOS circuits on a single chip for multi-frequency wireless applications. This PnC platform can enable the realization of low-loss surface phononic devices, which is of great importance for next-generation phononic-based filtering circuits.

The ability to control the propagation of SAWs in periodic structures has motivated researchers to extensively investigate SAW-PnCs [84, 25, 85, 86, 26, 46, 45, 87, 88, 89, 90, 91, 47], i.e., artificially-created surface periodic structures supporting a PnBG [1, 2, 92, 3] for SAWs. A complete PnBG is a range of frequencies in which the propagation of acoustic waves in any direction within the defect-free PnC is prohibited. Therefore, similar

to its optical counterpart, i.e., *photonic crystals* [4], introducing an appropriate defect [93, 43] inside a perfect SAW-PnC allows for lowloss localization and navigation of surface acoustic phonons within PnBG frequencies.

SAW-PnCs are created by periodically varying the effective elastic properties (i.e., mass density and stiffness) on the surface of host materials in one or two dimensions (e.g., through ordered synthesization and/or perforation). SAW-PnCs are broadly classified as hole-based SAW-PnCs [25, 26, 46, 45] and pillar-based SAW-PnCs [88, 91, 47]. In comparison to hole-based SAW-PnCs, pillar-based SAW-PnCs are more promising in terms of wider PnBGs in ultrasound (MHz) and hypersound (GHz) regimes with less stringent fabrication constraints thanks to the additional design flexibility in selecting the geometry and material of pillars. PnBGs in pillar-based PnCs [88] stem from the interplay of both Bragg scattering from the periodic phononic structure and local resonances of the individual pillar (i.e., lattice sites). Depending on the frequency of the propagating SAWs in the lattice, pillars can act as either local scatterers or local resonators, which is determined by the geometry and elastic properties of the individual pillar and the global symmetry of the lattice [90].

Previous experimental works on pillar-based SAW-PnCs are mostly based on deposited metallic pillars [88, 91]. These platforms have enabled wideband SAW-PnBGs below the substrate sound line. However, this wideband PnBG is achieved with the price of extra phononic loss of metals for acoustic waves [6, 94]. Therefore, the realization of SAW-PnC devices with wide PnBG and low phononic losses based on non-metallic structures is of great importance.

In this chapter, I present the first report on experimental demonstration of a SAW-PnC based on non-metallic pillars at hypersonic frequencies on a CMOS-compatible piezoelectric platform. Such structures allow for direct integration of SAW-based devices with RF electronics. In the remainder of this chapter, I first discuss dissipation processes in phononic devices and draw a comparison between metallic pillars and dielectric pillars in

Table 2.1: Nominal material properties and the level of thermoelastic damping for selected dielectrics and metals [95, 94].

| Material | Thermal conductivity $\kappa\ [W/(m \cdot K)]$ | Linear thermal expansion $\alpha\ [10^{-6}K^{-1}]$ | Specific heat at constant pressure $C_p[J/(kg \cdot K)]$ | Thermoelastic damping $\gamma \sim \kappa\alpha^2/C_P^2$ |
|---|---|---|---|---|
| Silicon | 120 | 2.6 | 686 | 0.0017 |
| AlN | 70 | 4.5 | 740 | 0.0026 |
| Tungsten | 200 | 5 | 125 | 0.32 |
| Gold | 315 | 14.2 | 129 | 3.8 |
| Nickel | 92 | 13 | 438 | 0.08 |
| Aluminum | 237 | 22.5 | 899 | 0.15 |
| Copper | 400 | 20 | 426 | 0.88 |
| Platinum | 70 | 8.94 | 133 | 0.32 |
| SiC | 70 | 3 | 938 | 0.0007 |

terms of major intrinsic losses. In Sec. 2.2, I describe my design approach for both the SAW-PnC and the input/output IDTs. In Sec. 2.3, I discuss the fabrication process and the experimental characterization results of the fabricated SAW-PnC devices.

## 2.1 Phononic material loss in PnC structures: Metallic pillars versus nonmetallic pillars

The design of a lowloss phononic structure requires mitigation of acoustic loss through different extrinsic and intrinsic processes such as coupling to radiative acoustic modes, thermoelastic damping, phonon-phonon interaction, and phonon-electron scattering [96, 97]. With the suppression of radiation loss (or coupling to bulk modes) in surface PnC structures through appropriate design of PnC defects [93], thermoelastic damping becomes the primary loss mechanism in PnC structures [98, 99, 100, 101, 102, 103]. The thermoelastic damping is caused by the irreversible conversion/coupling of the strain energy to heat due to thermal diffusion. Thermoelastic loss is in general higher in metals [99, 104, 94] due to the larger thermal diffusivity (i.e., $D = \kappa/C_P$, where $\kappa$ and $C_P$ are the thermal conductivity and specific heat capacity at constant pressure, respectively) and larger linear thermal expansion coefficients (i.e., $\alpha = \partial(lnL)/\partial T$). Landau and Lifshitz [101] have shown the

thermoelastic damping generally scales with $\gamma \sim \kappa\alpha^2/C_P^2$. Table 2.1 compares $\gamma$ as an indication of thermoelastic loss in a list of selected dielectric and metallic materials. As it is clear from Table 2.1, metallic materials have much higher thermoelastic damping losses as compared to dielectric materials. In addition, dielectric structures are much less prone to electron-phonon scattering losses [97] as compared to metals. The electron-phonon scattering is one of the major sources of acoustic dissipation for ultrasonic acoustic waves in bulk metals at low temperatures [105, 97]. In addition to the intrinsic losses (i.e., thermoelastic and phonon-electron dissipations) in metals, the friction at metal-piezoelectric interfaces in PnC structures formed by metallic pillars on a piezoelectric substrate also contributes to the overall phononic loss [106, 107]. Similar to the case of metallic-pillar PnCs, the use of metallic electrodes in directly excited PnC structures will lead to increased acoustic losses. Recently, it has been demonstrated that by using capacitive excitation and avoiding direct-contact metallic electrodes in a piezoelectric membrane structure, the mechanical quality factor ($Q_{ph}$) of the membrane structure at 1.2 GHz can be significantly improved [107]. These observations show that the utilization of non-metallic pillars results in surface PnC devices with potentially higher $Q_{ph}$ than those based on metallic-based PnC platforms.

## 2.2 Surface phononic crystal band structure and wideband IDT design

Silicon (Si) is a crystalline substrate suitable for fabricating phononic devices due to the availability of mature fabrication techniques, ease of integration with CMOS electronic circuitry, and low acoustic losses. However, Si is not a piezoelectric material. Thus, a piezoelectric film on Si is required to enable efficient excitation/detection of SAWs through interdigital transducers (IDTs) [108, 11]. Thin-film AlN [109] is a CMOS-compatible material with a very well reproducible deposition [110] that can fulfill the role of an electromechanical transducer while enabling the formation of a surface PnC by patterning it into pillar structures. AlN has, also, recently received attention in piezo-optomechanical studies (e.g., [111, 21, 112]).

### 2.2.1 Elastic wave simulations in surface PnC structures

Radiation loss of SAW-PnC devices (e.g., caused by coupling of surface confined waves to bulk waves) and presence of a PnBG depend on the extent of the non-radiative spectral region, which is set by the slowest bulk mode of the substrates and the PnC lattice symmetries. Among the various two-dimensional lattice structures, the triangular lattice provides the largest non-radiative wavevector extent for a certain lattice constant [90]. Figure 2.1 provides the simulated surface phononic band structure of the cone-like AlN pillars in a triangular lattice on (100)-oriented Si with a primary surface PnBG from 1.6 GHz to 1.74 GHz. As shown in Fig. 2.1(a), the edges of the irreducible Brillouin zone (IBZ) of the PnC structure is $\Gamma$–*X*–*L*–*K*–$\Gamma$ due to the elastic anisotropicity in Si and symmetry of the PnC lattice.

The phononic band structure in Fig. 2.1 is calculated for a primitive unit cell of the SAW-PnC using the finite element method (FEM) in the COMSOL Multiphysics environment. The material constants used in this simulation are listed in Table 1.3. Figure 2.1(a) shows the coordinate axes of the simulation domain, in which the $c$-axis of AlN and Z-axis of the Si stiffness tensor are along the z-axis of the simulation domain, and the X- and Y-axes of the Si stiffness tensor are along the x- and y-axes of the simulation domain, respectively. By applying the Floquet periodic boundary condition to the boundaries of the primitive unit cell perpendicular to the $x-y$ plane and setting the wavenumber ($k_x, k_y \in$ IBZ, $k_z = 0$), I find the corresponding eigen-frequencies and eigen-modes, and extract the band structure of the surface acoustic modes propagating through the lattice in the $x-y$ plane. In Fig. 2.1(a), the thin blue curves denote the confined surface phononic modes of the PnC structure, and the thick red line (i.e., the slowest shear bulk mode) represents the border between the phononic modes well bounded to the surface and the radiative modes (i.e., the bulk modes or leaky surface modes—gray region) not bounded to the surface.

My simulation results reveal that to achieve a wide PnBG, it is critical to have close-to-vertical sidewalls. In addition, simulations show that, for thin AlN pedestals, the PnC lattice

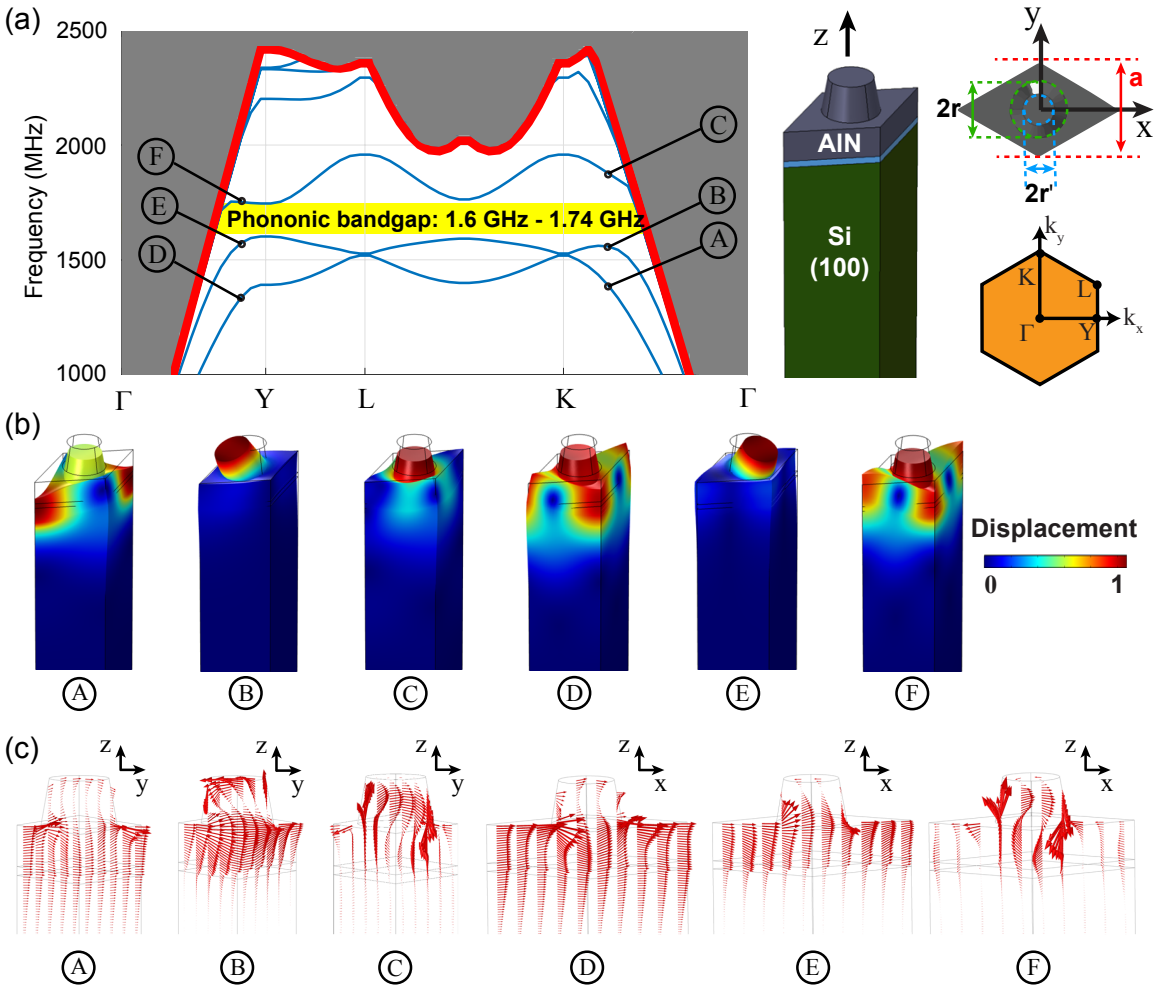


Figure 2.1: (a) Simulated surface phononic band structure of the fabricated SAW-PnC, which is a triangular lattice of cone-like AlN pillars on a (100)-oriented Si substrate (see the schematic of the lattice primitive unit cell in (a)) over the edges of the IBZ. The shaded yellow region specifies the extent of the theoretical complete surface PnBG from 1.6 GHz to 1.74 GHz. The lattice constant (a) (i.e., the distance between the nearest adjacent pillars) of the simulated PnC is 1.4 $\mu$m, and the angle, height, and top radius of the cone (i.e., $r'$) are 80 degrees, 530 nm, and 340 nm, respectively. (b) Displacement profiles of the selected points from the primary dispersion bands of the PnC structure in (a). (c) The acoustic power flow inside the SAW-PnC unit cell corresponding to the points (or modes) specified in (a) and the associated displacement profiles in (b). Little red arrows show the density and direction of the power flow in the mid-plane of the unit cell (i.e., in the plane of $x = 0$ for modes A, B, and C, and in the plane of $y = 0$ for modes D, E, and F). For the modes propagating in the $\Gamma-K$ and $\Gamma-X$ directions, the flow of the acoustic power is along the y- and x-directions, respectively, as seen from (c).

constant (i.e., a) does not play a major role in adjusting the width and center frequency of the first (primary) PnBG. However, as the thickness of the AlN pedestal increases, both the width of the first PnBG and its dependence on the PnC lattice constant increase, indicating that both Bragg scattering and local resonances contribute to the PnBG. Also, at the vicinity of the maximum radius for the pillars, a weak relation between the PnBG and the radius of pillars is observed. To find the optimum structure in terms of the bandgap width, I fixed the angle of the pillars to be 80 degrees as it is determined by the developed fabrication process, the filling fraction (i.e., $\frac{2\pi}{\sqrt{3}}(r/a)^2$) to be between 0.3 and 0.45 (for ease of fabrication), and the total height of the AlN layer (i.e., height of the pillars plus the thickness of the pedestal) to be 1 $\mu$m. Therefore, the optimization parameters reduce to three, namely the height of the pillars, which accordingly sets the thickness of the pedestal, the lattice constant, and the filling fraction (or the pillar radius,$r$). By finely sweeping these parameters, I found that by selecting $a = 1.40\,\mu$m, $r = 430$ nm, and pillar's height $= 530$ nm a wide 0.14 GHz SAW-PnBG centered at 1.67 GHz can be obtained (see Fig. 2.1(a) for definition of the parameters). In this optimization process, the high frequency of the PnBG has been the first priority, and the width of the PnBG has been the secondary criterion. While I kept some parameters fixed (e.g., AlN thickness and pillar angles) to reduce the fabrication complexity, changing these parameters might result in better characteristics (e.g., wider PnBG) at the cost of fabrication complexity. Nevertheless, the simulated PnBG width obtained in my optimization is enough for all practical applications.

To get more insight into the types of surface phononic modes in the PnC structure, I provide in Fig. 2.1(b) the displacement profile of the selected points from the phononic band structure shown in Fig. 2.1(a) for $ak_y = 3.5$ along $\Gamma-K$ and $ak_x = 3.2$ along $\Gamma-X$. Figure 2.1(c) illustrates the density and direction of the acoustic power flow in the PnC unit cell. For the modes in the $\Gamma-K$ and $\Gamma-X$ directions, the flow of the acoustic power is along the y and x directions, respectively, as seen from Fig. 2.1(c). In addition, the higher level of acoustic vibration (or acoustic power flow) in the pillars (as seen from Fig. 2.1(c)) causes

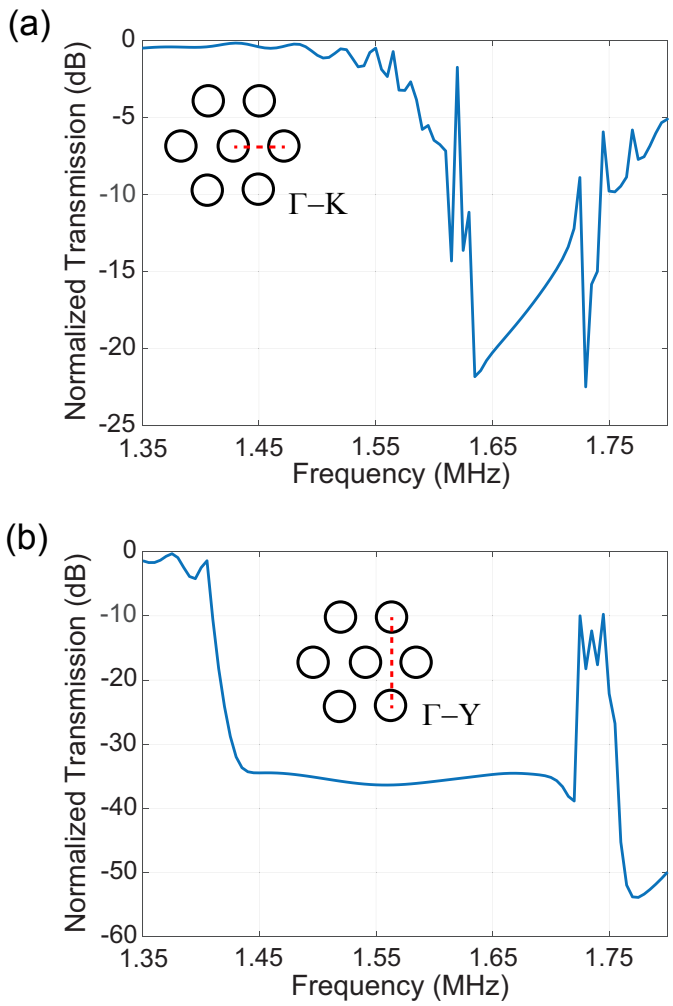


Figure 2.2: Simulated surface acoustic wave transmission through the fabricated SAW-PnC along: (a) $\Gamma - K$ (11 layers: $11\times a$) and (b) $\Gamma - X$ (9 layers: $9\times a\sqrt{3}$).

the corresponding dispersion branches to flatten, which is another indication of the local resonance behavior. In addition, the simulated acoustic transmissions of the SAW-PnC along $\Gamma-K$ and $\Gamma-X$ directions are shown in Figs. 2.2(a) and 2.2(b).

### 2.2.2 Designing wideband surface slanted IDTs

To experimentally demonstrate the predicted large PnBG of the PnC structure, I studied and designed wideband IDTs (or wide-band band-pass SAW filters, see Fig. 2.3). For the realization of wideband IDTs, a chirping is required such that at each frequency only a selected portion of the IDT effectively contributes to the generation and detection of the SAW pro-

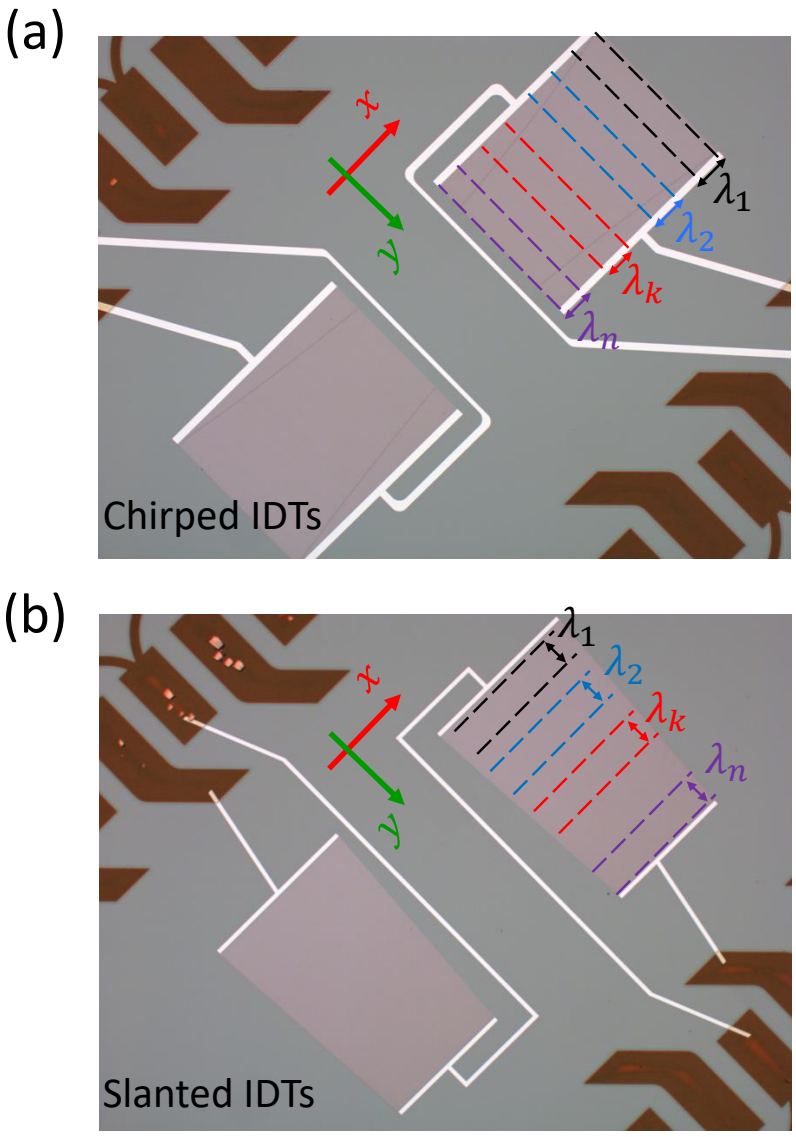


Figure 2.3: Wideband band-pass SAW filters. (a) Chirped IDTs, and (b) slanted IDTs.

vided that its wavelength (or periodicity) matches the wavelength of the emitted/received SAW. Figure 2.3 provides two strategies for designing wideband SAW-IDTs. In Fig. 2.3(a) the introduced chirping is along the direction of SAW radiation (or the x-axis). These IDTs are commonly called in literature [11] as chirped IDTs in which the periodicity of the strips gradually and continuously changes along the x-direction. As a result, a small number of IDTs' period effectively contributes to the launching of the acoustic power at each wavelengths (or frequency). On the other hand, in slanted IDTs (see Fig. 2.3) the chirping is

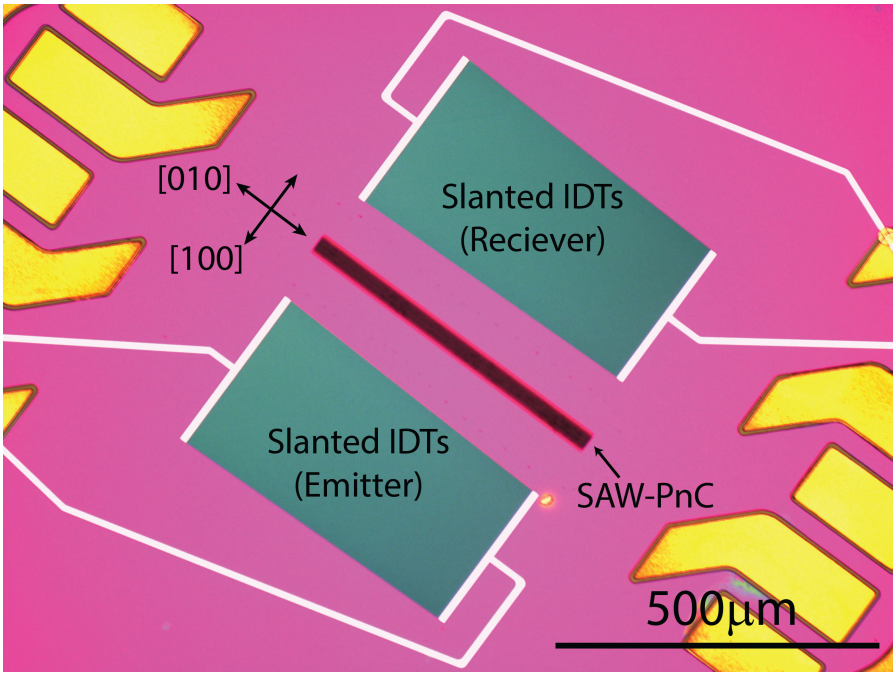


Figure 2.4: Optical image of the SAW-PnC device showing a ribbon of the SAW-PnC between a pair of wideband slanted IDTs (emitter and receiver transducers) connected to Cu contact pads. The crossed arrows show the crystallography orientation of (100) silicon substrate with respect to the SAW-PnC.

across the aperture of the IDTs and whole length of the IDTs assist to the generation and detection of the SAWs. I fabricated both IDTs and slanted IDTs performed better in the characterization and provided a stronger received acoustic signal. Therefore, I used slanted IDTs for the PnBG characterization of the fabricated pillar-based PnC structures.

I designed three wideband slanted IDTs [113, 114, 46], each covering 150 MHz bandwidth in the vicinity of the expected PnBG range. Figure 2.4 shows the optical micrograph of one of the fabricated devices with the slanted excitation and receiver IDTs. The designed wideband slanted IDTs are formed by gradually changing the width of the metal strips and the distance between them across the aperture of IDTs, according to the dispersion (or wavelength) of the Rayleigh-type SAW under the loading of the metal strips. We can imagine the slanted IDTs as many narrow flat-aperture single-frequency IDTs connected in parallel. Advantage of slanted IDTs over the wideband unchirped apodized IDTs and wideband chirped IDTs is their maximum use of the area underneath the IDTs for transduction,

which lowers their input impedance, and launching more acoustic power to each frequency, respectively. To avoid acoustic beam steering and yet obtain a wide fractional bandwidth, I incorporated symmetrical 500-$\mu m$-wide-aperture slanted IDTs and have limited finger-slant angles to $\pm 2$ degrees. It is worth highlighting that in a multi-layer substrate (i.e., a stack of multiple thin-film elastic materials on a semi-infinite substrate), the medium can be single- or multi-mode, depending on the frequency of operation. In my case, I limit my design to the frequency range in which my substrate allows only the fundamental Rayleigh-type SAW emitted by the slanted IDTs.

## 2.3 Fabrication and experimental results

The fabrication of the SAW-PnC devices (Fig. 2.4) can be divided into three key steps: 1) fabricating the AlN pillars, 2) fabricating copper (Cu) contact pads, and 3) fabricating aluminum (Al) IDTs. The cross-section scanning electron microscopy (SEM) image of the starting substrate for the fabrication of the SAW-PnC is shown in Fig. 2.5(a), which is a stack of $1\ \mu m$ AlN / $100\ nm$ molybdenum (Mo) / $520\ \mu m$ Si. AlN is sputtered (by Tegal Corporation) with the $c$-axis perpendicular to the surface of (100)-oriented highly-resistive Si substrates. The high resistivity in Si substrate minimizes the electromagnetic feedthrough coupling between the IDTs, interconnection wiring, and contact pads. Figure 2.4 shows the microscope image of one of the final fabricated SAW devices containing SAW-PnC, slanted IDTs, and contact pads.

I begin the fabrication of the devices by carefully cleaning the sample. I then spin coat MicroChem PMMA positive electron-beam (e-beam) resist on the sample and write the SAW-PnC pattern using a JEOL JBX-9300FS e-beam lithography (EBL) system, at the Georgia Tech institute for electronics and nanotechnology (IEN) facilities, with a 2 nA beam current and 100 kV accelerating voltage. I add the proximity error correction to minimize slight dimension variation throughout the phononic crystal lattice due to the back scattering of electrons during the exposure. After developing PMMA, chromium (Cr) is

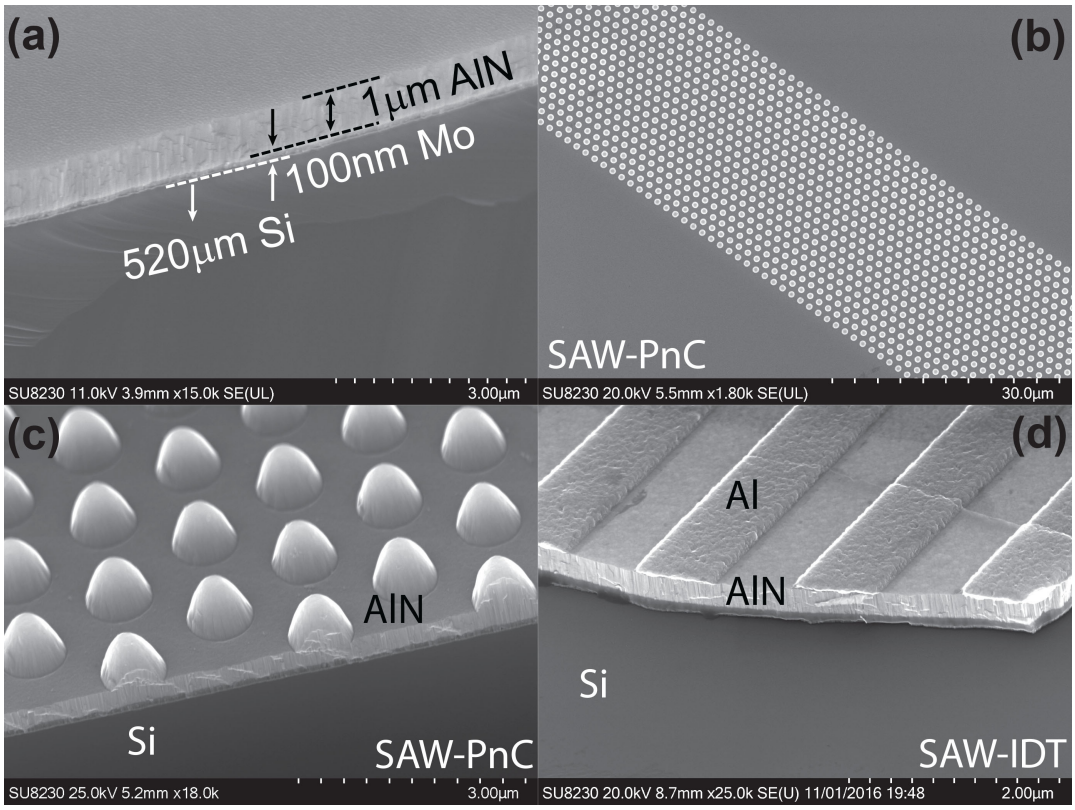


Figure 2.5: Fabricated pillar-based SAW-PnC structures. (a) SEM image of the cross-section of the starting substrate for the SAW-PnCs showing the material stack of 1 $\mu m$ AlN/ 100 $nm$ Mo/ 520 $\mu m$ Si. (b) Zoom-in SEM image of the SAW-PnC shown in Fig. 2.4 for studying SAW-PnBG in the $\Gamma - X$ direction. (c) Tilted SEM image of the cross-section of the SAW-PnC. The cone-like AlN pillars were etched by 530nm using plasma dry etching. (d) SEM image of the cross-section of the slanted IDTs showing 80-nm-thick Al metal strips fabricated on 470-nm-thick AlN after I etched 530 nm of AlN to form the pillars on the substrate.

evaporated and lifted off to create a hard etching mask for the subsequent 530 nm ICP-RIE etching of AlN, which is done using $Cl_2/BCl_3$/Ar chemistry [115]. After forming AlN pillars by partially etching the AlN thin-film, I remove the remaining Cr by wet etching (see Figs. 2.5(b) and 2.5(c)). In the next step, I fabricate Cu contact pads by patterning the sputtered film of 400 nm Cu/10 nm Ti, aligned with AlN pillars, through liftoff process using optical lithography and Microposit SC1813 positive photoresist. After fabricating the contact pads, I fabricate Al IDTs on the 470-nm-thick AlN by first patterning ZEON ZEP-520A positive e-beam resist followed by e-beam evaporation and liftoff of

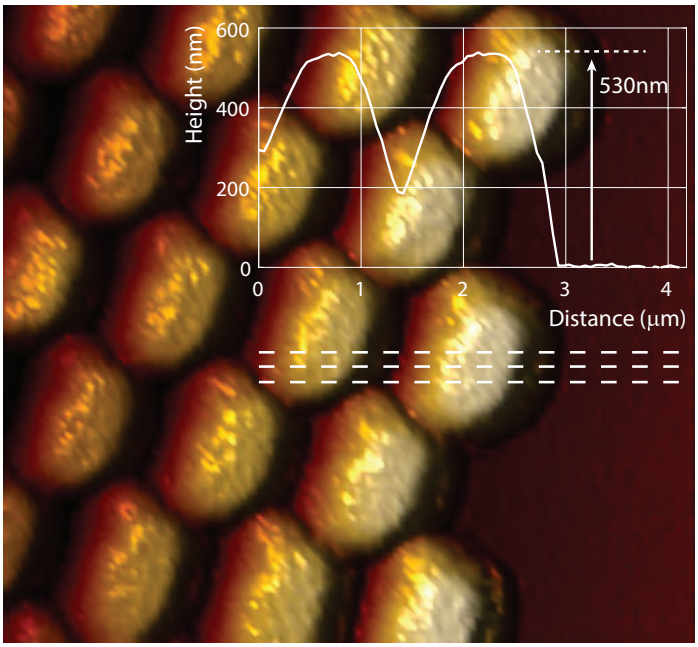


Figure 2.6: AFM measurement of fabricated pillar-based SAW-PnC in Fig. 2.5(c). The inset provides the height variation averaged over three paths highlighted by the white dashed lines, which show that the height of the fabricated pillars is 530 nm.

80 nm Al/5 nm Cr (Fig. 2.5(d)). Figure 2.6 provides atomic force microscopy (AFM) image of the final pillars, which can accurately capture the height of the pillars. However, the pillars in the AFM measurements appear slightly laterally deformed due to the finite width of the AFM tip and limited scanning resolution.

To characterize the fabricated SAW-PnC structures, I used an HP 8753D network analyzer connected to a pair of Infinity Probes from Cascade Microtech to measure the $S_{21}$ parameter (i.e., transmission through the SAW-PnC structure between the emitter and receiver IDTs in Fig. 2.4). The data acquisition is performed with 30 kHz resolution from 1.3 GHz to 1.85 GHz. The raw data obtained from the network analyzer is, in fact, a mixture of electromagnetic and acoustic signals [116]. The electromagnetic contribution comes from the capacitance that forms between input and output interconnects. The electromagnetic feedthrough can be minimized by appropriately shielding or isolating SAW IDTs. To extract the transmitted acoustic signal from the mixed signal, I take an inverse Fourier transform and examine the signal in the time domain. Owing to the difference between

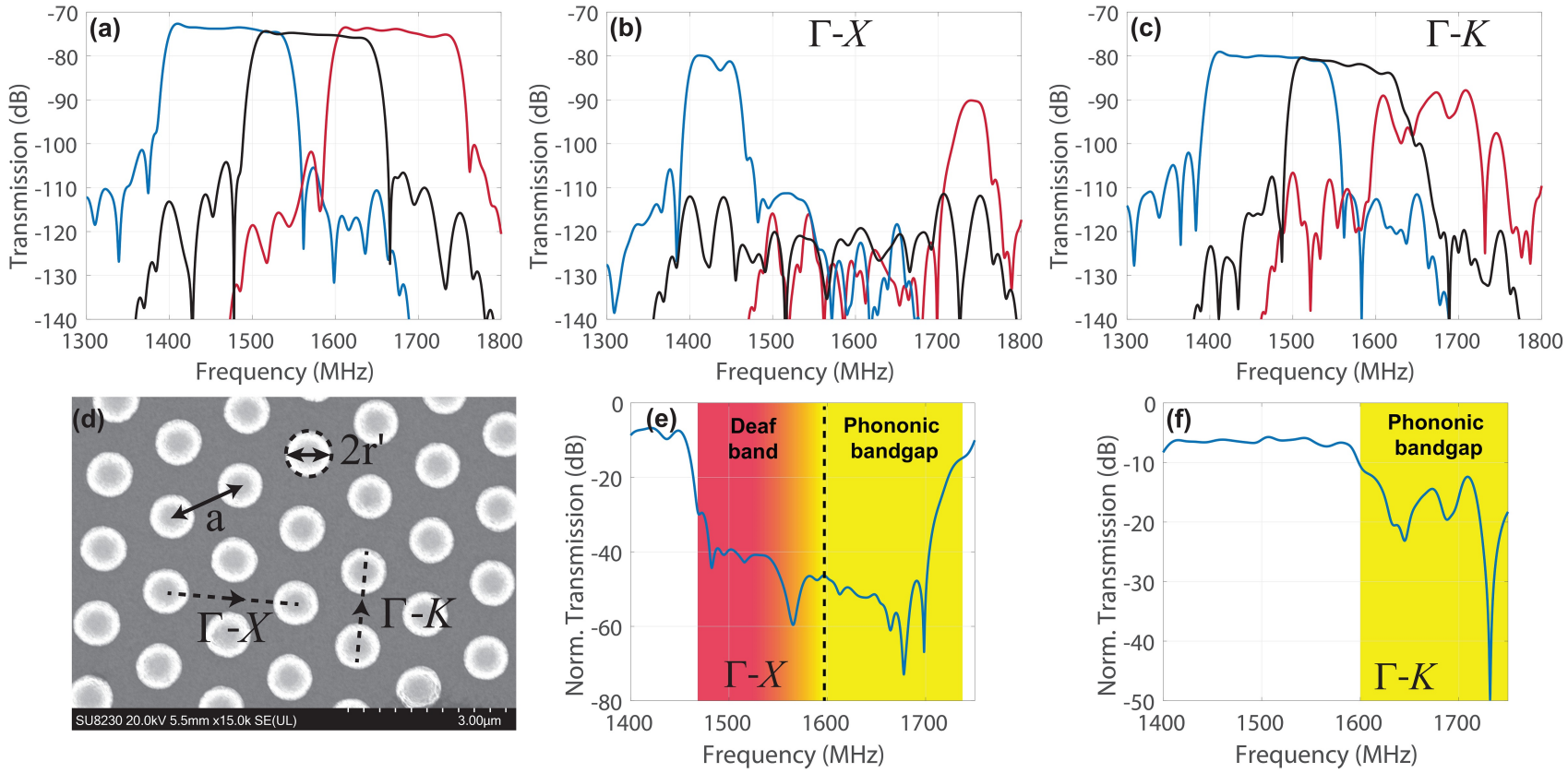


Figure 2.7: $S_{21}$ characterization of the fabricated SAW-PnC. (a) The acoustic response of the three reference slanted IDTs utilized for measuring the surface PnBG. (b) and (c) illustrate the transmission of the reference IDTs with SAW-PnC in between along $\Gamma{-}X$ and $\Gamma{-}K$, respectively, as defined in (d). (e) and (f) show the transmission of surface acoustic wave through the surface PnC normalized to the response of the reference IDTs. The transmission drop in (e) and (f) indicates the existence of surface PnBG that considerably attenuates the passing SAW. The dashed line in (d) shows the edge of the calculated directional PnBG along $\Gamma{-}X$.

the propagation speeds of the electromagnetic waves and the surface acoustic waves, the acoustic portion is well separated from the electromagnetic feedthrough in the time domain. After applying a lossless time-domain filter and taking the Fourier transform, I recover the acoustic signal in the frequency domain.

Plots in Fig. 2.7 provide the acoustic characterization results. In Fig. 2.7(a), I show the acoustic response of three wideband reference IDTs (i.e., the transmission between the input and output IDTs with no SAW-PnC in between) covering 1.4 GHz–1.55 GHz (blue line), 1.5 GHz–1.65 GHz (black line), and 1.6 GHz–1.75 GHz (red line) indicating a dynamic range of better than 50 dB. Transmitted signals are measured along two major crystallographic directions: $\Gamma-X$ (9 PnC periods: $9\times a\sqrt{3}$) and $\Gamma-K$ (14 PnC periods: $14\times a$) (see Fig. 2.7(d) for the definition of the directions). The transmitted acoustic signal detected by the receiver IDTs are depicted in Figs. 2.7(b) and 2.7(c) for the $\Gamma-X$ and $\Gamma-K$ directions, respectively. By normalizing the transmitted acoustic signal to the response of the reference IDTs (i.e., Fig. 2.7(a)), I extract the frequency profile of the attenuation for the transmitted acoustic signal (see Figs. 2.7(e) and 2.7(f)). The frequency ranges corresponding to the directional PnBGs and deaf band [92, 31] (discussed in the next paragraph) are highlighted by the shaded yellow and red regions in Figs. 2.7(e) and 2.7(f). The experimental results reveal at least a 150-MHz-wide PnBG at 1.65 GHz along the $\Gamma-X$ direction. The results of characterization along the $\Gamma-K$ direction, also, reveal at least a 150-MHz-wide PnBG centered at about 1.65 GHz.

It is worth mentioning that the width of the experimental PnBG along $\Gamma-X$ in Fig. 2.7(e) is slightly larger than that of the simulated PnBG predicted by the band structure in Fig.2.1(a), which can be due to the slight geometry difference between the actual fabricated structure and the simulated structure, the material constants incorporated in the simulations, as well as the presence of a deaf band. A deaf band is a frequency range of attenuation in the transmission of acoustic waves through a PnC beyond the actual directional PnBG, and it is caused by poor coupling between the acoustic waves emitted from the SAW IDTs and

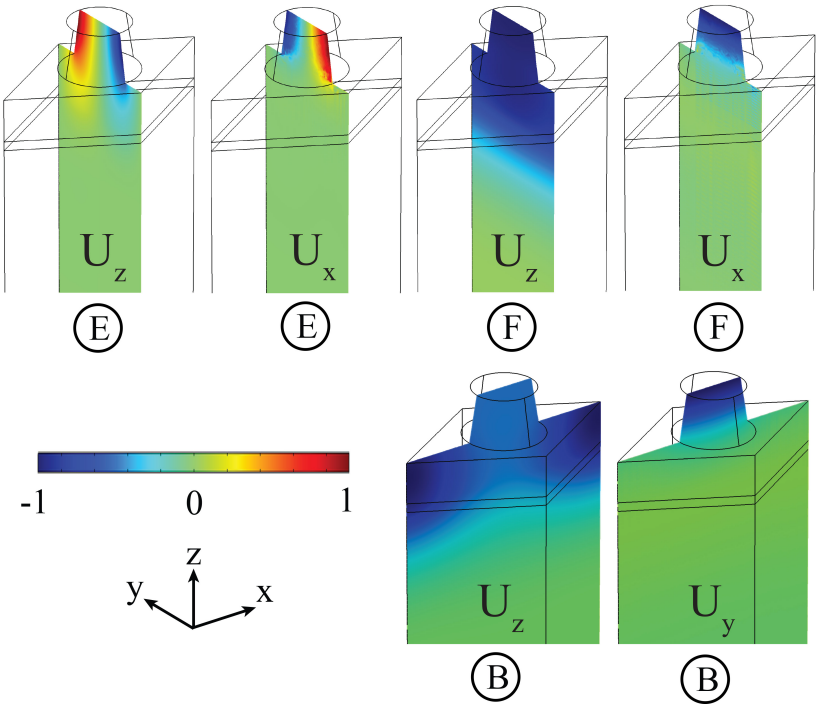


Figure 2.8: Displacement profiles for modes B, E, and F, as specified in Fig. 2.1, on the central cut perpendicular to the flow of the acoustic power propagating along the $\Gamma-K$ direction (or the y-axis, mode B) and the $\Gamma-X$ direction (or the x-axis, modes E and F). $U_x$, $U_y$, and $U_z$ show mode profiles of vibration along x-, y-, and z-axes, respectively.

the phononic modes of the PnC adjacent to the PnBG region because of the impedance (or group velocity) and/or polarization mismatches. Comparing the simulated acoustic transmissions in Fig. 2.1(d) with the experiments in terms of the attenuation bandwidth, I believe the presence of a deaf band is the most likely reason for the slightly larger observed stop band. Figure 2.8 illustrates the mode profiles of points E and F in Fig. 2.1 that are adjacent to the directional PnBG in the $\Gamma-X$ direction. As the displacement profiles of $U_x$ and $U_z$ for the SAW-PnC mode marked by F show, an incident Rayleigh SAW mode in the $\Gamma-X$ direction (i.e., along the x-axis of Fig. 2.8) can couple to this mode because of its vibration resemblance with Rayleigh modes. In addition, the incident Rayleigh SAW whose phase-front lies in the y-z plane (according to the axes in Fig. 2.8) can excite mode F, although with low coupling efficiency. Therefore, the experimental results do not show a deaf band for the upper frequencies of PnBG in the $\Gamma-X$ direction. However, the vibration profile

of the SAW-PnC mode marked by E (see Fig. 2.8) indicates the formation of a deaf band for the frequencies below the directional PnBG in the $\Gamma - X$ direction because of the asymmetric vibration profile of the SAW-PnC mode in the x- and z-directions, as it is verified by the experimental results. In addition, the symmetries of the vibration profile of mode B in z- and y-directions depicted in Fig. 2.8 resemble those of the incident Rayleigh wave emitted from IDTs. Therefore, the deaf band at frequencies below the directional PnBG along $\Gamma - K$ direction is not noticeable. Nevertheless, comparing the results in Fig. 2.1 and Fig. 2.7 show good agreement between simulations and experiments. The results in Fig. 2.7 clearly show the existence of hypersonic PnBGs in SAW-PnCs formed without using metallic pillars. The relatively large PnBG ($10\%$ PnBG width–to–center frequency) enables the formation of functional SAW devices by using line and point defects for many applications including wireless communication filters.

# CHAPTER 3

# CMOS-COMPATIBLE HYPERSONIC SURFACE PHONONIC WAVEGUIDES ON SILICON CHIPS WITH PIEZOELECTRIC EXCITATION

In the previous chapter, I demonstrated a hypersonic phononic bandgap (PnBG) in pillar-based AlN on Si surface phononic crystals (PnCs). This CMOS-compatible platform with its wide PnBG and potentially much lower material loss paves the way for enabling on-chip complex all-phononic signal processing systems consist of surface waveguides and resonators as their Lego pieces. This chapter is dedicated to the design of surface waveguides in AlN on Si with focus on PnC-based structures and the next chapter details the design of a low-loss PnC-based resonator. It is worth noting that the "lowloss" here means the phononic structure supports a PnC mode highly confined inside the introduced line/point defect with minimal coupling to the unguided surface and radiative bulk modes. There are also other sources of loss such as thermoelastic damping (as detailed in Section 2.1) which is not discussed in this chapter.

## 3.1 Motivations for the development of surface phononic waveguiding

The integrated acoustic waveguides and resonators controlling the flow of surface vibrations on the surface of the chips are attractive for a diverse range of applications spanning from micro/nano-electromechanical systems (MEMS/NEMS) [117, 118] to acousto-optic devices [20, 21] and quantum studies [13, 15, 16, 18] owing to: (1) the convenience of surface micro-machining (i.e., a few deposition, etching, or lithography steps) which is fully compatible with surface-oriented integrated optics and electronics fabrications, (2) adjusting their operation frequency by surface feature sizes (essential for multi-frequency devices), (3) the localization of acoustic waves over a fraction of their wavelength near the surface of the chips (beneficial for sensing [119, 120] and nonlinear acoustic [121, 122]

applications), and (4) the ability to excite and detect surface acoustic waves (SAWs) at any point on the surface of the chips. Among these on-chip surface acoustic devices, those structures realized on silicon (Si) chips at hypersonic frequencies (i.e., GHz) are of prominent interest for applications including radio-frequency (RF) wireless communications [11] when directly integrated with electronics.

Despite advances in the fabrication of SAW devices, these devices are not CMOS-compatible because of the utilization of crystalline substrates such as quartz, lithium niobate ($LiNbO_3$), and lithium tantalate ($LiTaO_3$). Therefore, enabling SAW devices on CMOS-compatible platforms diversifies their applications in various integrated MEMS/NEMS platforms.

Here, I intend to discuss and present a new surface phononic waveguide structure excited by a CMOS-compatible aluminium nitride (AlN) piezoelectric thin film that fits the aforementioned applications. The proposed acoustic structure is created by introducing special surface topography (i.e., periodic features) to the surface of the Si chips so that the SAWs become *laterally* confined to a region inside the piezoelectric material, which then allows for (1) the efficient use of the substrate area (which considerably scales down the size of surface devices), (2) avoiding the cross talk between surface waves in wide-beam structures as well as (3) ease of navigation on the surface of the substrate [123], and more importantly (4) better excitation and detection of surface acoustic waves in a high-acoustic-phase-velocity AlN thin film on Si substrates.

## 3.2 Surface elastic waves on half-space substrates

The *Rayleigh* mode [22] (shown in Fig. 1.2) is the most common surface acoustic mode utilized in various SAW-based devices. The phase velocity of Rayleigh modes is relatively close to bulk acoustic modes, which makes them prone to the radiation loss (or coupling to bulk acoustic modes) specially in surface acoustic resonators. Therefore, the surface acoustic modes slower than Rayleigh modes have weaker radiative components (or acoustic

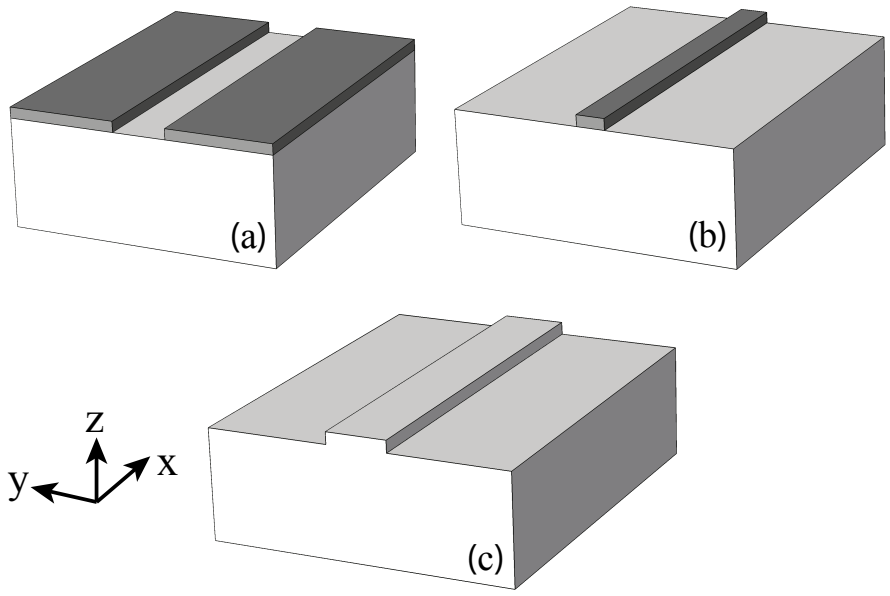


Figure 3.1: Surface acoustic waveguides with finite lateral spreading created by surface micro-machining. (a) Slot-based structures for high-acoustic-velocity thin-film material deposited on the substrate, (b) ridge-based thin-film structure for low-acoustic-velocity material deposited on the substrate, and (c) ridge structures formed by directly etching the substrate.

loss), which highlights the importance of engineered surface waveguide modes not offered by planar surfaces. In addition, the lateral extent of Rayleigh waves on untreated surfaces is unlimited. Therefore, the primary goal of designing an integrated surface waveguide is to design a structure which has (considerably) lower phase velocity (compared to the bulk waves) and finite spreading on the surface perpendicular to the direction of propagation, which hereafter I call them *Rayleigh-like* acoustic waves. Another major concern is, of course, a high electromechanical transduction between the input power and the mechanical domain for the efficient excitation/reception of the surface waves to maintain the integrity of the transmitted acoustic signal.

Two common approaches for creating structures supporting Rayleigh-like waves are [23, 124]: (1) the deposition of another thin-film material [in the form of creating a slot in the deposited high-phase-velocity film, Fig. 3.1(a), or a strip of the low-phase-velocity film, Fig. 3.1(b)] and (2) introducing the so-called surface topography by selectively etching

the substrate, as illustrated in Fig. 3.1(c). The mechanism of confinement in the former approach (i.e., deposition of another material) is analogous to optics in which the higher refractive index (or a lower phase velocity) inside the core waveguide prevents the guided mode from coupling to radiative optical modes of the surroundings with lower refractive index (or a higher phase velocity). However, the mechanism of guiding in topography-based waveguides (i.e., the later approach) is based on reducing the restraining force (or reducing the effective stiffness, $c_{eff}$) acting on a selected region, which does not have any optical analogue [125]. In either scenarios, the half-space structures may deviate from supporting a single surface acoustic mode and the upper frequency of the operation limits to the cut-off frequency of the first higher acoustic mode. Additionally, SAWs become dispersive because of a characteristic length governing the distribution of the acoustic power flow (e.g., the thickness of the deposited film or the width of the surface topography).

Compared to the thin-film-enabled acoustic waveguides, the topography waveguides allow for sharper bending due to the much higher acoustic localization inside the topography region. Despite the simplicity of topography waveguides and the lack of the need for finding two distinct materials, the electromechanical excitation is challenging particularly at hypersonic frequencies (i.e., micron/nano-scale devices). While the thin-film-deposited surface structures at hypersonic frequencies can be designed to be excited easier; however, the localization of the acoustic waves inside the guiding region should be improved, which is the focus of the rest of this chapter.

### 3.3 Surface acoustic waveguiding in AlN on Si

AlN has proven itself as a widespread piezoelectric thin-film material for nowadays on-chip commercial devices due to the best balance among high transduction efficiency, high-volume manufacturing, and low intrinsic acoustic losses [126, 127, 128] in a wide range of devices [109] from film-bulk-acoustic resonators (FBARs) [129] and solidly-mounted resonators (SMRs) to contour-mode resonators (CMRs) [130] and recently investigated for

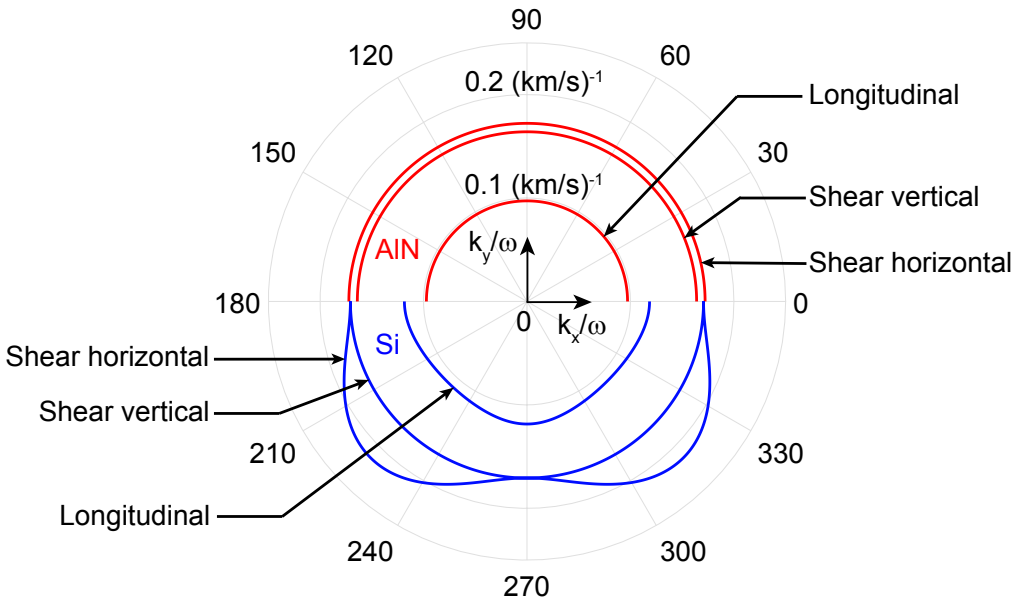


Figure 3.2: Slowness diagrams for bulk acoustic waves in Si and AlN for $k_z = 0$. The contours show $v^{-1} = k/\omega$ as a function of the angle in (100) plane with respect to [100] direction. The $c$-axis of AlN points in z-direction.

SAW devices [128]. The slowness contours (i.e., $1/v = k/\omega$) of Si and AlN for three bulk polarizations of shear vertical, shear horizontal, and longitudinal are plotted in Fig. 3.2 using the material constants listed in Tab. 1.3. Slowness contours provide information regrading the phase velocities of particular polarization, elastic stiffness symmetries (where circles indicate isotropicity) and the acoustic power flow direction (which is indicated by the normal direction to the contours). By inspecting the contours in Fig. 3.2, we realize that AlN supports faster bulk acoustic waves. Hence, the appropriate architecture for guiding Rayleigh-like waves in thin-film AlN on Si is the slot-based architecture, Fig. 3.1(a), as the velocity of the SAW inside the slot is lower compared to the velocity of the SAW propagating in AlN/Si. This has been confirmed by Fig. 3.3, where the simulation of SAW phase velocity in 1 $\mu$m AlN deposited on Si as a function of the slot width is illustrated. Figure 3.3 shows increasing the slot width results in a lower acoustic phase velocity and a higher localization in Si.

It is worth mentioning that bulk acoustic waves may not be perfectly dispersion-less

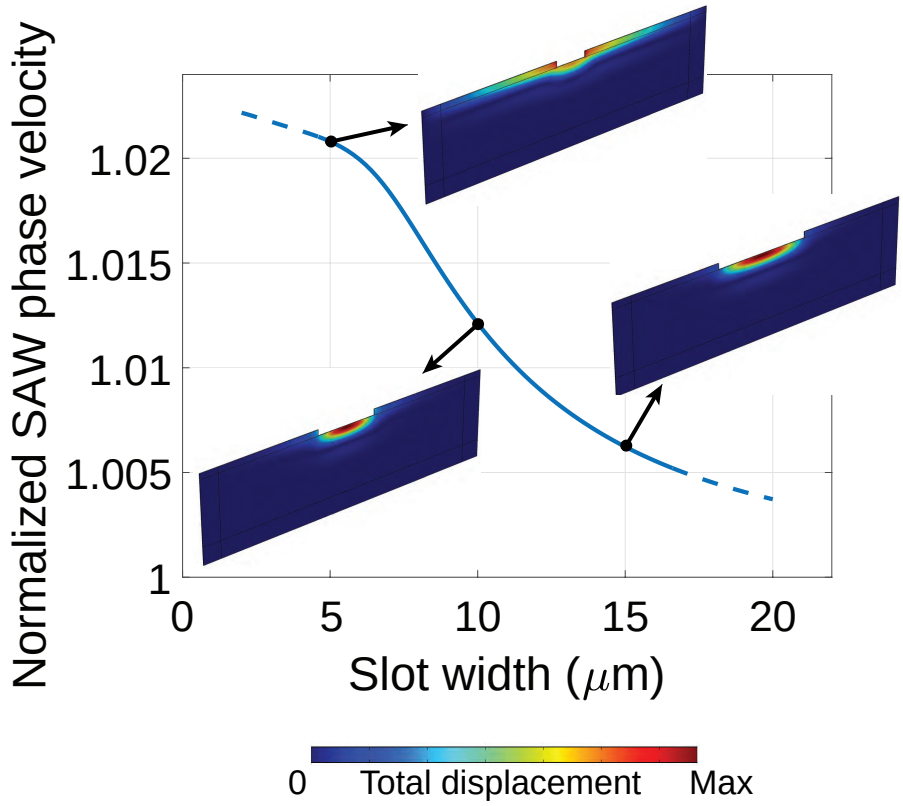


Figure 3.3: Phase velocity of confined Rayleigh-like wave inside the slot created in 1$\mu$m-thick AlN on (100) Si, normalized to the Rayleigh wave ($v_R$) on Si along the same direction. The slot is along the [100] direction. The insets show the total displacement profile of the Rayleigh-type SAW for selected widths of 5$\mu$m, 10$\mu$m, and 15$\mu$m.

(which is often negligible) and accordingly the slowness contours become frequency dependent. The dispersive behavior of materials comes from all anharmonicities such as thermoelastic damping and viscosity, and it is commonly modeled by the Zener's standard model of linear anelasticities [99, 102] by incorporating the time derivatives of stress ($\sigma$) and strain ($\epsilon$) in the following canonical equation

$$\sigma + \tau_\epsilon \dot{\sigma} = M_R(\epsilon + \tau_\sigma \dot{\epsilon}), \tag{3.1}$$

where $\tau_\epsilon$ and $\tau_\sigma$ are the relaxation time constants under constant strain and stress, respectively, and $M_R$ is called relaxed elastic stiffness tensor. The material constants listed in

Tab. 1.3 are valid up to hypersonic frequencies.

Albeit the slot-based architecture provides a better confinement of SAWs in higher-phase-velocity piezoelectric thin-film AlN on Si, the excitation or detection of such SAWs is problematic due to the concentration of the acoustic power inside Si as shown in Fig. 3.3. To overcome the challenge of the simultaneous confinement and the efficient excitation of SAWs in AlN on Si, I investigated PnC-based surface structures formed in a structured AlN piezoelectric film on Si, allowing for localizing SAWs inside the introduced piezoelectric ridge structure and enabling a higher level of electromechanical transduction.

## 3.4 Surface phononic crystals in AlN on Si

Periodic alteration of elastic properties (i.e., $c_{IJ}$ and/or $\rho$) on the surface of host materials can influence the dispersion (or phase velocity) of surface phononic modes to a degree that depends on the strength of alternation, where the tagged phononic wavelength is comparable or smaller than the periodicity length scale. These periodic structures are called surface phononic crystals (PnCs) [1, 2, 86, 3] and usually designed to exhibit a range of frequencies, the so-called phononic bandgap (PnBG), devoid of any propagating phononic mode at any direction on the surface. These PnC structures have been extensively studied numerically and experimentally in various platforms for surface acoustic waves on the surface of solids [88, 91, 47].

The judicious creation of a line defect inside the surface PnC lattice may allow for a single phononic wave to propagate along the direction of the defect (over a range of frequencies) within the PnBG frequencies, i.e., *phononic waveguiding* [35, 93, 43], enabling a wide range of different phononic devices (in particular, phononic cavities [35, 93]). Phononic waveguides are the integral parts of any all-phononic systems [38] composed of phononic cavities communicating through phononic waveguides.

### 3.4.1 Surface phononic band structure in pillar-based AlN periodic structures on Si

Figure 3.4 shows the phononic band structure of a pillar-based surface PnC arranged in the form of a triangular lattice supporting a wide PnBG from 1550 MHz to 1800 MHz whose dimensions are as follows: AlN pedestal thickness is 500 nm, pillar's height is 500 nm, and the lattice constant (i.e., the distance between nearest-neighbor pillars) is 1.3 $\mu$m. The details of phononic simulations and phononic mode profiles were discussed in Chapter 2. Briefly, the non-radiative surface phononic modes reside outside of the sound cone (represented by the gray region in Fig. 3.4) whose border illustrates the dispersion of the slowest acoustic bulk mode. To extract the surface PnBG, the eigen acoustic modes of the primitive unit cell are simulated over the boundaries (or wavenumber) of the irreducible Brillouin zone. The shaded yellow region in Fig. 3.4 specifies the complete surface PnBG frequencies as there is no surface bands existing over this range of frequencies at any direction. The irreducible Brillouin zone is determined by the symmetry of the material properties as well as the symmetry of the PnC lattice. Due to the anisotropicity in Si (see Fig. 3.2), the edges of the irreducible Brillouin zone in the triangular lattice of AlN pillars on Si becomes $\Gamma - X - L - K - \Gamma$. In order to design the AlN-on-Si PnC for possessing PnBGs at other frequency ranges, the lattice constant (or center-to-center distance between adjacent pillars), the height and radius of AlN pillars, and the thickness of AlN pedestal should be accordingly modified, where the lattice constant primarily sets the center frequency and the pillar's height adjusts the width of the surface PnBG. Other parameters are used for the fine tuning and optimization of the PnBG range of frequencies.

## 3.5 Surface waveguiding in pillar-based AlN-on-Si phononic crystal

Phononic waveguides in surface PnCs provide two-dimensional confinements (similar to slab PnCs if designed carefully), in which the out-of-plane confinement comes from the phase velocity mismatch between surface waves and bulk waves, and the in-plane con-

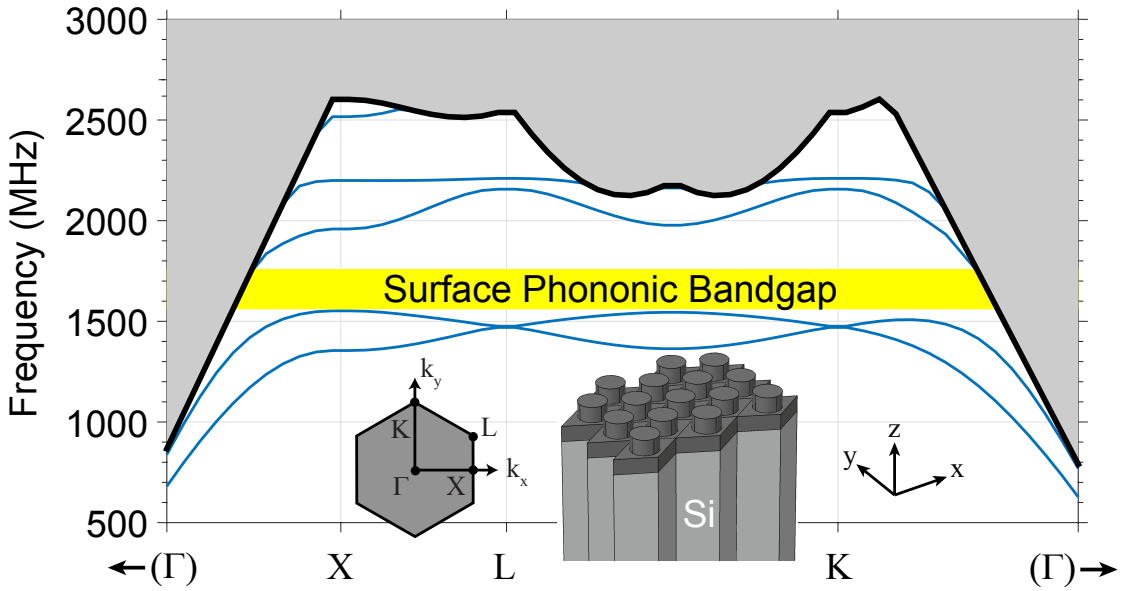


Figure 3.4: Surface Phononic band structure of a pillar-based triangular lattice of AlN on Si. The yellow shaded region specifies the range of the complete surface PnBG form 1550 MHz to 1800 MHz. AlN thickness is 1 $\mu$m and pillars' height is 500 nm. The distance between nearest-neighbor pillars is 1.3 $\mu$m.

finement is due to the PnBG of the host surface PnC prohibiting the surface leakage of phonons. The line defect creating the phononic waveguide should be periodic to obtain a well-defined wavenumber according to the Floquet's theorem, guarantying the propagation without any reflection along the defect [131].

Considering the feasibility (or ease) of fabrication, there are two practical ways of creating a line defect with no additional fabrication steps allowing for a single AlN etching step forms the surface PnC as well as the line defect: (1) a line defect primarily formed by dislocating/removing pillars (basically introducing a void structure), and (2) a line defect primarily formed by introducing additional AlN structures with the same height as of the pillars. Figure 3.5 shows an example line defect created in the pillar-based PnC structure by removing a row of pillars. Thanks to the structural mirror symmetry of the PnC waveguide with respect to the y-z plane, the simulation domain can be limited to only a half of the PnC structure (shown in Fig. 3.5) by enforcing symmetry [i.e., symmetric boundary condition (which filters the modes with the normal displacement components to the boundary)

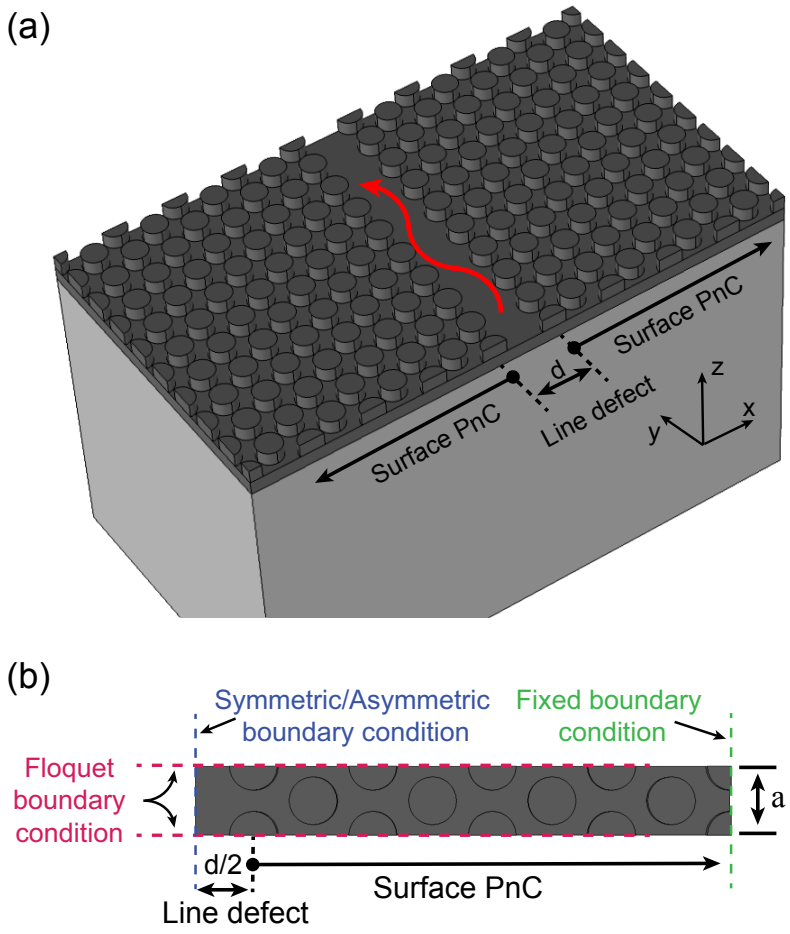


Figure 3.5: (a) Phononic waveguiding by introducing a line-defect along $\Gamma - K$ or y-direction. "d" identifies the spacing between the two PnCs. (b) Top view of the simulated PnC structure (i.e., the half of the structure) with boundary conditions labeled.

and the asymmetric boundary condition (which filters the modes with the tangential displacement component)] to find all surface eigenmodes of the actual waveguide structure. The incorporation of symmetry lowers the demanding computational resources as well as improving the simulation accuracy by using a finer meshing element.

For the surface PnC structure whose PnBG is illustrated in Fig. 3.4, the line defect is created along $\Gamma - K$ or y-direction as depicted in Fig. 3.5. As a result, for the waveguide super-cell (shown in Fig. 3.5(b)) the projected irreducible Brillouin zone becomes $k = k_y \in [0, \pi/a]$ and $k_x = k_z = 0$, in which $a$ identifies the periodicity of waveguide super-cell identical to the lattice constant of the PnC. Among those wavenumbers inside the

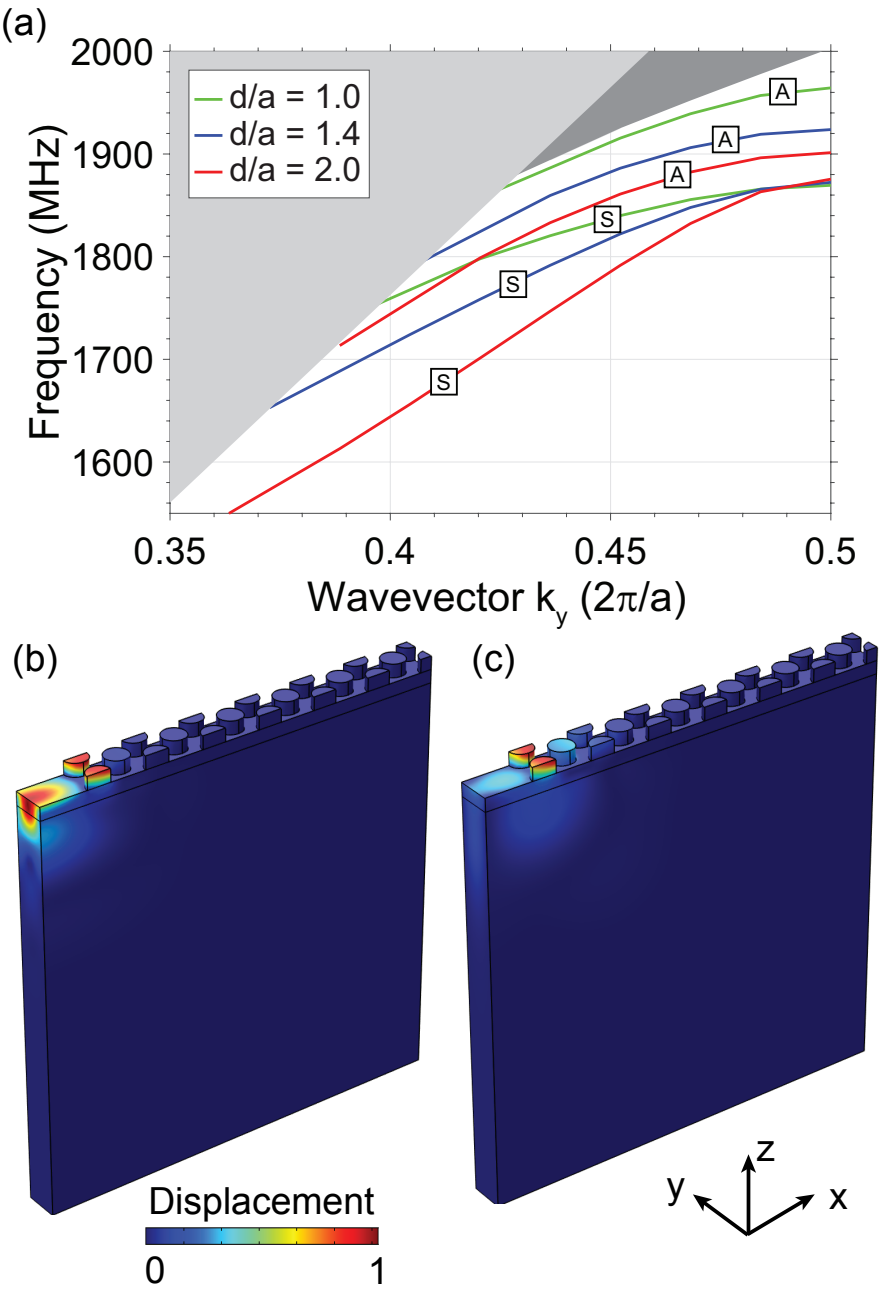


Figure 3.6: Surface phononic waveguiding in the pillar-based PnC formed by introducing a pillar-free defect (see Fig. 3.5). (a) Dispersion bands of the selected defects for $d/a = \{1, 1.4, 2\}$ (label A: Asymmetric modes and label S: Symmetric modes). (b) and (C) total displacement profiles of the guided modes in the surface phononic waveguide with $d/a = 2$ at $k_y = 0.436(2\pi/a)$ obtained by the symmetric boundary condition ($f = 1745.3$ MHz) and asymmetric boundary conditions ($f = 1833.1$ MHz), respectively.

irreducible Brillouin zone, we are interested in the wavenumbers lying outside of the sound cone and in the frequencies within the PnBG. This allows the surface mode to be confined to the defect and not propagating through the PnC or couple to the radiative bulk modes. It is worth noting that we observe a zero group velocity at $k_y = \pi/a$ due to the symmetry of the phononic bands. Therefore, the phononic wave-packet transmission should be away from high symmetry points and mostly over the linear part of the dispersion [4] to avoid the distortion of the transmitted wave-packet. On the other hand, for designing a phononic cavity it is often preferred to select the wavenumbers close to the high symmetry points in the middle of the PnBG to lower the radiation loss as much as possible.

### 3.5.1 Type 1: line defect created by removing AlN pillars

The simplest way of creating a waveguide (or line defect) in a PnC structure is by putting two arrays of surface PnCs (acting as a perfect acoustic mirror over the PnBG frequencies) at a distance away from each other. In this case, the surface acoustic wave can only exist over the distance between the two PnCs (see Fig. 3.5). The eigenmodes of the surface PnC waveguide are then extracted by applying the symmetric and asymmetric boundary conditions. Figure 3.6 provides the dispersion of selected line defect widths formed by introducing a pillar-free region (i.e., Fig. 3.5) for $d/a = \{1, 1.4, 2\}$. In Fig. 3.6(a), the light gray region contains the radiative bulk modes while the dark gray region consists of unguided surface PnC modes. As Fig. 3.6(a) shows, the single-mode region for the symmetric modes is close to the sound-line while for the asymmetric modes it is close to the phononic conduction bands (i.e., PnC surface modes not confined to the line defect).

In this type of the line defect, the only design parameter for adjusting the dispersion and obtaining a desired single-mode operation is the width of the defect or "d". Albeit, with increasing the defect width the asymmetric bands go to a lower frequency and distance from the radiative conduction bands, it causes the width of the single-mode operation for the asymmetric modes becomes narrower. Therefore, the Type-1 defect provides the desired

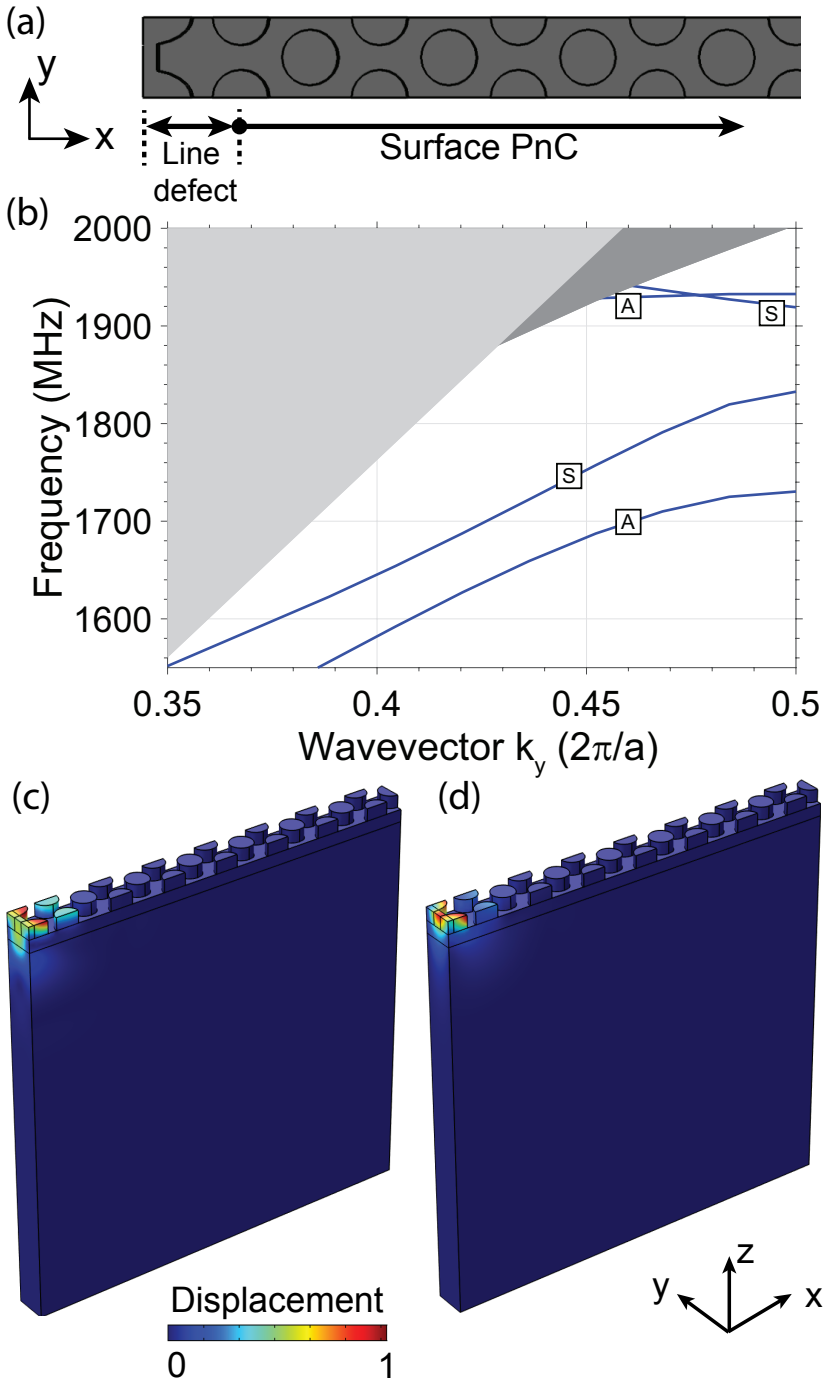


Figure 3.7: Surface phononic waveguiding in the pillar-based PnC formed by introducing a ridge AlN structure. (a) Top-view of the designed ridge structure with the same height as of the pillars of the PnC structure. (b) Dispersion bands of the ridge structure (label A: Asymmetric modes and label S: Symmetric modes). (c) and (d) total displacement profiles of the surface guided modes at $k_y = 0.484(2\pi/a)$ obtained by the symmetric boundary condition ($f = 1819.6$ MHz) and asymmetric boundary conditions ($f = 1725.0$ MHz), respectively.

confinement and localization of acoustic waves inside AlN. However, the limited range of usable single-mode operation in this defect makes them less attractive for practical single-mode waveguide applications.

### 3.5.2 Type 2: line defect created by introducing a ridge AlN structure

Another type of the line defect is formed by introducing a (corrugated) ridge AlN structure. The additional design parameters of this structure can be used to tailor a desire phononic dispersion for the waveguide modes in particular a single-mode operation, which is essential for designing a waveguide-based surface phononic cavity. For the ease of fabrication, the height of pillars and that of the ridge waveguide are identical. The ridge AlN structure is shown in Fig. 3.7(a) and its corresponding surface modes are illustrated in Fig. 3.7(b). As Fig. 3.7(b) illustrates, the surface waveguide structure supports a much wider single-mode operation for the symmetric mode. Figures 3.7(c) and 3.7(d) provide the displacement mode profile of the symmetric and asymmetric modes selected from the lower branches of the symmetric and asymmetric bands of the structure.

# CHAPTER 4

# INTEGRATED MODE-GAP WAVEGUIDE-BASED PHONONIC CRYSTAL RESONATORS

Resonators in PnCs or any kinds of periodic structures are commonly formed by adding a point (or regional) defect [132], which is usually achieved by modifying the geometry or dislocating a subset of holes or pillars in the perfect periodic structure in the range of the PnC bandgap frequencies. The resulting confinement of the acoustic mode in the defect area by the PnC bandgap reduces the coupling-loss of localized modes to the unconfined modes in the periodic structure. The quality factors (Qs) of such resonators are, therefore, limited by the material loss if the PnC structure is designed carefully. Here, I focus on the systematic design of mechanical resonators in PnCs, in particular, waveguide-based PnC resonators. In these resonators, the input and output electrodes are integrated with the resonator (over the resonant area) to allow for direct excitation and detection of the resonant mode of the PnC resonator.

One of the main design challenges of a waveguide-based phononic resonator is the waveguide termination, which can highly affect the Q (or loss) of the resonator. Previous waveguide-based PnC resonators were implemented by abruptly terminating the PnC waveguide with a complete PnC structure [35]. However, such abrupt terminations result in high perturbation of the waveguide mode that can result in coupling to the lossy unconfined PnC modes. An alternative approach for confining the acoustic modes while minimizing the PnC waveguide perturbation is to use the concept of phononic mode-gaps rather than complete phononic bandgaps at the waveguide terminations. Such approaches have already been successfully implemented in *photonic crystal cavities* [133]. In mode-gap-based resonators, a heterogeneous-waveguide structure is used, in which the guided mode of the core waveguide is not supported by the surrounding waveguides (i.e., surrounding waveg-

uide have a mode-gap at the frequency range corresponding to the target guided mode of the core waveguide); hence, the energy remains inside the middle region (i.e., the resonant area). The introduced perturbation in this approach is sufficiently small that still preserves the global periodicity of the structure.

In this chapter, I present a new design for integrated phononic crystal (PnC) resonators based on confining acoustic waves in a heterogeneous waveguide-based PnC structure [134, 93]. In this architecture, a PnC waveguide that supports a single mode at the desired resonance frequencies is terminated by two waveguide sections with no propagating mode at those frequencies (i.e., have mode gap). The proposed PnC resonators are designed through combining the spatial-domain and the spatial-frequency domain (i.e., the k-domain) analysis to achieve a smooth mode envelope. This design approach can benefit both membrane-based and surface-acoustic-wave-based architectures by confining the mode spreading in k-domain that leads to improved electromechanical excitation/detection coupling and reduced loss through propagating bulk modes. The new design for PnC resonators based on a heterogeneous three-region PnC waveguide based architecture is composed of: 1) a single-mode PnC waveguide, 2) two end terminating PnC waveguides with mode gap, and 3) two adiabatic transition regions. This new design enables us to design a PnC resonator mode with smooth spatial mode profile with maximum localization in k-domain that allows for higher coupling efficiency and possibly lower loss. The proposed architecture also can be extended to SAW-based devices in which it can considerably suppress radiation loss due to coupling to the bulk modes. The high-Q and low input impedance enabled by the proposed structure are applicable to a wide range of PnC lattices and material structures for various applications.

## 4.1 Proposed resonator structure

Two common PnC resonator structures are the Fabry-Perot resonators [34] (see Fig. 4.1(a)) and the waveguide-based PnC resonators formed by a line segment defect in otherwise

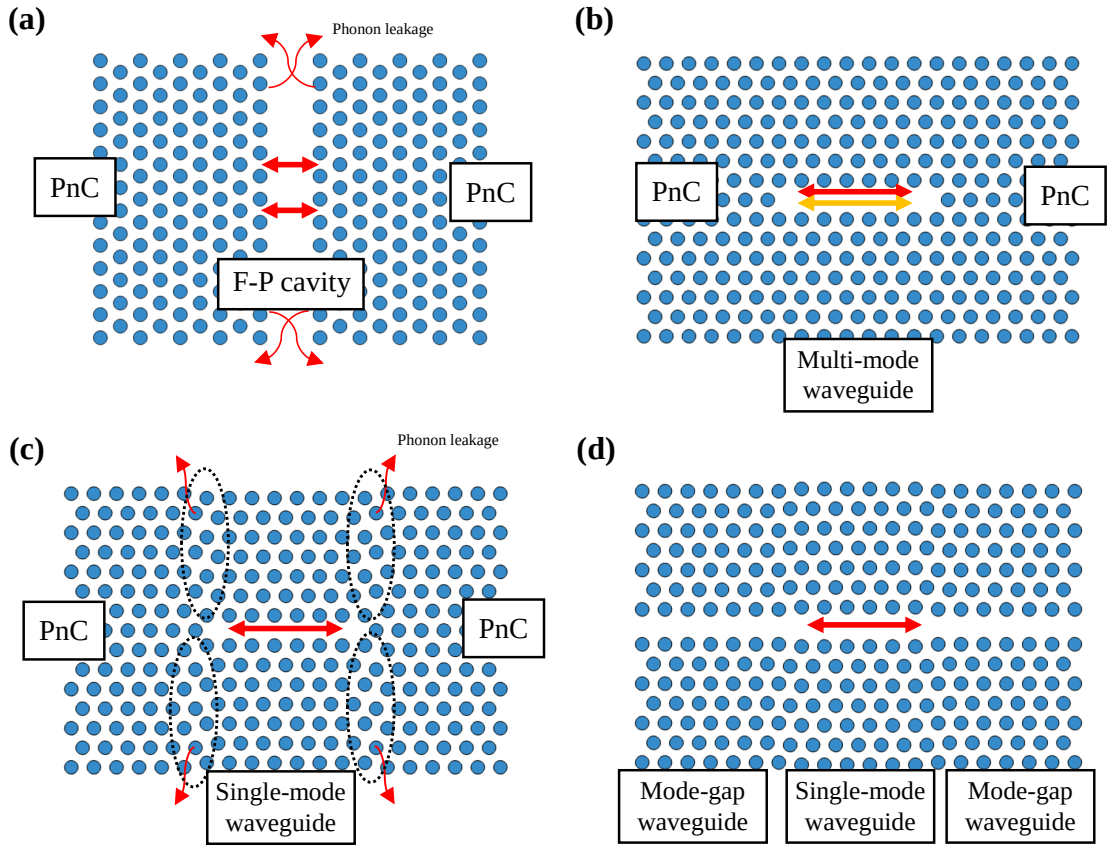


Figure 4.1: Different schemes for PnC resonators. (a) Transversal resonances between two arrays of PnC. (b) Multi-mode waveguide-based resonators without dislocating adjacent unit cells to the waveguide. (c) Single-mode waveguide that is abruptly connected to PnC. (d) Single-mode waveguide that is adiabatically terminated to mode-gap waveguides.

complete PnC lattice [35] (see Fig. 4.1(b)). Despite impressive performance, both of these architectures have structural limitations. The former has a large structure and is not suitable for dense integration with other functional PnC structures while the latter may suffer from inherently multi-mode waveguide with difficult excitation (see Fig. 4.1(b)) as well as leakage of phonons at the abrupt discontinuity between the PnC waveguide and the complete PnC (see Fig. 4.1(c)). An ideal waveguide-based resonator should support single-mode operation with minimal leakage (or no abrupt termination). The design of such optimal resonators is the focus of this chapter. While the proposed approach can be implemented in different PnC platforms, I demonstrate it in a membrane PnC structure (see Fig. 4.3(a)).

The proposed resonator structure (schematically shown in Fig. 4.1(d)) is composed of a

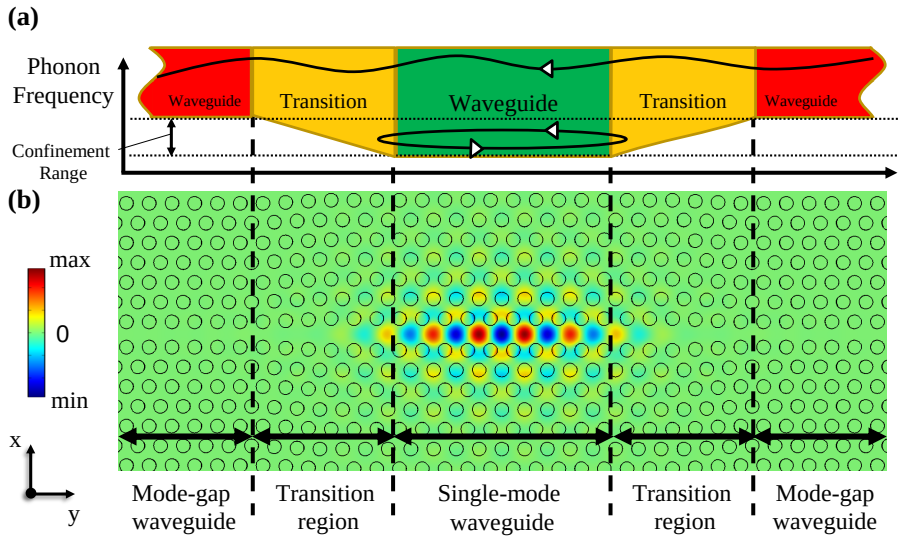


Figure 4.2: Schematic of the mode-gap waveguide-based resonators. (a) The mechanism of confinement in mode-gap termination and the frequency ranges the phononic mode is propagating or confined. (b) The acoustic resonance mode with mode-gap termination.

segment of single-mode PnC waveguide terminated at both ends to another PnC waveguide with no allowed guided mode (i.e., terminated to PnC waveguides with a mode gap for the middle single-mode waveguide). The detailed implementation of this resonator is shown in Fig. 4.2 in which the single-mode PnC waveguide in the middle is formed by removing one row of metallic PnC pillars and reducing the width of the PnC waveguide to remove unwanted guided modes and obtain a single-mode waveguide at the frequency of interest. The geometry of the PnC structure is adiabatically adjusted from the middle single-mode PnC waveguide to the mode-gap PnC-waveguides at two sides.

As highlighted in Fig. 4.2(a), the mode gap in the surrounding waveguides is obtained by engineering the phononic dispersion of the PnC waveguide through changing the spacing (w) between the pillar rows forming the waveguide super cell. In addition to smoothing the transition between the single-mode waveguide and the mode-gap waveguides, the transition region allows for fine tuning of the acoustic resonance mode. The length of the middle waveguide is usually selected based on: 1) the target resonance frequency, 2) the dimension needed for implementation of the necessary transducers to excite and detect the

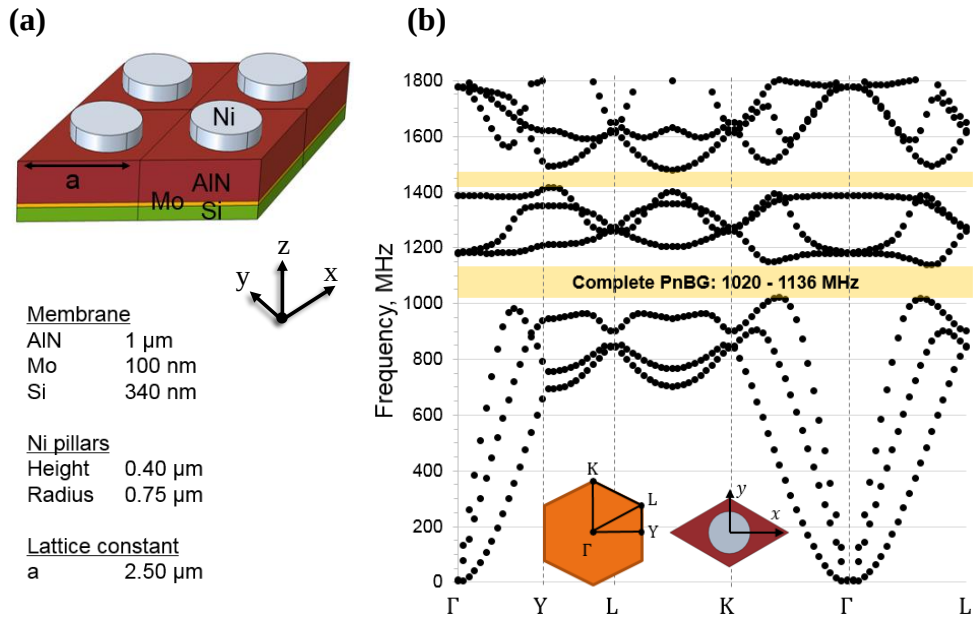


Figure 4.3: Unit cell phononic band structure. (a) The composition of the PnC and the dimensions. (b) The band structure of the phononic unit cell on the edges of the irreducible Brillouin zone showing two complete phononic bandgaps at 1.07 GHz and 1.45 GHz.

acoustic mode, and 3) the desired input impedance of the resonator. Figure 4.2(b) shows the simulated out-of-plane field pattern of the resonance mode of the proposed structure; it clearly demonstrates the acoustic wave confinement in the center of the PnC resonator.

## 4.2 Design and simulation of the mode-gap resonator

The first design step is to form a PnC structure with a large phononic bandgap (PnBG). Based on the detailed theoretical simulation, I chose a triangular lattice of nickel (Ni) pillars with detailed dimensions shown in Fig. 4.3(a). This structure is selected by calculating the band structure of a large number of PnC structures with different lattice symmetry and unit cell geometry. The calculated band structure of this PnC is shown in Fig. 4.3(b), which is based on 3D-FEM implemented in the COMSOL environment. The wavenumber is swept over the edges of the irreducible Brillouin zone shown in the inset of Fig. 4.3(b) (due to the anisotropicity in Si and lattice symmetry) to accurately extract the unit cell phononic

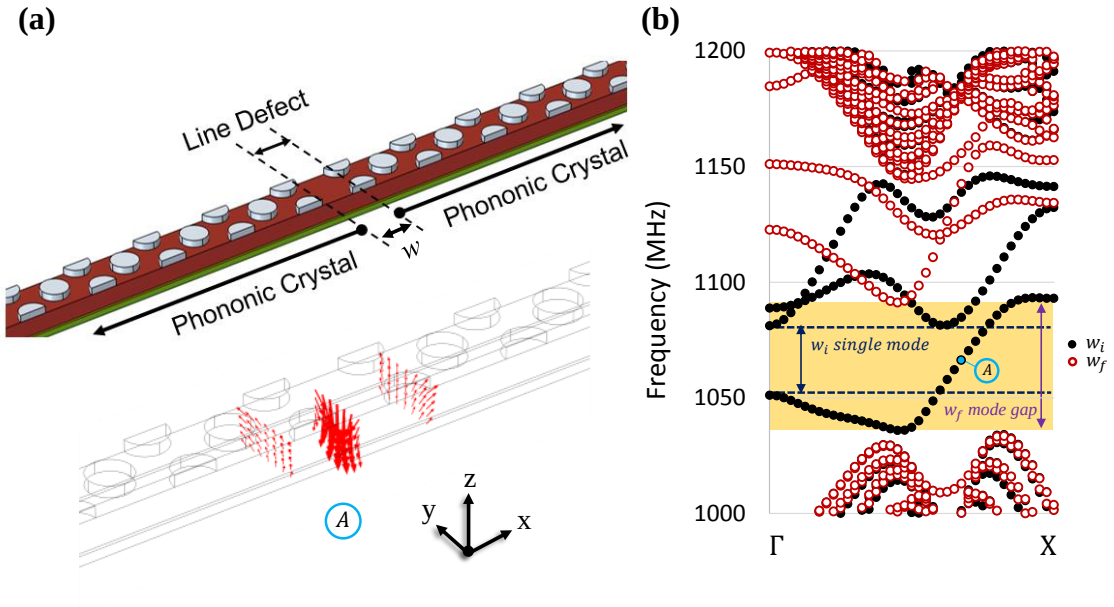


Figure 4.4: (a) The schematic of the waveguide unit cell formed by removing a row of pillars and the vectorial displacement profile of a vibration mode inside the mode-gap region (i.e., point A in (b)). (b) Phononic dispersion of the designed single-mode PnC waveguide and the mode-gap PnC waveguide. The shaded region specifies the range of mode-gap frequencies if the waveguide width $w_i$ varies to $w_f$. The blue dash lines specify the extent of the single-mode range of frequencies for $w_i$.

band structure. The details of the physics and simulation of the PnBG in the pillar-based membrane structure discussed in Ref. [31]. Figure 4.3(b) shows the existence of two PnBGs centered at 1.07 GHz and 1.45 GHz. I implemented my resonator in the lower PnBG due to its wider bandgap. The next step is to design a single-mode PnC waveguide (by adding a line defect) with a reasonably large single-mode guiding bandwidth. The line defect is created by removing one row of pillars in the $\Gamma - K$ direction (see Fig. 4.4). To design the single-mode PnC waveguide and the mode-gap PnC waveguides in Fig. 4.2(b), I vary the width of the guided region ($w$) over a large range and calculate the dispersion diagrams of the guided mode(s) within PnBG of the PnC waveguide. The simulation results (using 3D-FEM) for two values of $w$ ($w_i$ and $w_f$ corresponding to the width of the single-mode and the mode-gap PnC waveguide respectively) are shown in Fig. 4.4(b). Figure 4.4(b) clearly shows the single-mode operation of the center waveguide with $w = w_i = 0.8 \times a\sqrt{3}$ and the

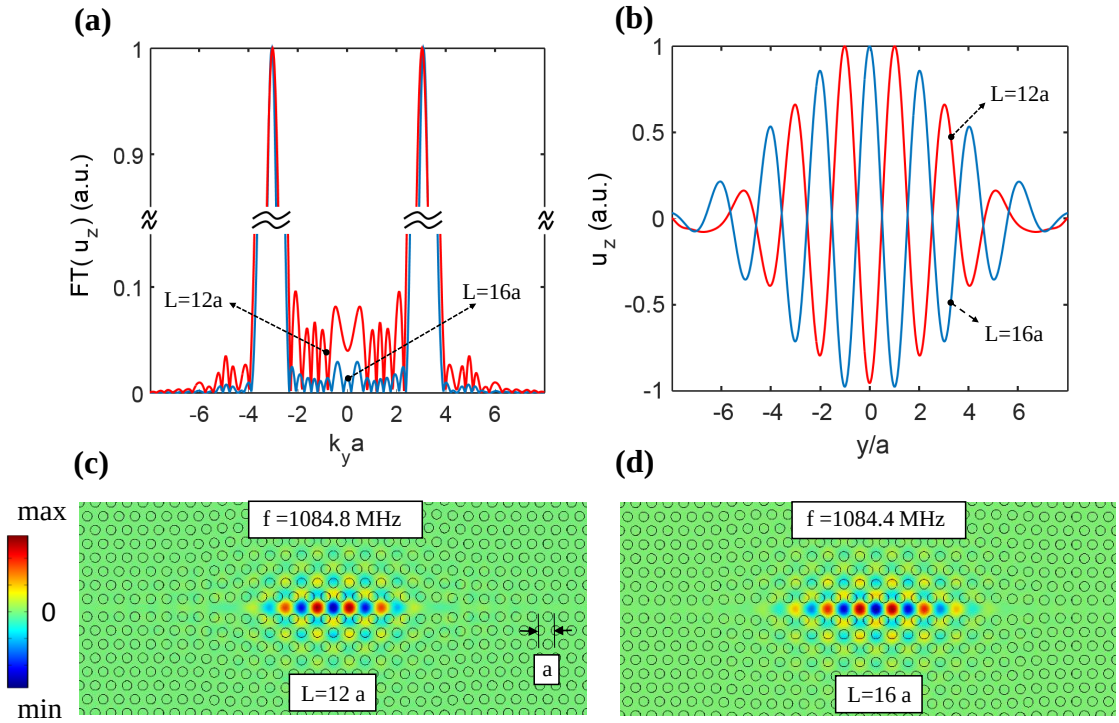


Figure 4.5: Mode-gap phononic resonators at different lengths. (a)-(b) k-domain and real domain of two acoustic resonance modes for the out-of-plane displacement profile shown in (c)-(d) with normalized length of 12 (red curve) and 16 (blue curve) and the same termination profile.

existence of the mode gap for $w_i$ at the terminating waveguides $w = w_f = 0.64 \times a\sqrt{3}$ in the frequency range of 1.05 GHz–1.07 GHz. The mode of the single-mode waveguide is an asymmetric Lamb wave with dominant out-of-the-plane vibration, which can be efficiently excited by IDTs on top of the structure.

The design of the adiabatic transition region on the two sides of the single-mode PnC waveguide depends on the difference between $w_f$ and $w_i$ in Fig. 4.4. To optimize these transition region, I use the design strategy developed for the photonic crystal counterpart of these structures [133]. The design goal in this approach is to form a waveguide-based resonance mode with two sharp peaks in the k-domain (i.e., Fourier transform of the spatial coordinate in the out-of-plane direction, z-direction in Fig. 4.4). This assumes the relatively uniform distribution of the field energy of the resonant mode over the central region, which

facilitates the excitation by IDTs and reduces the input impedance of the structure. The design approach is demonstrated in Fig. 4.5 for two different lengths of the transition region, in which the waveguide width changes from $w_f$ to $w_i$.

Figures 4.5(a) and 4.5(b) show the z-component (i.e., out-of-plane component) displacement profiles of two flexural resonance modes in the k-domain and the spatial domain, respectively. The uniform distribution of the resonance mode energy over the entire single-mode region in spatial domain and tight localization in k-domain in the form of two sharp peaks are evident from Figs. 4.5(a) and 4.5(b). In addition, the $L = 16\,a$ results in weaker strength of $u_z$ in DC content of k-domain outside of the two sharp peaks as it is a longer waveguide with less acoustic energy concentration at the terminations, which is desirable. Note that, these two sharp peaks correspond to the forward and backward wave propagation in the center PnC waveguide, which forms a standing wave as evidenced by the spatial mode pattern in Fig. 4.5(b). Also note that the suppression of the acoustic energy corresponding to low k values (i.e., among DC component) is highly desirable in extending this design to the SAW-based PnCs in which the low wave vector components of resonant acoustic mode, that fall within sound cone (or the radiative region), can couple to the bulk modes, resulting in considerable acoustic loss and low resonator Q.

Designing a high-Q low-input-impedance waveguide-based resonator also requires: 1) the resonance frequency to be close to the middle of the PnC bandgap to minimize leakage through limited number of fabricated PnC layers, 2) lower elastic energy concentration in the metallic pillars to reduce the metallic loss, and 3) dominant vibration in the out-of-plane direction to be efficiently excited by the fabricated IDTs, which accordingly lowers the input impedance.

## 4.3 High-Q surface phononic crystal resonator

The demonstration of hypersonic surface PnC platform in Chapter 2 paves the way toward fabricating practical CMOS-compatible low-loss PnC devices for filtering applications in

wireless communications. At the heart of such PnC devices, a high-Q phononic resonator is always necessary. My surface PnC platform offers a lower level of material phononic loss due to the utilization of non-metallic (i.e, dielectric-based) pillars for realizing the surface PnC devices. However, in addition to the material loss, structural losses including the radiation loss (i.e., coupling to bulk modes) and fabrication-induced phononic losses (e.g., sidewall roughness) should be also minimized. To minimize the radiation loss in the surface PnC resonator, an appropriate defect should be introduced to the PnC lattice supporting a phononic resonance mode (close to the middle of the surface PnBG) whose wavenumber content within sound cone of the underlying Si substrate is sufficiently weak. This will ensure that the coupling to the radiative bulk modes as well as coupling to the unconfined surface PnC modes is suppressed.

I designed my surface PnC resonators according to the proposed mode-gap waveguide-based technique as detailed in Sec. 4.2. My strategy to realize such a point-like defect is to connect a single-mode surface PnC waveguide smoothly (or adiabatically) over a transition region with mode-gap termination waveguides. I use an optimized surface phononic waveguide based on the ridge-type structure as detailed in Chapter 3.

To address fabrication imperfection losses, I optimized an ICP etching recipe for dry etching AlN by using a high-resolution negative e-beam resist flowable oxide (FOx) to pattern a hard etching mask for AlN PnC structures by e-beam lithography (see Fig. 4.6). This significantly reduces roughness compared to the lift-off process of chromium (Cr). Additionally, the FOx etching mask allows for more vertical sidewalls compared to Cr etching mask. This enables patterning a dense array of (high-aspect-ratio) AlN pillars for realizing SAW-PnC supporting a PnBG at multi-GHz.

### 4.3.1 Designing mode-gap termination in the pillar-based SAW-PnC platform

Designing a wideband single-mode waveguide is challenging and requires an extensive search through FEM simulations with several optimization parameters. In Chapter 3, the

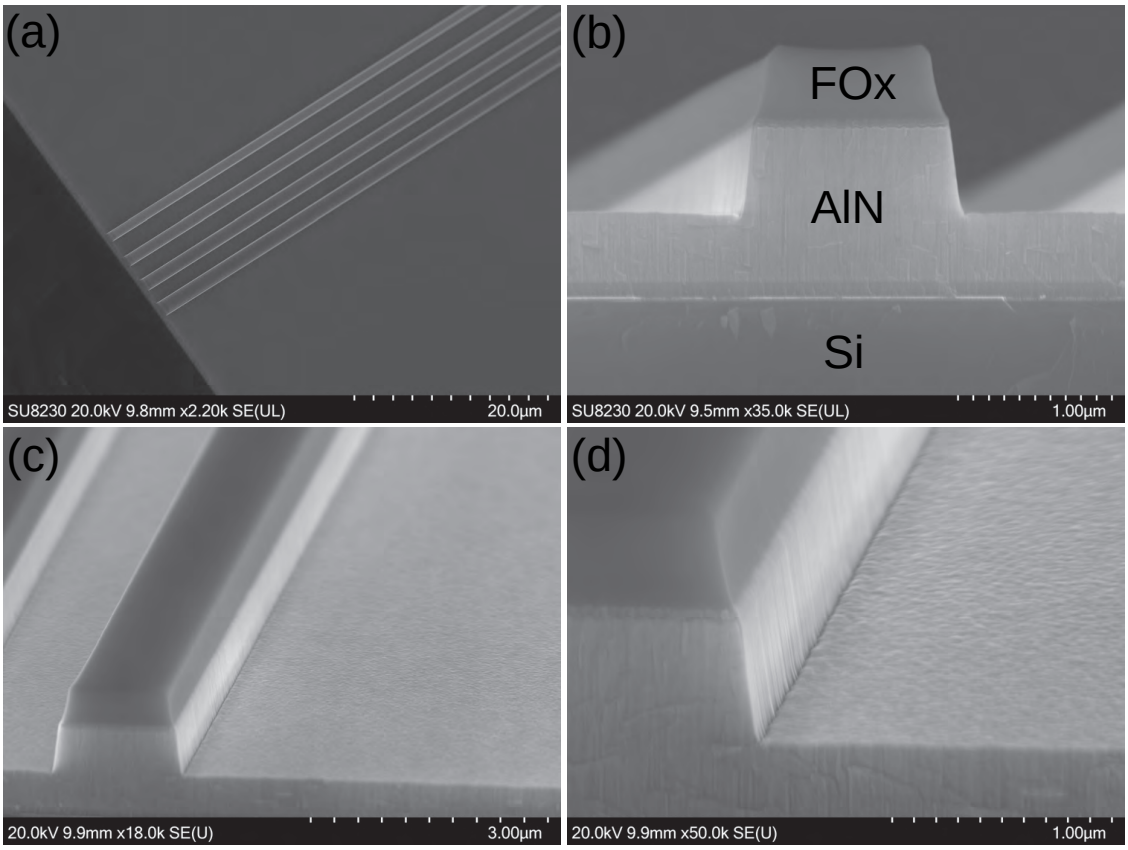


Figure 4.6: AlN waveguide structures patterned by FOx and etched in an ICP etching tool. (a) The top-view SEM of the fabricated AlN waveguides. (b) Cross-section of the fabricated AlN waveguides (from top to bottom: FOx/10 nm Cr/AlN/Si). Evaporated Cr was initially used to protect AlN structures in TMAH (TMAH is the developer for FOx). Later, I used ALD $SiO_2$ to protect AlN in TMAH. (c) and (d) show the roughness on the sidewall of the fabricated AlN waveguides. The sidewalls are close to vertical.

surface phononic waveguiding in the pillar-based PnC platform in AlN on Si was studied and the ridge-based line defect was proposed for the realization of surface phononic waveguiding. In such pillar-based platforms, the strategy for designing the mode-gap termination (starting from the main single-mode waveguide positing in the central part of the cavity) is not by laterally adjusting the size of the defect, but by anisotropically scaling the waveguide super-cell along the direction of the defect. This approach of perturbation allows for side-coupling of several PnC resonators for designing higher-order SAW filters by conveniently adjusting the mechanical couping between the surface PnC resonators without worrying about lattice mismatches.

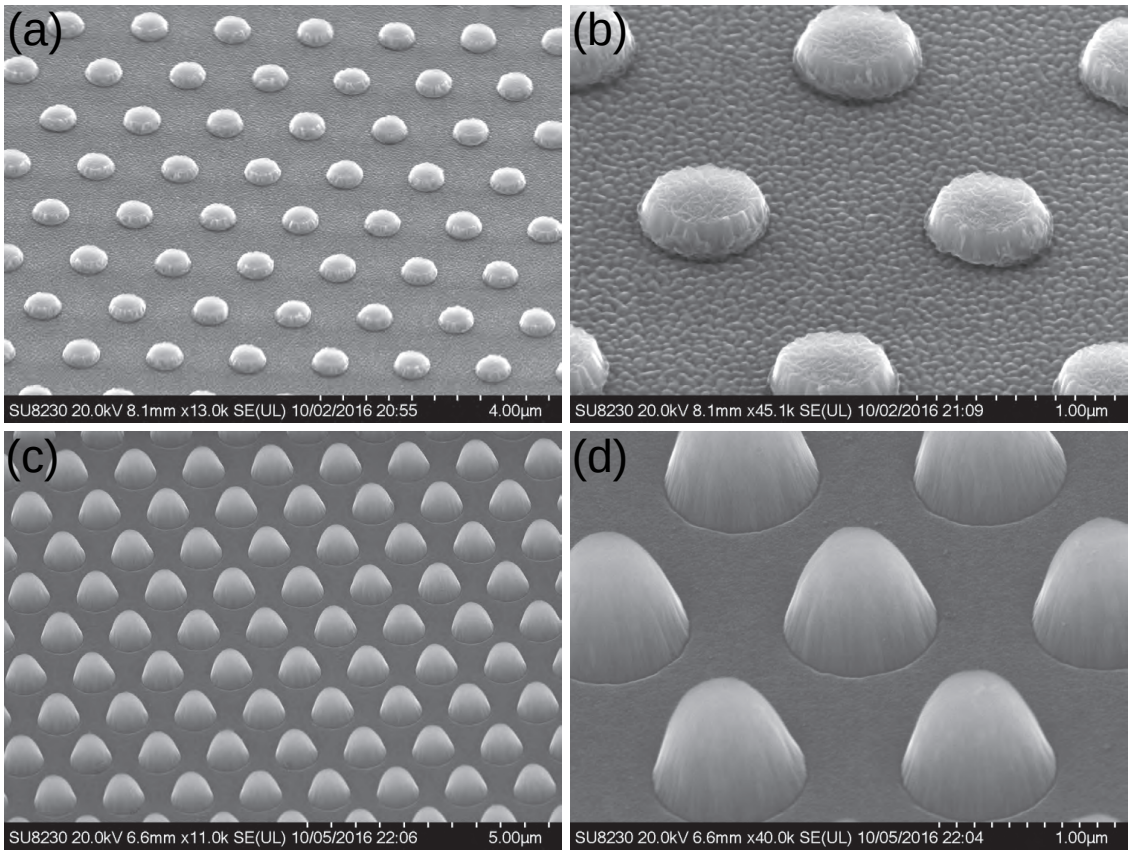


Figure 4.7: ICP etching of AlN PnC structure using a chromium (Cr) lift-off mask. (a) and (b) show the side-view SEMs from an AlN sample patterned with a Cr mask prior to ICP etching. (c) and (d) provide side SEMs from the AlN sample after 500 nm etching of AlN and removing the residue of Cr in a wet process.

### 4.3.2 Etching AlN PnC devices using FOx hard mask

Despite simplicity, creating a Cr hard mask by a lift-off process [i.e., patterning a positive e-beam resist followed by evaporation of Cr and then lift-off of the deposited Cr, see Figs. 4.7(a) and 4.7(b)] limits the density of AlN feature sizes by their angle of the sidewalls. Since in pillar-based surface PnCs, the aspect ratio of the pillars is usually high, the sidewall angle could limit the realization of hypersonic surface PnCs. Moreover, the deviation from vertical sidewalls lowers the bandwidth of the PnBG. Non-vertical sidewalls stem from the fact that the lift-off process creates a Cr mask with non-vertical sidewalls because of the shadowing effect (see Fig. 4.7(b)), which results in non-vertical AlN pillars during ICP etching of AlN as shown in Figs. 4.7(c) and 4.7(d).

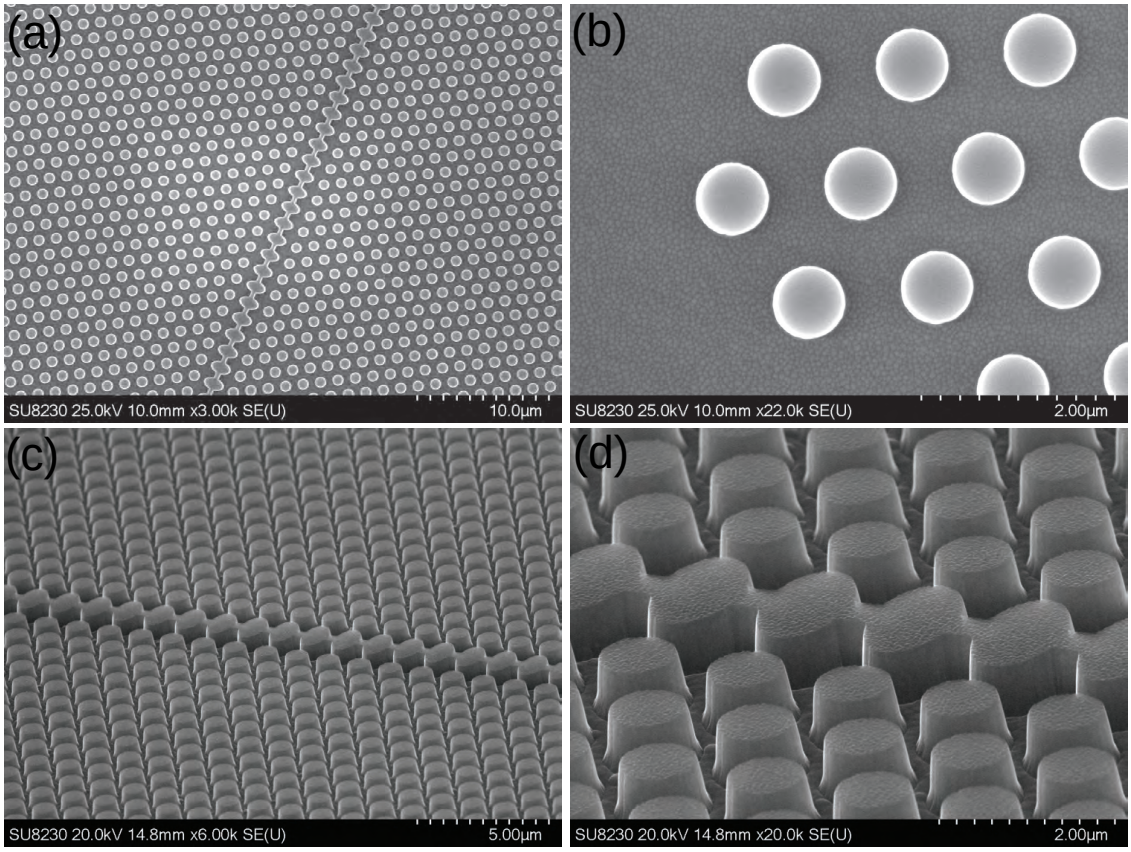


Figure 4.8: ICP etching of AlN PnC resonators using the FOx e-beam resist with the thickness of 700 nm. (a) and (b) show the top-view SEMs from an AlN sample patterned with FOx prior to ICP etching. (c) and (d) provide side SEMs from the AlN sample after 500 nm etching of AlN and removing the residue of FOx with BOE.

To fabricate the surface PnC resonators a new etching mask was developed by e-beam patterning of a high-resolution negative resist FOx (from Dow Corning) to enable vertical sidewalls. Tetramethylammonium hydroxide (TMAH) is the developer of Fox and severely etches AlN. Therefore, AlN samples have to be protected in TMAH. I deposit 10 nm AlD $SiO_2$ to protect the AlN samples during the development of the FOx. Figures 4.8(a) and 4.8(b) show the FOx etching hard mask patterned on an AlN sample coated with a thin layer of ALD $SiO_2$. As Figs. 4.8(c) and 4.8(d) show, FOx enables the fabrication of more vertical sidewalls which helps to increase the width of the PnBG as well as the fabrication of AlN PnC structures for much higher frequency.

# CHAPTER 5
# STIMULATED BRILLOUIN SCATTERING IN PHONONIC-CRYSTAL-ASSISTED SILICON NITRIDE WAVEGUIDES

In this chapter, I investigate the application of hypersonic pillar-based membrane PnC structure for designing stimulated Brillouin scattering (SBS) structures in silicon nitride (SiN) [135, 136]. These SiN PnC structures benefit from low optical losses, wide optical transparency window, and high optical power-handling of SiN, which enables my structures to achieve high total SBS gain (i.e., $G_{\mathrm{SBS}} = g_{\mathrm{m}} P_{\mathrm{p}}$). Additionally, the tensile-stressed LPCVD SiN when accompanied by my designed PnC membrane can lower the SBS threshold power by suppressing phononic leakage. Moreover, the PnC membrane in the proposed SiN waveguides can enhance SBS by: 1) maximizing the overlap between the desired acoustic modes with the optical forces, and 2) reducing the number of unwanted acoustic modes. Minimizing unwanted acoustic modes could also potentially reduce the power budget for the SBS process by eliminating the creation of unwanted Stokes wave from the scattered input pump. My photonic/phononic platform allows for the design of single-mode acoustic waveguides, which benefits applications including GHz-rate comb generation with a uniform RF spacing between comb lines. Harnessing SBS in SiN enables monolithic integration of SBS devices with on-chip photonics and electronics functionalities, which promises unprecedented on-chip nonlinear optics and GHz signal processing applications in an integrated platform.

## 5.1 Theory of stimulated Brillouin scattering

Inelastic scattering of light by lattice vibration (so called phonon) falls into two regimes, according to whether the phase shift between the adjacent vibrating lattice sites (i.e., atoms) is negligible or not. In the Brillouin regime, light scattering induces a tiny phase shift

between atoms and results in the excitation of acoustic phonons. In the Raman regime, however, the phase shift is non-negligible and light scattering involves optical phonons. Depending on whether the creation of phonons is due to fluctuations or an intense optical force, the scattered light falls in either the spontaneous or stimulated regime, respectively. Similar to optical parametric oscillations (OPOs), the prerequisite to an efficient stimulated Brillouin scattering (SBS) is the precise phase-matching between a pair of optical modes (pump and red-shifted Stokes) and an acoustic mode. In other words,

$$\begin{aligned} \omega_{\mathrm{p}} - \omega_{\mathrm{s}} &= \Omega_{\mathrm{m}} \text{ (energy conservation)}, \\ \overrightarrow{k}_{\mathrm{p}} - \overrightarrow{k}_{\mathrm{s}} &= \overrightarrow{K}_{\mathrm{m}} \text{ (momentum conservation)}, \end{aligned} \tag{5.1}$$

in which, $\omega/2\pi$ ($\Omega/2\pi$) and $\overrightarrow{k}$ ($\overrightarrow{K}$) are the frequency and wavevector of the optical (acoustic) modes, and $p$, $s$, and $m$ denote the pump, Stokes, and acoustic modes, respectively.

Although Brillouin scattering was predicted in the 1920s, the interaction was experimentally confirmed in quartz and sapphire [137] in 1964 following the invention of the laser. Since then, with the advancement in microphotonic and nanophotonic fabrication technologies, devices that meet the essential requirements of SBS process have been progressively enhanced, enabling numerous applications for SBS including narrow-linewidth lasers [58, 138, 65], inertial sensors [59], non-reciprocal optical devices [139, 140], GHz-rate comb generation [52, 53, 141, 142], and slow light and optical memories [60, 61, 143]. These appealing applications have motivated further investigations of SBS and its implementation in platforms compatible with integrated photonics [54, 50, 63] and electronics [144].

Different platforms have been studied for SBS such as chalcogenide glasses [51, 62], Si [54, 50, 63], silica [52, 64, 49, 65], and $CaF_2$ [55] to obtain a large SBS gain, $g$, and ultimately a very low threshold power, $P_{th}$, quantified as [145, 146, 54]

$$g(\Omega) = \frac{\omega_{\rm o} Q_{\rm m}}{2k_{\rm m}} |\langle \mathbf{f}, \mathbf{u}_{\rm m} \rangle|^2 \mathcal{L}_{\rm m}(\Omega - \Omega_m),$$
$$P_{\rm th} = \alpha / g_{\rm m}, \tag{5.2}$$

where $\omega_{\rm o}/2\pi$ and $\alpha$ are the optical frequency and the optical loss of the waveguide, respectively; $\mathbf{f}$ is the power-normalized optical force vector, and $\Omega_{\rm m}/2\pi$, $\mathbf{u}_{\rm m}$, $Q_{\rm m}$, and $k_{\rm m}$ are, respectively, associated with the resonance frequency, displacement vector, quality factor, and effective stiffness of the acoustic mode m, $g_{\rm m} = g(\Omega_{\rm m})$ and $\mathcal{L}_{\rm m}(\Omega - \Omega_m)$ is the normalized Lorentzian lineshape with $\mathcal{L}_m(0) = 1$. I assumed $\omega_{\rm s} = \omega_{\rm o}$ and $\omega_{\rm p} - \omega_{\rm s} \ll \omega_{\rm s}$ as the SBS frequency spacing between optical pump and Stokes waves is often a few GHz. Once the total SBS gain, $G_{\rm SBS} = g_{\rm m} P_{\rm p}$, exceeds the optical loss ($\alpha$), i.e., there is a net SBS gain, the Stokes wave grows as

$$P_{\rm s}(L) = P_{\rm s}(0)\, \exp(g_{\rm m} P_{\rm p} L_{\rm eff} - \alpha L), \tag{5.3}$$

in which $P_{\rm p}$ is the (non-depleted) input pump power and $L_{\rm eff} = (1 - \exp(-\alpha L))/\alpha$. Eq. (5.2) reveals that to achieve the maximum gain (i.e., $g_m$) the integral overlap between the optical force and the acoustic mode over the cross section of the structure (A) (i.e., $\langle \mathbf{f}, \mathbf{u}_{\rm m} \rangle = \int_A \mathbf{f}^* \cdot \mathbf{u}_{\rm m} da$) has to be maximized. This necessitates tight localization of optical and acoustic modes along with a large optical force whose profile matches the displacement profile of the acoustic mode. Additionally, Eq. (5.2) emphasizes the importance of optical loss and mechanical quality factor in lowering the threshold power. As a result, different materials and designs have been investigated for low-loss tight confinement of optical and acoustic waves.

To achieve a large optical force, a large refractive index contrast is needed. This is the motivation behind using free-standing Si nanowires [50, 54, 147] that confine both acoustic and optical waves via total internal reflection. However, Si nanowires suffer from linear

losses (i.e., scattering loss) and nonlinear losses (such as two-photon absorption (TPA) and TPA-induced free-carrier absorption [54, 148]) that may stifle efficient on-chip SBS generation. Some other proposed platforms like $CaF_2$ or silica either are not suitable for integrated photonics or possess small refractive index contrasts. Among several alternative materials, silicon nitride (SiN) is a promising platform as it is fully compatible with integrated photonics technology with a relatively large refractive index, wide transparency window (i.e., from visible to infrared wavelengths), and ultra-low optical losses [149]. Wider transparency window in SiN permits SBS interaction at shorter optical wavelengths (not possible in Si and chalcogenide structures) and allows the use of low-noise solid-state lasers [77, 150] at these wavelengths. In addition, high-tensile stress in low-pressure-chemical-vapor-deposited (LPCVD) SiN allows extremely low phononic losses [151, 152, 66, 153], enabling higher SBS gains.

## 5.2 Design of the phononic crystal structure

Figure 5.1(a) shows the schematic of a free-standing SiN nanowire, and the corresponding phononic dispersion diagram of its acoustic modes propagating along the y direction calculated using the finite element method (FEM) implemented in COMSOL. The dispersion diagram is extracted by applying Floquet periodic boundary conditions on the boundaries perpendicular to the y axis (see Fig. 5.1(b)). Figure 5.1(b) depicts the displacement profiles of different bands in the nanowire phononic dispersion diagram at normalized wavenumbers $K_m a = 0.01$ and $0.3$.

Investigation of the phononic bands starting with $\Omega_m(K_m = 0) = 0$ (i.e., the blue curves in Fig. 5.1(a)) reveals that the polarization of bands 1 and 2 are shear vertical and shear horizontal, respectively. Band 3 is a torsional mode resulting from mixing bands 1 and 2 via the boundaries of the nanowire, and band 4 is a longitudinal mode. Since the polarizations of bands 1–4 resemble those of the acoustic modes in bulk material (that are utilized in conventional Brillouin scattering), we refer to them as Brillouin-like acous-

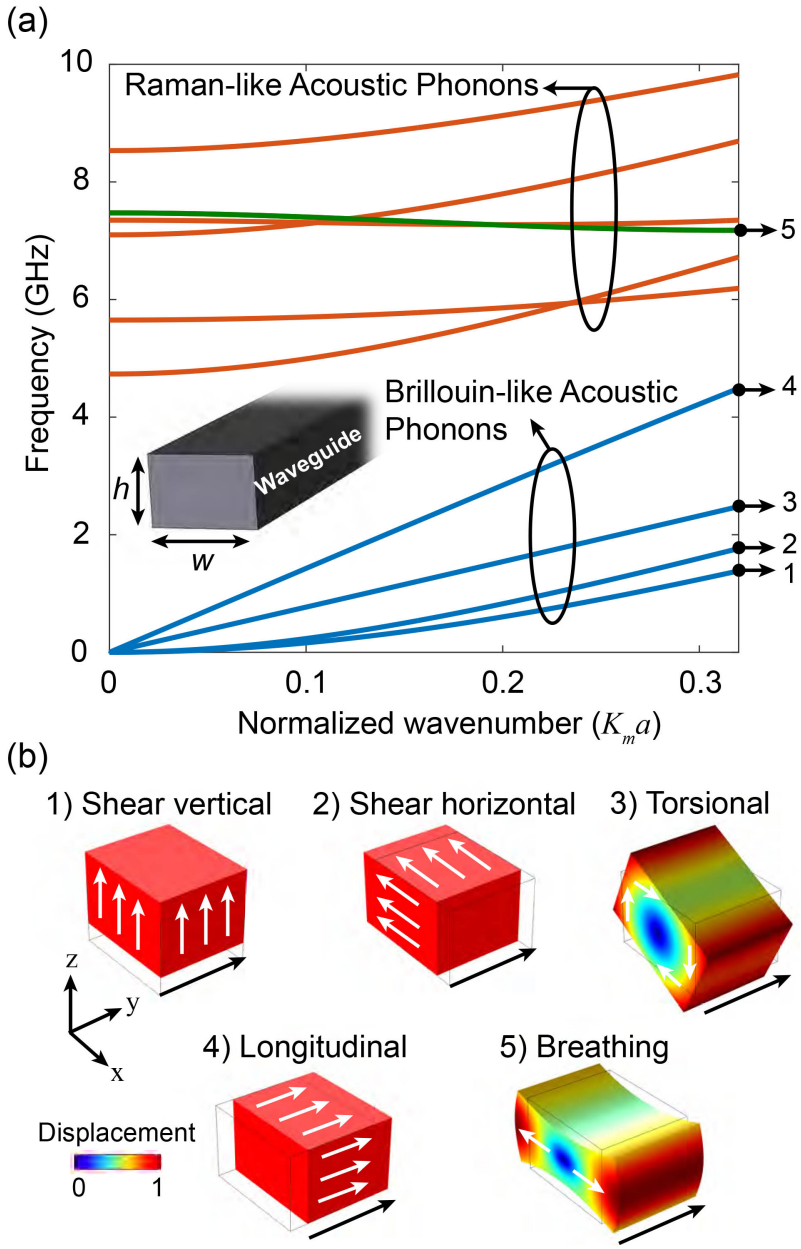


Figure 5.1: Phononic dispersion diagram of a free-standing SiN nanowire. (a) Phononic dispersion bands of a nanowire with ($w$, $h$) = (600, 400) nm and ($E$, $\nu$, $\rho$) = (250 GPa, 0.25, 3100 kg/m$^3$). $E$, $\nu$, and $\rho$ are Young's modulus, Poisson's ratio, and mass density, respectively. The acoustic wavenumber is normalized to "$a$", which is the length of the simulated portion of the waveguide (i.e., $a$ = 500 nm ); Dispersion bands can be classified as Brillouin-like acoustic phonons and Raman-like acoustic phonons based on the starting frequency at $K_m a = 0$. (b) Vibration profiles and propagation direction (i.e., along the y direction) of the acoustic modes of the SiN nanowire at $K_m a = 0.3$ for bands 1–4 and $K_m a = 0.01$ for band 5 in (a). White arrows depict the dominant vibration direction.

tic phonons. However, the phononic bands with $\Omega_m(K_m = 0) \neq 0$ (i.e., red curves in Fig. 5.1(a)) resonate transversally between boundaries of the nanowire at smaller wavenumbers and gradually tend to be traveling as wavenumber increases. As these red bands in Fig. 5.1(a) behave similar to optical phonons in the vicinity of $K_m = 0$, we refer to them as Raman-like acoustic phonons [53]. By expanding the structure from nanowire to bulk with no boundaries, Raman-like acoustic phonons merge with Brillouin-like acoustic phonons and what remain are the three fundamental types of acoustic plane waves: longitudinal, shear vertical, and shear horizontal.

Among Raman-like acoustic modes, the breathing acoustic mode (i.e., the green band 5 in Fig. 5.1(a)) yields the highest interaction with the fundamental guided photonic mode (i.e., $TE_1$) of the SiN nanowire. This is because the cross-sectional variation of the displacement profile of these breathing acoustic modes closely matches the profile of the radiation pressure of the photonic mode, which is normal to the surface of the optical waveguide. This greatly enhances the SBS gain (because of $g_m \propto |\langle \mathbf{f}, \mathbf{u}_m \rangle|^2$) and reduces the threshold optical pump power for nonlinear processes (e.g., phonon lasing) compared to other acoustic modes of the structure. The mechanical resonance frequency of these Raman-like breathing modes in sub-micron-size dimensions for SiN devices falls in multi-GHz frequency ranges.

The need for a mechanical support in a practical structure results in acoustic loss through the support that will reduce the overall SBS gain. To overcome this challenge, in my design, the optimal SiN nanowire is held in place by adding a PnC structure on the two sides (see Fig. 5.2(a)) exhibiting a phononic bandgap (PnBG) at the desired range of frequencies, which provides the support for the nanowire and yet confines the acoustic phonons to the SiN optical waveguide region at bandgap frequencies for strong photon-phonon interaction. Compared to the structures confining the generated acoustic phonons through the acoustic refractive index contrast between the waveguide and substrate (e.g., [51]), membrane structures enable tighter confinement because there is no decaying tail

for the acoustic modes to the surrounding environment (unless through the membrane). The application of the PnC structure, furthermore, limits the number of confined acoustic modes to those over a certain range of frequencies within the PnBG, culminating in a smaller resonant mode as compared to membrane-based nanowires suspending with arms at far distances [50], which are in general acoustically highly multi-mode. Therefore, PnCs prevent the formation of SBS at frequencies outside the PnBG because of the small overlap between the associated vibration profile with the optical force, which is highly localized to the optical waveguide region, yielding an extremely small SBS gain (i.e., $\langle \mathbf{f}, \mathbf{u}_m \rangle \approx 0$). This minimizes the competition between different acoustic modes in SBS, resulting in SBS with a cleaner spectrum and lower threshold power.

The mechanism of phononic confinement in a pillar-based PnC is the Bragg reflection that is enhanced by local resonances of the SiN pillars [31]. Due to the large optical refractive index contrast between SiN and air, a small distance between the PnC structure and the SiN nanowire in Fig. 5.2(a) is enough to make sure that the guided optical modes of the SiN waveguide do not interact with the PnC pillars. Since the pillars in the structure (see Fig. 5.2(a)) do not scatter the guided photons, the design of the line defect inside the PnC (which effectively forms a PnC cavity) is independent of the design of the optical (SiN) waveguide. This simplifies the design procedure.

To design the PnC cavity, I first optimize a unit cell of the triangular pillar-based PnC (see Fig. 5.2(a)) to support a wide PnBG with a center frequency close to resonance frequency of the desired breathing acoustic mode of the free-standing SiN nanowire. After designing the unit cell, I create a phononic defect by removing a few rows of pillars from the perfect PnC and replacing them with the SiN nanowire (i.e., the center region in Fig. 5.2(a)). The resulting structure can be visualized as a SiN nanowire with side pedestals surrounded by two perfect PnC regions (see Fig. 5.2(a)). The width of the PnC line defect is then finely adjusted to support a breathing-like acoustic mode possessing the maximum breathing vibration inside the optical waveguide. For ease of fabrication, I assume the

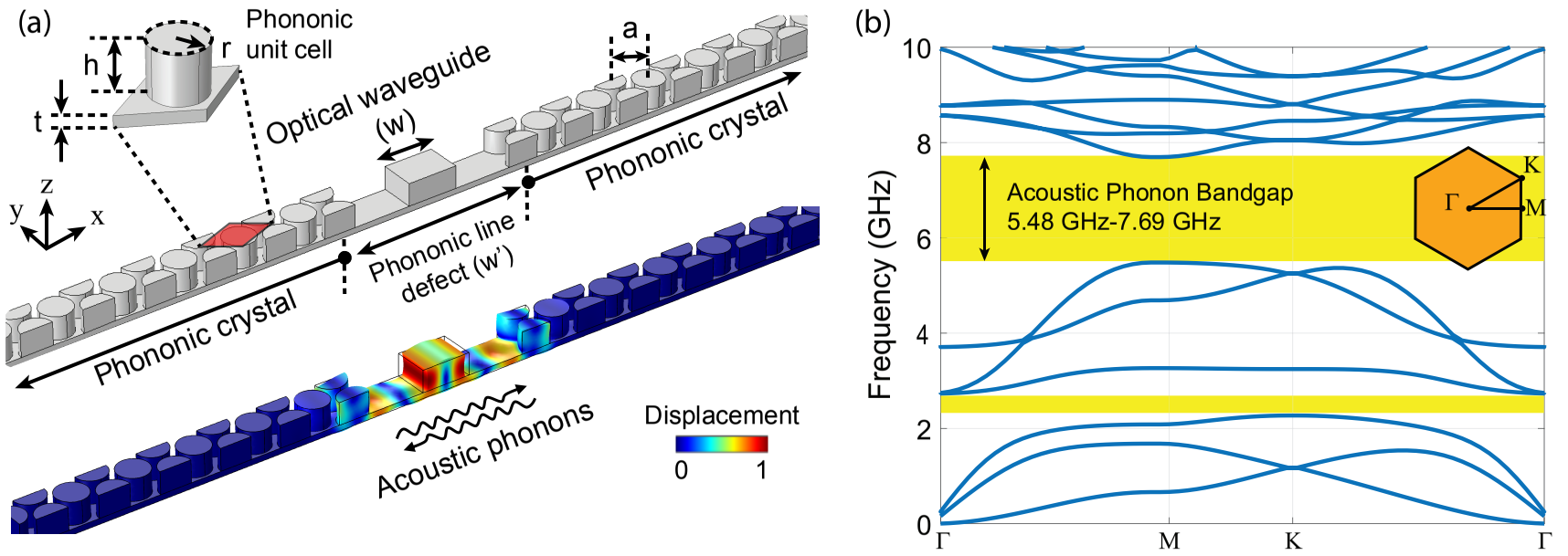


Figure 5.2: Proposed SiN structure for the SBS interaction. (a) The schematic of the pillar-based SiN waveguide for SBS generation, showing the phononic crystal and the optical ridge waveguide along with the vibration profile of the breathing acoustic mode confined inside the phononic bandgap of the PnC. The PnC is formed by a triangular lattice of SiN pillars standing on a thin SiN membrane. The phononic line defect is designed such that the breathing vibration is maximized inside the optical waveguide. The displacement profile in (a) is at normalized wavenumber $K_m a \approx 0$. (b) Phononic dispersion diagram of a primitive unit cell of the PnC (highlighted in (a)) over an irreducible Brillouin zone (shown in the inset of (b)). The pillars' height, radius, and membrane thickness are $(h/a, r/a, t/a)$=(0.64, 0.44, 0.16), respectively.

height of the pillars and the waveguide to be identical, which then allows to fabricate the whole structure using a single lithography-and-etching step without the need for separately aligning pillars with the SiN waveguide. This is very important when fabricating a long waveguide as a minor misalignment between the waveguide and the PnC can significantly change the spectrum of SBS and make the Stokes linewidth broader. As an example, using a search through FEM simulations, for the optical waveguide width of $w = 0.7$ $\mu$m (see Fig. 5.2(a)), I chose $a = 0.5$ $\mu$m, $r = 0.22$ $\mu$m, $h = 0.32$ $\mu$m, and $t = 80$ nm for the PnC structure whose dispersion diagram is shown in Fig. 5.2(b) demonstrating a large PnBG in the 5.48 – 7.69 GHz frequency range. I also selected the width of the phononic line defect $w' = 2.77$ $\mu$m because it yields stronger breathing vibration inside the selected optical waveguide width, which accordingly maximizes the overlap between the confined acoustic mode and the guided photonic modes in the optical waveguide width of $w = 0.7$ $\mu$m.

## 5.3 Optical forces and SBS gain calculations

Traditional SBS theory [154] only captures the bulk-induced nonlinearity (i.e., the electrostriction effect —the material density variation in response to the light intensity, which accordingly affects the material permittivity) and treats optical and acoustic waves as plane waves. However, as the cross-section of the waveguide scales down, plane-wave-approximated SBS is no longer valid because it misses the boundary-induced nonlinearities primarily caused by radiation pressure that plays a major role in SBS at nanoscale structures.

Recent studies [145] predict a large enhancement of SBS in nanostructures as a result of the boundary effects, which add to the SBS caused by electrostriction effect. In fact, traveling photons inside a structure with nanoscale cross section exert a noticeable optical pressure normal to the boundaries of guiding region formulated as [146]

$$\mathbf{f}\,(\mathbf{r}) = (\frac{-1}{2}\Delta\epsilon\; E_{\text{pt}}(\mathbf{r})E^{*}_{\text{st}}(\mathbf{r}) + \frac{1}{2}\Delta(\epsilon^{-1})D_{\text{pn}}(\mathbf{r})D^{*}_{\text{sn}}(\mathbf{r}))\;\hat{\mathbf{n}}\;\delta(\mathbf{r}-\mathbf{r}_{\Omega}), \tag{5.4}$$

derived from the Maxwell stress tensors (MSTs). In Eq. (5.4), $E$, $D$, and $\Delta\epsilon$ denote the electric field amplitude, the electric displacement field amplitude, and the difference in the permittivity across the boundaries, respectively; subscripts $t$ and $n$ refer to the tangential and normal components, subscripts $p$ and $s$ refer to the pump and Stokes waves, respectively. In addition, $\mathbf{r}$ is the position vector and $\hat{\mathbf{n}}$ represents the unit vector normal to the boundaries of the waveguides; and $\delta(\mathbf{r})$ is the Dirac delta function. The force is non-zero only at the boundaries of the waveguide (i.e., $\mathbf{r} = \mathbf{r}_\Omega$) and pointing from the high-index region (larger $\epsilon$) to the low-index region (smaller $\epsilon$). MSTs can also induce a body force inside optical waveguides if the refractive index varies across the cross-section, which is not the case for our structure.

To calculate the force and the overlapping integral between the optical and acoustic modes of the structure shown in Fig. 5.2(a), I first use the FEM to simulate the optical and acoustic modes (and their corresponding frequencies and field profiles) using eigen-mode analysis. Then these modes are imported in the vectorial format into an in-house MATLAB code to calculate the optical force using Eq. (5.4), and then the overlapping integral between optical and acoustic modes to find the SBS gain as formulated in Eq. (5.2). Here, I consider forward SBS (FSBS) in which pump and red-shifted Stokes waves are co-propagating as the designed PnC structure supports a Raman-like acoustic mode within its PnBG.

Considering the energy and momentum conservations in FSBS (i.e., Eq. (5.1)) when pump and Stokes waves are from the same optical dispersion band, we obtain

$$K_{\mathrm{m}} = k_{\mathrm{p}}(\omega_{\mathrm{p}}) - k_{\mathrm{s}}(\omega_{\mathrm{s}}) = \Omega_m \frac{\partial k}{\partial \omega} = \Omega_m / v_g, \tag{5.5}$$

where $v_g$ is the group velocity of the optical waves. Therefore, to satisfy the phase matching condition in the FSBS, the phononic structure should support an acoustic mode with acoustic phase velocity that matches the group velocity of the engaged optical modes. The nonzero frequency of the Raman-like modes at zero wavenumber and the flat nature of their

band structure will ensure the phase matching condition. Owing to the fact that the frequency of the Raman-like breathing acoustic mode is several orders of magnitude smaller than the frequency of the optical pump and Stokes modes (i.e., $(\omega_p - \omega_s)/\omega_p \ll 1$), we can assume in the structure that the optical mode profile of the incident pump and Stokes modes are similar.

Figure 5.3(a) shows the magnitude of the FSBS gain in free-standing nanowires as a function of the waveguide width (i.e., w) simulated for the breathing acoustic mode at $\lambda_{opt} = 1.55$ $\mu$m. As shown in Fig. 5.3(a), the maximum radiation pressure gain normalized to the mechanical quality factor of the acoustic mode (i.e., $g_{\text{m}}/Q_{\text{mech}}$) is achieved for a SiN waveguide with $h = 400$ nm and $w = 550$ nm, which is $g_{\text{m}}/Q_{\text{mech}} = 0.06$ $(\text{W.m})^{-1}$. Figure 5.3(a) highlights the importance of tight localization, i.e., the smaller width of the waveguide results in a larger SBS gain or a stronger photon scattering due to the generated SBS acoustic phonons. For waveguides with widths smaller than 0.5 $\mu$m, the light confinement inside the physical cross section of the SiN nanowire is considerably reduced, resulting in a reduction in the integral overlap of optical and acoustic modes, and therefore, the SBS gain.

In Fig. 5.3(a), I also compare the normalized SBS gain (i.e., $g_{\text{m}}/Q_{\text{mech}}$) in the PnC-assisted structure with SiN nanowire. To calculate the gain in the PnC-assisted structure as a function of the width, the PnC is accordingly adjusted to have the breathing frequency at the middle of its PnBG. The smaller value of $g_{\text{m}}/Q_{\text{mech}}$ in the PnC-assisted structure can be attributed to the emerging flexural vibration in the pedestal (see Fig. 5.3(b)), which slightly delocalized the acoustic mode from the optical waveguide. In fact, the flexural vibration does not significantly scatter light compared to breathing vibration because it preserves the total area of the nanowire cross-section. However, the PnC membrane provides lossless support for the SiN waveguide and better structural stability compared to the bare SiN waveguide with arms at far distances. This enables fabrication of longer SBS waveguides leading to a larger power in the Stokes wave.

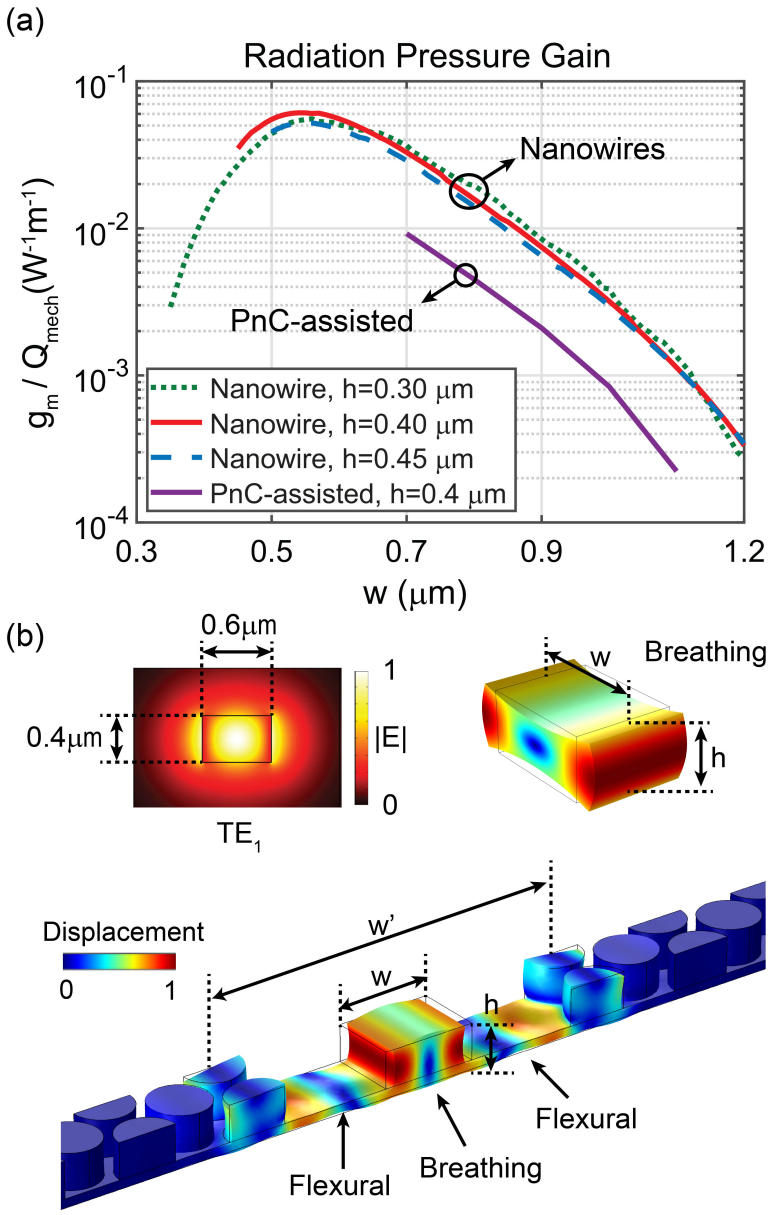


Figure 5.3: FSBS gain in SiN nanowires and PnC-assisted SiN waveguides. (a) Variation of the FSBS gain in the SiN nanowire for the acoustic mode shown in (b) as a function of its width (w) for three different heights ($h = 0.3$ $\mu$m, $h = 0.4$ $\mu$m, and $h = 0.45$ $\mu$m). In addition, the FSBS gain for a PnC-assisted waveguide with the total thickness of 400 nm is compared with that of different nanowires. The gain slightly reduces because of the extension of the acoustic waves to the pedestal. (b) The acoustic breathing vibration mode and the electric field of the fundamental TE optical mode (i.e., $TE_1$ whose electric field lies in the plane of the nanowire) used in the simulation of the FSBS gain of nanowires. In addition, the breathing-like acoustic vibration mode inside the PnC-assisted waveguide is depicted, which is a combination of two primary vibrations: breathing and flexural.

Table 5.1: Comparison of SBS gain and linear optical loss between different optical structures.

| Structure | $g_m$ [$W^{-1}{\cdot}m^{-1}$] | Linear optical loss [$dB{\cdot}cm^{-1}$] |
|---|---|---|
| Si nanowire [147] | 1152 | 0.18 |
| Si nanowire [54] | 6561 | 5.5 |
| Single-mode fiber [155] | 0.14 | 0.2 |
| $As_2S_3$ waveguide [51] | 310.8 | 0.8 |
| This work (Theory) | 500 | 0.1 |

It has been shown that the high tensile stress in LPCVD-deposited stoichiometric SiN results in extremely high mechanical quality factors ($Q_m$-frequency product $> 2 \times 10^{13}$ [66]) at room temperature and ($Q_m$-frequency product $> 3 \times 10^{15}$ [153]) at millikelvin temperatures in SiN membranes. Therefore, having additional PnC to prevent anchor loss (or phononic leakage) makes $Q_{\mathrm{m}} \approx 10^4$ a reasonable prediction at GHz frequencies for SiN membrane. Therefore, we expect that the SBS gain around $g_{\mathrm{m}} = 600$ can be achieved in tensile-stress SiN. In addition, the presence of the PnC structure eliminates several undesired acoustic modes that naturally exist in the nanowire structures, which can result in the generation of unwanted Stokes modes. Thus, the proposed PnC-assisted structure improves several properties of a single nanowire for SBS generation.

Table 5.1 compares the (forward/backward) SBS interaction in different optical structures in terms of the SBS gain ($g_m$) and linear optical loss. As it is clear, single-mode fiber has the lowest SBS gain among the structures because of the loose confinement of the engaged optical and acoustic modes. However, thanks to the low loss of optical fibers, SBS is still observed although over several kilometers lengths. By shrinking the cross section of optical structures, we generally observe that the SBS gain is increased; however, the tighter cross-section confinement introduces additional scattering optical losses. In particular, in the case of the Si nanowires listed in Tab. 5.1, the increasing SBS gain incurs (significantly) higher optical loses. Therefore, even though the SBS gain in SiN is not as high as the Si structures, the lower optical losses in SiN can compensate the difference and enable promising on-chip SBS devices with low threshold powers.

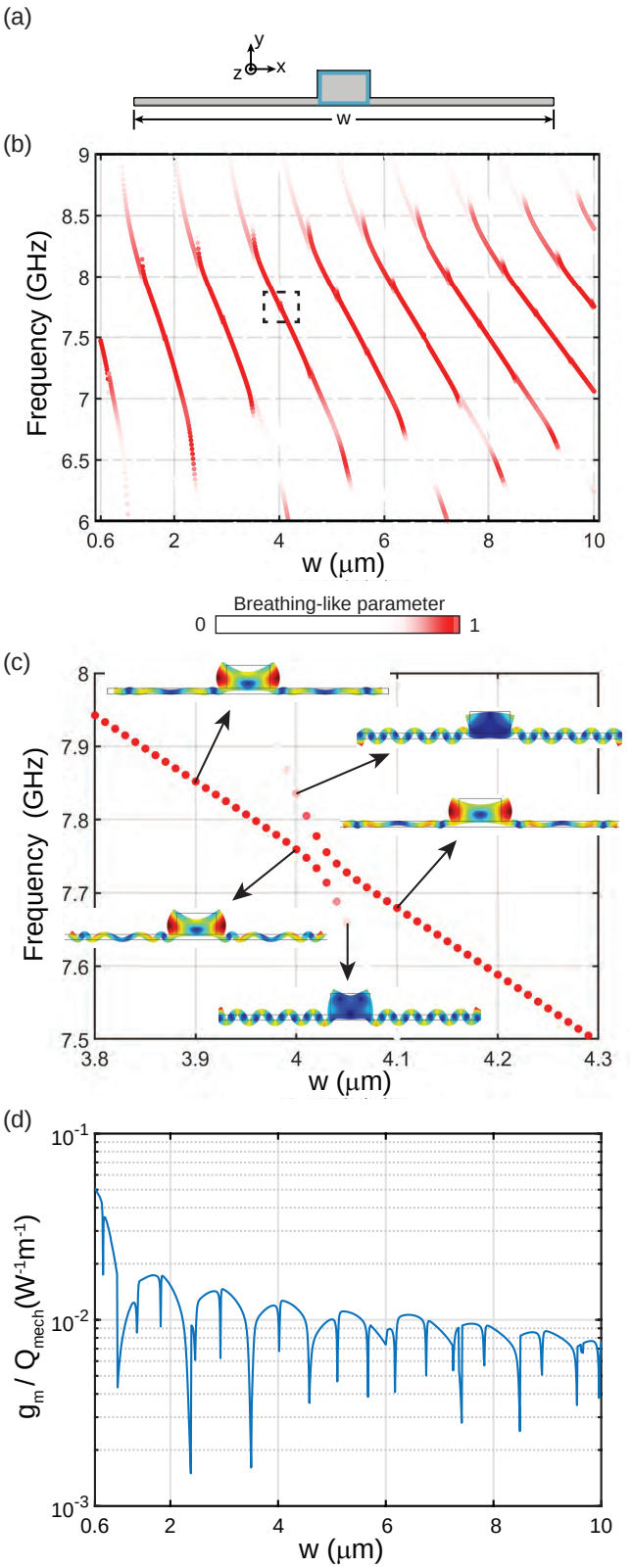


Figure 5.4: Properties of a SiN nanowire on a membrane without PnC. (a) The cross-section of the nanowire (height = 400 nm and width = 600 nm) on a membrane with the width of $w$ and the height of 80 nm. (b) The breathing-like acoustic modes of the structure shown in (a) at $K_m = 0$ for different membrane widths. The color code for the representation of the acoustic resonances is the "breathing-like parameter". (c) Zoomed version of a resonance mode of the structure in (a) in the region identified by the dashed black square in (b) demonstrating mode-splitting (or avoided crossing) due to the coupling between a breathing-like acoustic branch and other acoustic branches of the structure. (d) The FSBS gain calculated for the closest mode of the structure in (a) to the breathing mode of an ideal nanowire (i.e., the mode with the largest "breathing-like parameter" in (b)) as a function of $w$.

In order to further highlight the benefits of integrating the membrane structure with PnCs, I also study the FSBS gain in a nanowire sitting on a membrane without PnCs (see Fig. 5.4(a)). Because the nanowire-on-membrane structure (Fig. 5.4(a)) with infinite width ($w$) does not support a breathing mode confined inside the nanowire, I calculate the FSBS gain for membrane structures with finite width. In Fig. 5.4(b), the acoustic resonances of this structure as a function of $w$ are shown and color-coded based on the "breathing-like parameter", which is the overlap integral over the region specified in Fig. 5.4(a) between the normalized field patterns of the acoustic resonance mode of the nanowire-on-membrane structure and that of the corresponding ideal nanowire (a free-standing nanowire with no membrane) with the same height and width. Figure 5.4(c) illustrates the zoomed version of Fig. 5.4(b) around $w = 4\ \mu m$, which shows an avoided crossing (or mode splitting) between different acoustic branches. The simulated mode profiles of different points on the band structure in Fig. 5.4(c) reveals the transition of the acoustic mode families across the avoided crossing. Figure 5.4(d) shows variation of the FSBS gain as a function of $w$ for the breathing-like vibration and illustrates that by extending the width of the structure, the FSBS gain reduces owing to the lower concentration of the acoustic mode energy (or power) in the form of breathing vibration inside the optically relevant region (i.e., nanowire). This highlights one of the benefits of the PnC-based structure that enables confinement of the (breathing) acoustic modes to the optical region. In addition, Fig. 5.4(d) reveals that the FSBS gain drops when breathing acoustic modes transition from one acoustic branch to another acoustic branch of the structure.

I should also highlight that in addition to radiation pressure, electrostrictive force also contributes to the SBS interaction and could be significant as those in silicon nanostructures. However, there is no reported measurement on the photo-elastic coefficients of SiN [41] that allows me to incorporate them in my study.

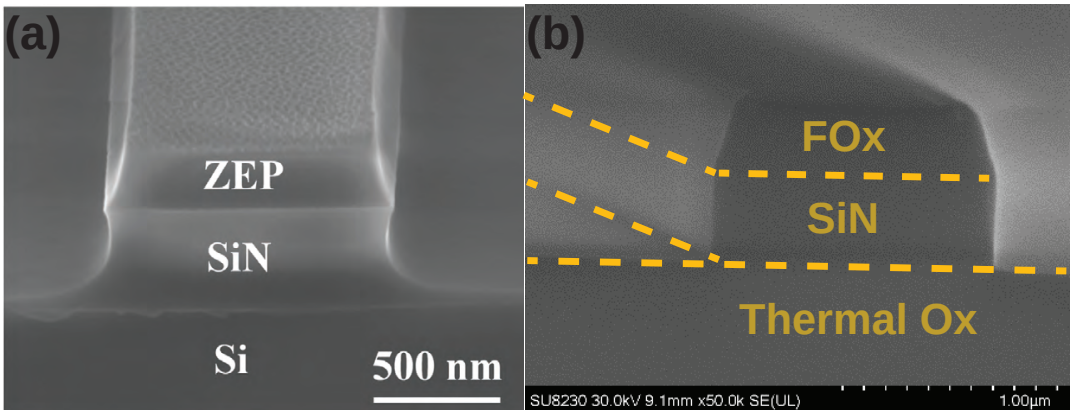


Figure 5.5: (a) Etching SiN devices using an RIE recipe [149]. (b) Etching SiN using the developed ICP etching recipe. It clearly shows the sidewalls of the ICP etching are much more vertical compared to the RIE recipe.

## 5.4 Fabrication of membrane-based SBS PnC devices

My PnC-based SBS membrane devices in SiN require a very smooth and vertical sidewall for the fabrication of very low loss optical structures as well as the fabrication of the hypersonic pillar-based PnC structure. The previously-optimized SiN RIE etching, shown in Fig. 5.5(a), yields extremely low-loss optical devices [149]. However, the tail of the sidewalls in the RIE etching does not allow to fabricate the dense hypersonic PnCs structure. Therefore, I developed an ICP etching recipe for fabricating SiN devices in an $Ar/O_2/CF_4$ chemistry as shown in Fig. 5.5(b). I use a high-resolution FOx e-beam resist to create a hard etching mask for the SiN devices prior to ICP etching.

Another challenge to fabricate SBS SiN devices was to release several microns of high-stress LPCVD SiN. The SiN releasing process should meet the following two requirements: 1) an (extremely) high selectivity between the SiN film and the underlying substrate to not damage the SiN devices during etching of the substrate, and 2) a very slow rate for LPCVD SiN undercutting to let the accumulated stress inside the high-stress SiN to be released gradually during undercutting as the sudden releasing of the stress breaks the SiN thin structures. After examining several releasing options [i.e., using buffered oxide etch (BOE), xenon difluoride ($Xef_2$), and potassium hydroxide (KOH)], KOH wet etching was

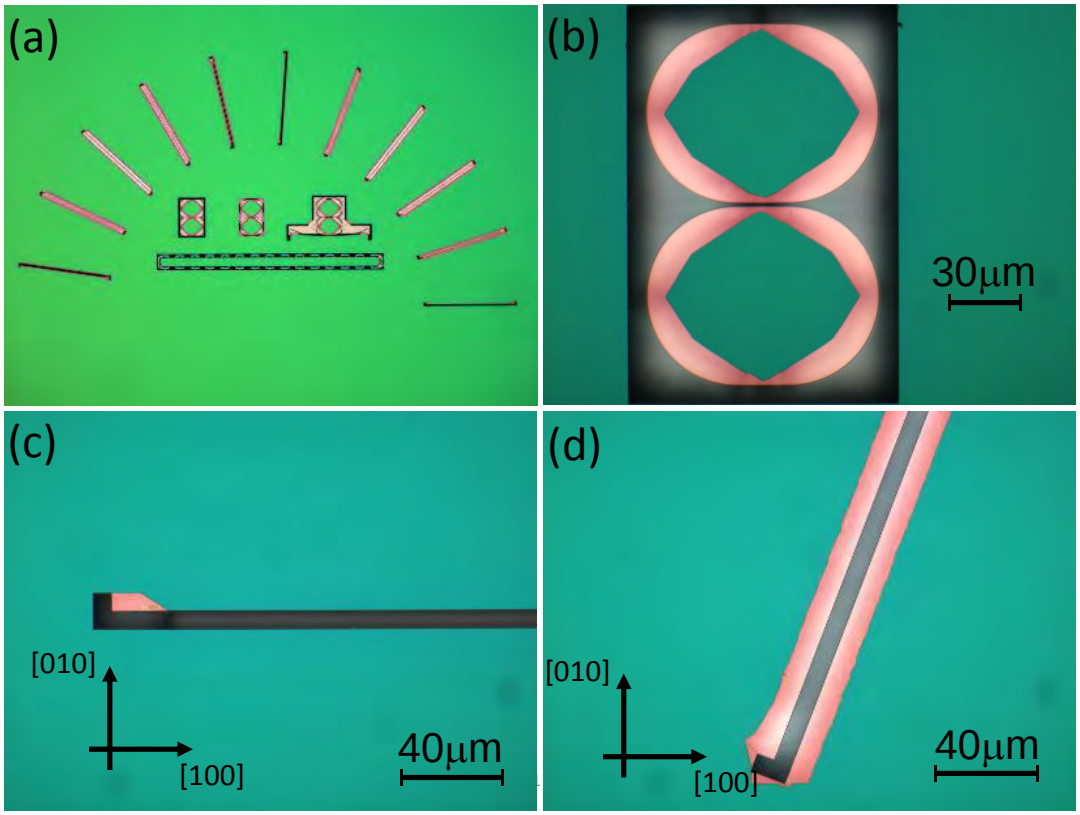


Figure 5.6: KOH wet releasing of SiN structures on Si after 22 hours in normal temperature at cleanroom. (a) Different SiN devices patterned on Si. (b) Releasing a double-disk SiN structure. (c) and (d) releasing waveguides patterned at different angles with respect to [100] direction.

selected for releasing SiN devices fabricated on Si because of the extremely high selectivity between SiN and Si in KOH wet etching, and the extremely slow etch rate of Si in KOH at cleanroom normal temperature (it usually takes about 15 hours for releasing SiN SBS structures on Si). Figure 5.6 show a number of test structures on a same Si chip patterned in a 400-nm-thick high-stress LPCVD SiN film. The bright region shows the extent of SiN undercutting. In contrast to $Xef_2$ that etches Si isotropically, KOH etches Si anisotropically (see Fig. 5.6(b)). This requires that SiN structures to be patterned along certain directions on Si. As Figs. 5.6(c) and 5.6(d) show, long waveguide structures have to be along the [110] direction.

# CHAPTER 6

# ON-CHIP OPTOMECHANICAL PHOTONIC RESONATORS IN DOUBLE-LAYER SILICON PLATFORMS

This chapter deals with the standing-wave vibrational modes at the RF frequencies that interact with the resonating optical modes inside a microcavity to enable the so called *cavity optomechanics*. Researchers, during the last two decades have extensively explore cavity optomechanics for diverse areas [157, 158] spanning from the quantum studies such as cooling of a mechanical object to its ground state [77, 78] and squeezing light [79] to the classical effects such as sensing [82] and RF oscillations [80, 81].

Here, I present the first report on the fabrication of the optomechanical cavities in a double-layer Si platform [156]. In these structures, the optical resonance modes (which form a photonic molecule) are extremely sensitive to the gap size because of the large refractive index of Si, as well as the tiny separation between layers. This collectively leads to a significant optomechanical interaction as compared to all alternative platforms. Moreover, these structures are able to be integrated with the existing integrated optical devices to enable novel on-chip optical systems for RF-photonic applications [159]. In this chapter,

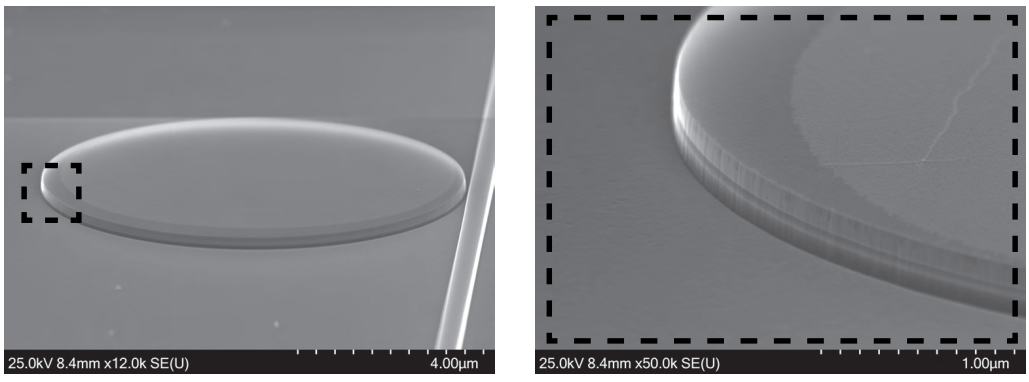


Figure 6.1: An optical microdisk resonator in the double-layer Si platform [156]. The thickness of the top and bottom Si layers are 110 nm that are vertically spaced by a 60-nm $SiO_2$ layer.

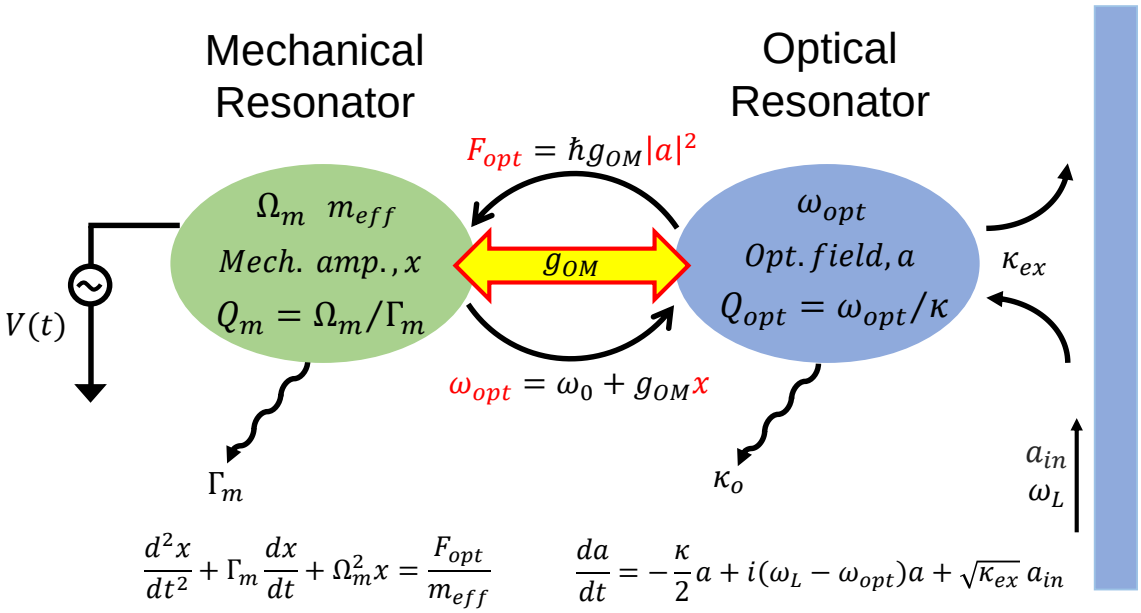


Figure 6.2: Optomechanical interaction between an (electro)mechanical and optical resonator along with the underlying classical equations.

I investigate particularly the above-threshold optomechanical oscillation in the fabricated double-layer structures with no external feedback as well as high-speed wideband-tunable optical resonators tuned by an electrical signal in telecom bandwidth.

Figure 6.1 shows an example of a microdisk resonator fabricated in the double-layer Si platform. The incorporation of the gap (by partially undercutting the sandwiched $SiO_2$) in these platforms enables the realization of novel cavity optomechanical structures, where the optical resonance frequency is a strong function of the gap size. Such sensitivity to the gap size (which has not been reported in any previous demonstrations) makes the fabricated double-layer structure a very promising candidate for the study of the optomechanical effects. The tiny gap ($\sim$ 60 nm) between the Si layers also allows for independently adjusting the optical and mechanical resonance frequencies.

These structures can also accommodate the application of an RF electrical signal that can capacitively excite the fundamental symmetrical flexural mechanical mode, thereby communicating with the resonating optical mode inside the structure. Figure 6.2 illustrates the optomechanical interaction in which the linear optomechanical coefficient (i.e., $g_{OM} =$

$\partial\omega/\partial x$, which indicates the sensitivity of the optical resonance mode to the gap variation as well as the amount of force exerted by a single photon ($F_{opt} = \hbar g_{OM}$, where $\hbar$ is the reduced Planck's constant)) which mediates the nonlinear coupling between the optical and mechanical resonance modes of the microcavity.

### 6.1 On-chip optomechanical oscillators

Resonating optical modes in a double-layer structure exert a gradient-based radiation pressure ($F_{opt}$) [160, 72, 73]. This force can be either attractive or repulsive force [160, 161] depending on whether the excited optical supermodes are bonding (or symmetric) or anti-bonding (or asymmetric). It has been shown that the gradient-based radiation pressure in the vertically stacked layers [73] is stronger than the scattering-based radiation pressure commonly observed in the single-layer (single-object) cavities [67, 80].

Using a slightly-detuned input laser with respect to the optical resonance frequency of the optomechanical microcavity causes the exerted optical force (gradient-based or scattering-based radiation pressure) to modify the mechanical resonance mode in the following ways [162]: 1) the modification of the mechanical resonance frequency (i.e., $\Omega_0 = \Omega_{OM} + \Omega_m$), and 2) the modification of the mechanical damping (i.e., $\Gamma_0 = \Gamma_{OM} + \Gamma_m$), where $\Omega_m$ and $\Gamma_m$ are the cold-cavity mechanical resonance frequency and damping, respectively, and $\Omega_{OM}$ and $\Gamma_{OM}$ are the shifts due to the existing optical forces. $\Omega_{OM}$ stems from the fact that the optically-induced stiffness $k = -\partial F_{opt}/\partial x$ adds to the intrinsic stiffness of the mechanical cavity. However, $\Gamma_{OM}$ is due to the retarded nature of the optical force which is delayed on the order of $\tau = Q_{opt}/w_{opt}$ (the photon storage time).

Depending on the detuning of the input laser, the mechanical damping modification ($\Gamma_{OM}$) can result in either the cooling of the mechanical resonator (when the input laser is red-detuned, $\omega_L < \omega_{opt}$) or the amplification of the mechanical vibration or *oscillation* (when the input laser is blue-detuned, $\omega_L > \omega_{opt}$). When the input laser is properly detuned and the power inside the microcavity is above the oscillation threshold power (which is the

power at which $\Gamma_0 = 0$), the following explains how the microcavities in the double-layer structures fall in oscillation leading to the modulation of the input light and creation of side-lobes at $\omega_L \pm \Omega_0$ (which requires $\delta\omega = 1/\tau > \Omega_0$ or the side-lobes lie within the linewidth). Closely-resonating input laser builds up light inside the optical cavity which accordingly intensifies the optical forces. The optical forces then deform the double-layer structure and reduce the gap if the resonating optical mode is symmetric, or the optical forces increase the gap if the resonating optical mode is antisymmetric [161]. In either of these scenarios, as the gap size is changing or the optical resonance frequency is shifting, the laser becomes progressively less resonating and therefore, the optical force weakens and eventually diminishes and the structure then goes back to its initial state. This process (or cycle) repeats at the frequency of the excited mechanical resonance mode which is usually in RF frequencies for microcavities without a need to any external (electric) feedback.

### 6.1.1 Fabrication of double-layer optomechanical Si devices

Figure 6.3 illustrates the process flow of fabricating optomechanical cavities in the double-layer Si platforms. The fabrication begins by first patterning a hard mask for etching waveguides and resonators. The hard etching mask for Si devices is usually HSQ (a negative e-beam resist). Recently, a new double-patterning hard mask has been developed [163] in which the pattern of devices is first transfered to a very thin layer of ALD $Al_2O_3$ from the HSQ mask by etching using a fluorine-based etching chemistry. This enables a hard mask with rounded corners compared to the single HSQ mask directly patterned by the electron beam. Then $Al_2O_3$ forms a hard-mask for etching optical devices. $Al_2O_3$ provides higher selectivity in chlorine etching chemistry compared to HSQ. In addition, compared to metal masks such as chromium, ALD $Al_2O_3$ has smaller grain sizes and therefore it yields a better resolution. Figure 6.1 shows a double-layer Si resonator etched using an $Al_2O_3$ hard mask.

After etching devices (Fig. 6.3: step 1), I deposit 20 nm ALD $SiO_2$ followed by 30

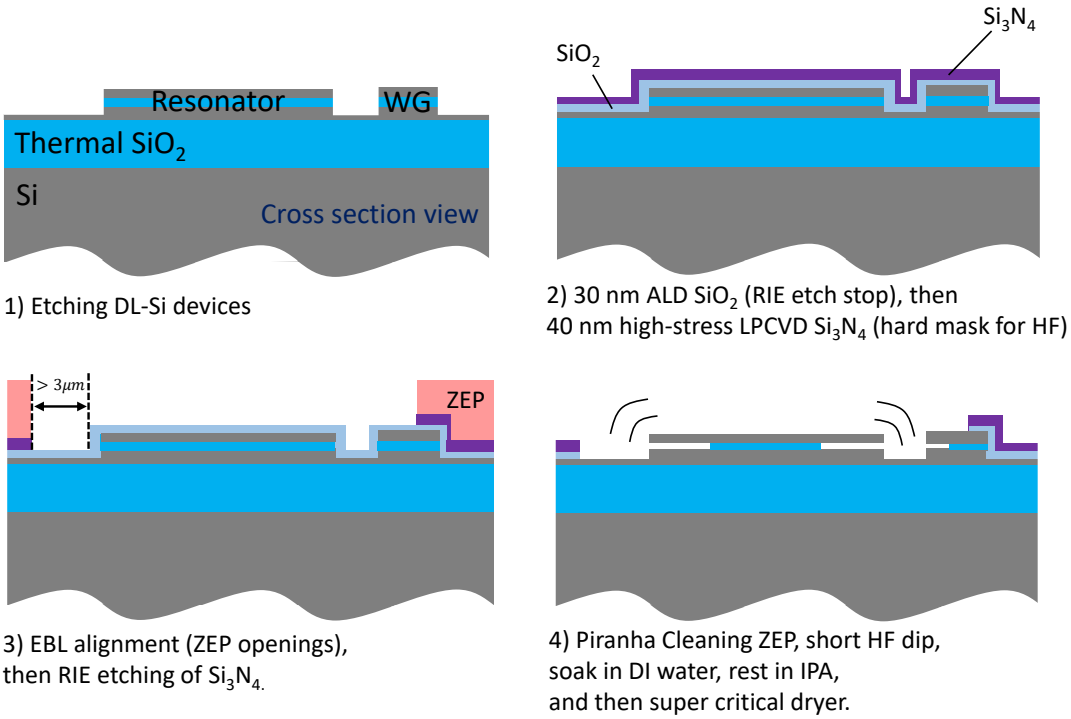


Figure 6.3: Overview of the process flow for the fabrication of the on-chip optomechanical devices in double-layer Si platforms.

nm high-stress LPCVD $Si_3N_4$ (Fig. 6.3: step 2). The ALD $SiO_2$ forms an etch-stop layer (protecting optical devices during etching $Si_3N_4$) and the LPCVD $Si_3N_4$ protects selected regions during the wet releasing of optical devices. The high-stress LPCVD $Si_3N_4$ has an advantage of high resistance to HF or BOE. Therefore, a thin-layer of $Si_3N_4$ is sufficient for protection. Besides, a thin layer of $Si_3N_4$ covering waveguides and coupling gratings after releasing does not introduce optical losses, nor does it significantly shift the optical

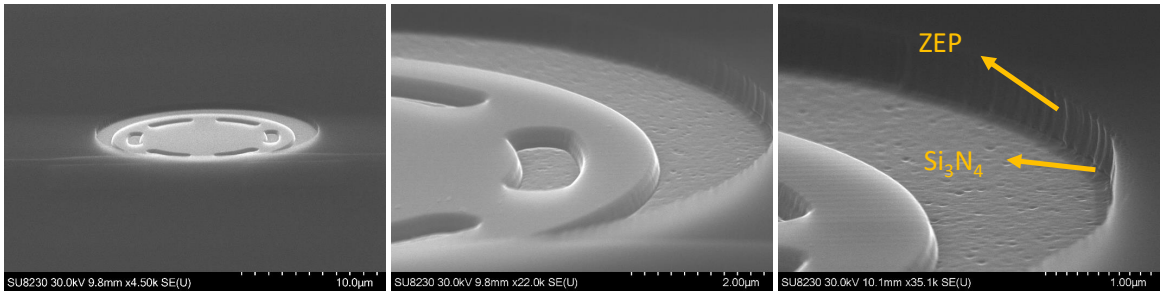


Figure 6.4: Fabricated double-layer optomechanical devices. SEMs show the devices in step 3 of the process flow (see Fig. 6.3).

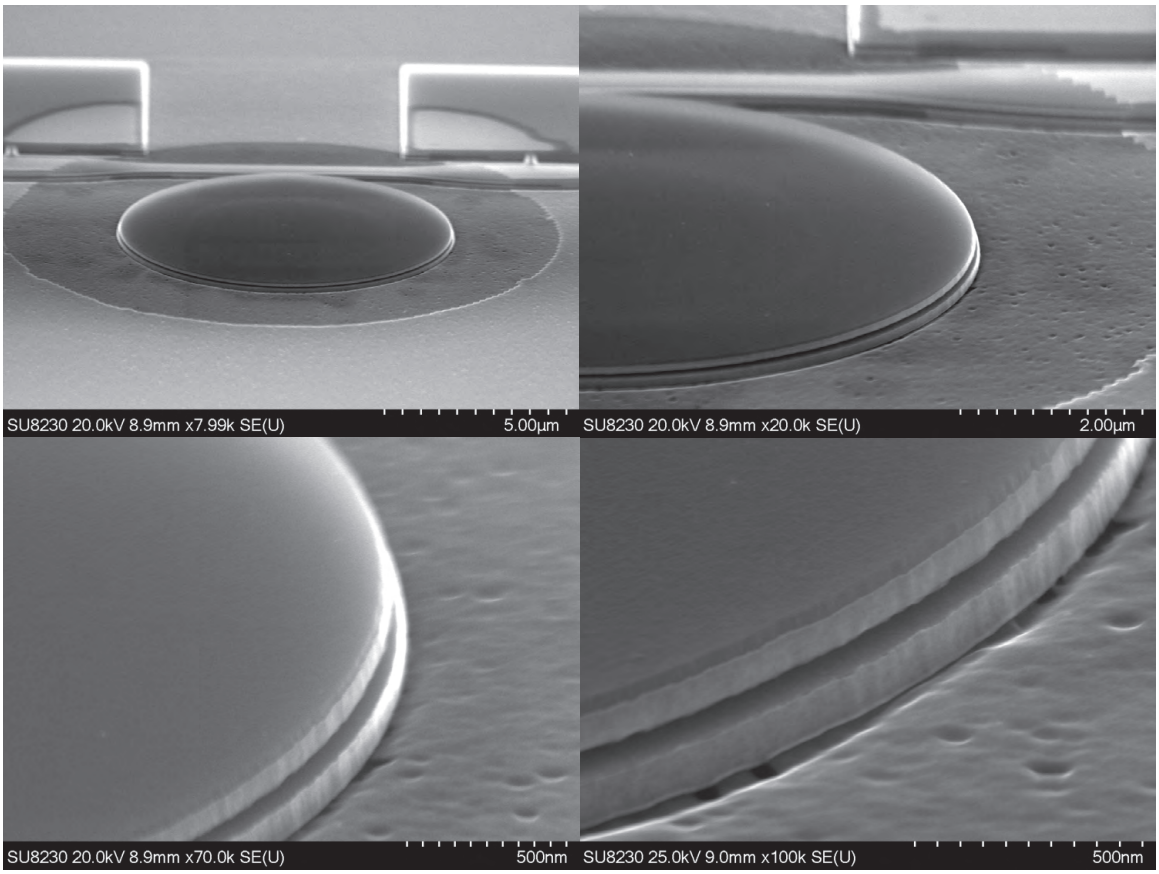


Figure 6.5: Fabricated double-layer optomechanical cavity after releasing (or partially undercutting the $SiO_2$ interlayer). All SEMs were taken at different angles from a single double-layer optomechanical cavity.

transmission of the coupling grating. The next step is patterning the $Si_3N_4$ by an EBL alignment to form openings in the positive-EBL-resist ZEP, followed by an RIE etching of $Si_3N_4$ (Fig. 6.4).

The residue of the ZEP after etching $Si_3N_4$ is then removed using the Piranha solution and the devices are released in the next step (Fig. 6.3: step 4). To release the devices (i.e., partial etching of the middle $SiO_2$ layer), I suspend the devices in pure hydrofluoric acid (HF) for $\sim$ 20 seconds, followed by immersing the devices in DI water for 20 minutes, and then in IPA over night. Eventually, the devices are dried out in a tousimis supercritical point dryer. Figure 6.5 shows the SEMs of final devices after releasing.

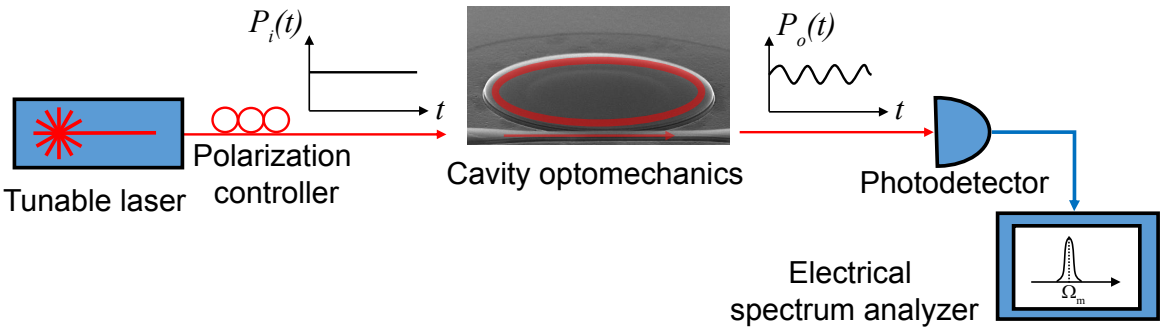


Figure 6.6: Characterization setup for the optomechanical oscillation when the input laser power is above the oscillation threshold.

### 6.1.2 RF characterization of on-chip optomechanical oscillators

The apparatus for the characterization of the optomechanical oscillation in the fabricated double-layer Si structures is shown in Fig. 6.6. After identifying the optical resonance wavelengths of the cavity by sweeping the tunable laser and looking at the optical transmission of the device, the laser is then blue-detuned to one of the optical resonances. The output of the laser first goes to the polarization controller to maximize the coupling of the light to the on-chip integrated grating couplers (originally designed for TE optical modes). The light then goes through the waveguide and coupled to the resonator at resonance. The transmitted (modulated) light ($a_{out} = a_{in} - \sqrt{\kappa_{ex}}a$, see Fig. 6.2) is then photo-detected and converted to an RF signal. By looking at the frequency content of the electrical signal using an electrical spectrum analyzer, the frequency of the vibrational resonance modes that efficiently interact with the circulating optical resonance mode are identified.

The lowest order vibrational resonance modes of a double-layer Si structure with the radius of 4.5$\mu$m and the $SiO_2$ undercut of 2$\mu$m are shown in Fig. 6.7(a). Due to the symmetry of the exerted optical force which is localized at the periphery of the resonator and pointing in the out-of-plane direction, only the fundamental flexural resonance mode is efficiently excited. Fig. 6.7(b) provides the simulation of fundamental flexural resonance mode (shown in the inset) as a function of the undercut for a double-layer microdisk with the radius of 4.5$\mu$m.

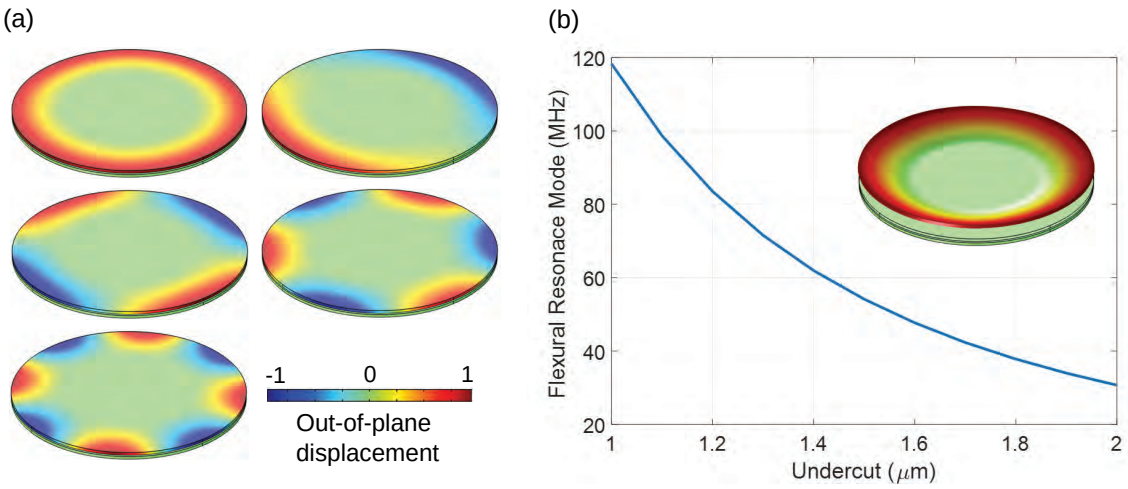


Figure 6.7: Lowest-order (standing-wave) flexural resonance modes of a double-layer structure. (a) Out-of-plane displacement profile of several flexural resonance modes in a microdisk double-layer Si resonator with the radius of 4.5$\mu$m. The bottom layer is fixed while the top layer is free to deform. (b) Variation of the resonance frequency of the fundamental flexural resonance mode as a function of the undercut.

Fig. 6.8 provides the optical and RF characterization of a fabricated double-layer Si structures with the input laser power above the oscillation threshold with no external feedback. The RF characterization reveals the optical force excites a flexural vibration mode at 75 MHz. It is worth noting that the characterization of the devices at vacuum and low temperature results in higher mechanical quality factors [164]. Because of the 60 nm gap inside the double-layer structure, squeezing thin-film damping is one of the major sources of phononic loss in the structure that can be mitigated by operation at vacuum, which accordingly further lowers the threshold power of the optomechanical oscillation.

Figure 6.9 shows the characterization of another double-layer Si structure for different input power, with a lower threshold power as well as a lower oscillation frequency compared to Fig. 6.8. Additionally, Fig. 6.9 shows that by increasing the input power the frequency of the oscillation slightly increases which is another indication of an optomechanical interaction. It is worth noting that the RF characterizations shown in Figs. 6.8 and 6.9 have been obtained without using an erbium-doped fiber amplifier (EDFA).

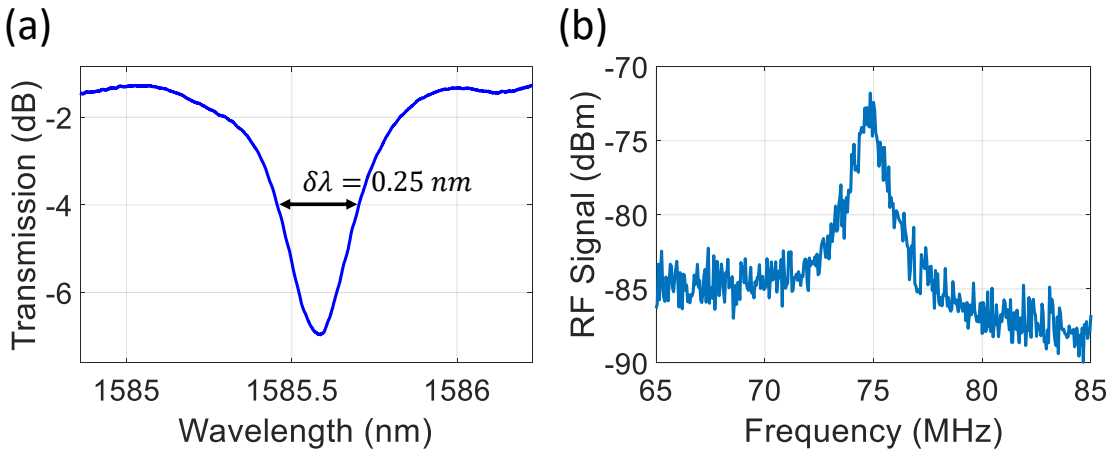


Figure 6.8: Characterization of an optomechanical double-layer Si microdisk with the radius of 4.5$\mu$m. (a) Optical transmission of the device at low input power, and (b) RF characterization of mechanical resonating mode at input laser power above the oscillation threshold.

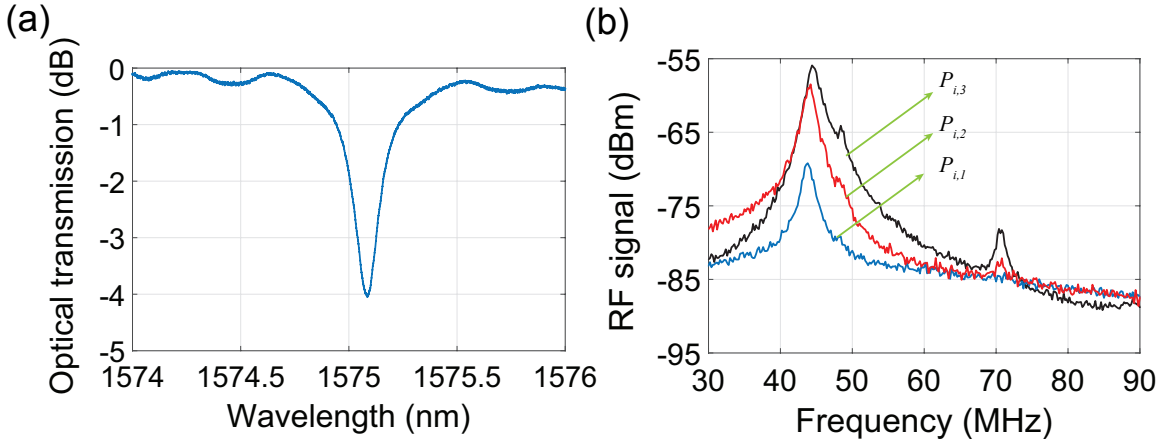


Figure 6.9: Characterization of an optomechanical double-layer Si microdisk with the radius of 4.5$\mu$m. (a) Linear optical transmission (at low power), and (b) RF characterization of mechanical resonating mode ($P_{i,1} < P_{i,2} < P_{i,3}$).

## 6.2 Wideband-tunable resonators using electrostatic actuation

Optical network-on-chip has established itself as a viable alternative to the conventional metal wire interconnection as it enables to drastically increase the total available bandwidth and to reduce the overall interconnect power dissipation. Nevertheless, optical interconnects for intra-chip communications need to meet very stringent power consumption and size requirements to comply with the needs of multi-core processors in future decades [165]. Among the important building blocks of optical networks-on-chip are tunable optical elements. While most of the proposed tunable photonic devices to date are based on carrier dispersion and thermal tuning, they suffer from intrinsic loss and small tuning range (for tuning based on carrier dispersion) or very low tuning speed and high power consumption (for thermal tuning). Among the various approaches for extending the tuning range, the switching speed, and lowering the power consumption, mechanically-tunable photonic devices have proven themselves as promising candidates [166, 167, 168].

Several demonstrations of mechanically tunable photonic devices have been reported [166, 167]. However, most of these devices are based on photonic crystal cavities, which limits their applicability for dense optical networks. Here, an alternative opto-mechanical architecture that enables low-power and wideband tunable micro-optical traveling-wave resonators in double layer silicon material platforms is presented [156, 169].

### 6.2.1 Proposed wideband-tunable devices

Figure 6.10(a) shows the schematic of the proposed tunable microdisk resonators on double-layer SOI platform. The material platform is formed by two thin layers of crystalline Si that are separated by a thin (e.g., 20-100 nm) oxide layer. The development of the double-layer Si platform has been detailed in [156]. The device is realized by patterning the microdisk structure in the double-layer SOI substrate and partially undercutting the thin oxide layer between the upper and lower Si layers (see Fig. 6.10(b)). The top and the bottom Si layers

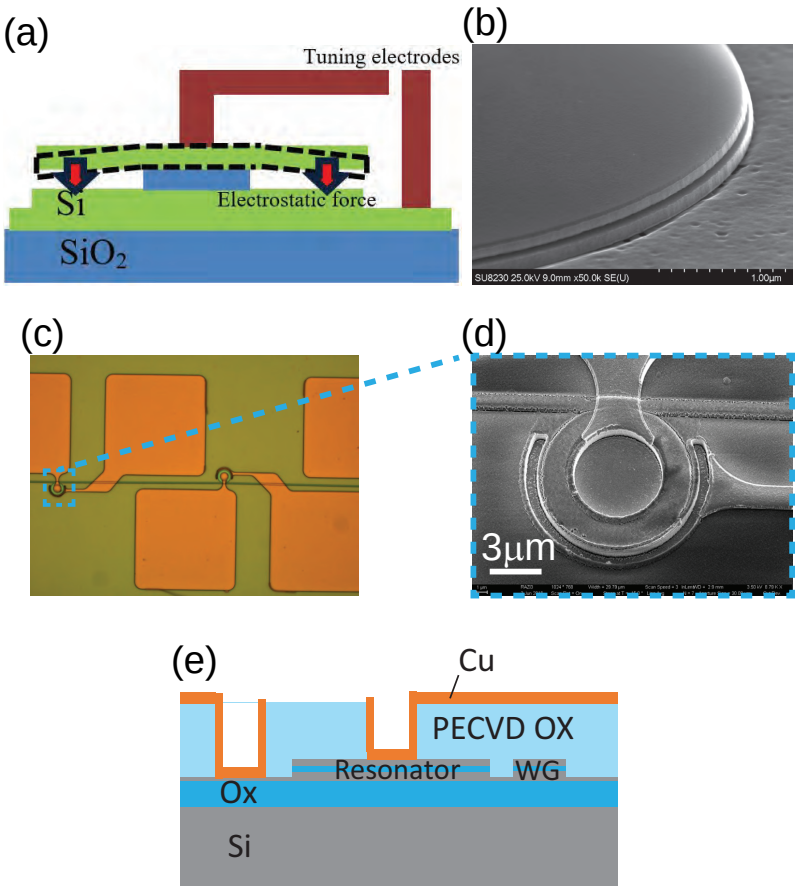


Figure 6.10: An electrostatically actuated wideband tunable optical resonator. (a) The schematic cross section view of the microdisk cavity and the location of the tuning electrodes. The top and bottom Si layers both have 110 nm thickness including a 50 nm pedestal for the bottom layer, with the initial gap of 60 nm. (b) SEM Image of the the fabricated double-layer optomechanical resonator after releasing. (c) and (d) optical and zoom-in SEM of the fabricated double-layer structure along with the electrical pads before releasing. (e) The schematic cross-section of the fabricated structures shown in (c) and (d)

in such an undercut structure form a capacitor with an air dielectric layer, which allows for the movement of the upper Si layer. The resonator wavelength tuning is achieved by changing the size of the gap between the two Si layers. An electric voltage is applied between the upper and the lower Si layers resulting in an attractive electrostatic force between the two capacitor electrodes that pulls the upper Si layer down and reduces the gap (see Fig. 6.10(a)).

### 6.2.2 Theory and simulations

To obtain a high tuning efficiency (defined as the ratio of the wavelength shift ($\Delta\lambda$) to the change in the applied voltage ($\Delta V$), i.e., $\Delta\lambda/\Delta V$), a high sensitivity of the resonance wavelength to the change in the gap size and a relatively strong electrostatic force and/or relatively low structure stiffness for the moving electrode (i.e., the upper Si layer) are required. All of these have been achieved by using the structure proposed here: the vertical slot architecture with the thin air gap (Fig. 6.10(a)), allowing us to concurrently achieve wide tuning bandwidth and a low tuning voltage. Furthermore, the upper electrode is patterned to adjust/reduce its stiffness for the target device tuning range.

The proposed optomechanical structure supports both TE and TM modes (slot-mode) simulated in COMSOL [170]. While the TM mode (i.e., Electrical field normal to the double SOI wafer surface) of the structure provides slightly higher sensitivity to changes in the gap size, my focus is on the TE mode (i.e., Electrical field parallel to the double SOI wafer surface) of the structure as it provides lower loss (i.e., higher quality factors for the optical resonance modes) and allows for more compact resonators with larger free spectral ranges (FSRs). Reducing the gap size results in increasing the $TE_1$ resonance wavelength (Figs. 6.10(a) and 6.10(b), red curves) of the fundamental TE mode (vertically even-mode). While the change in the optical resonance wavelength is almost linearly proportional to the change in the gap, the change in the gap size is a nonlinear function of the applied voltage and depends on the gap size itself. The maximum tuning range is also limited by the pull-in voltage that limits the maximum change in the gap size. As indicated in Figs. 6.11(c) and 6.11(d), 35 nm and 22 nm wavelength shifts can be obtained, respectively, for the structures in Figs. 6.11(a) and 6.11(b) by applying a reasonably small voltage. This shows the unique feature of the proposed structures in providing a very wideband tuning range.

The tuning speed of the proposed electro-statically tunable devices is limited by the mechanical time constant of the moving Si layer, which is in-turn limited by the fundamental flexural resonance frequency ($f_{mech}$) of the double-layer structure. The patterned and

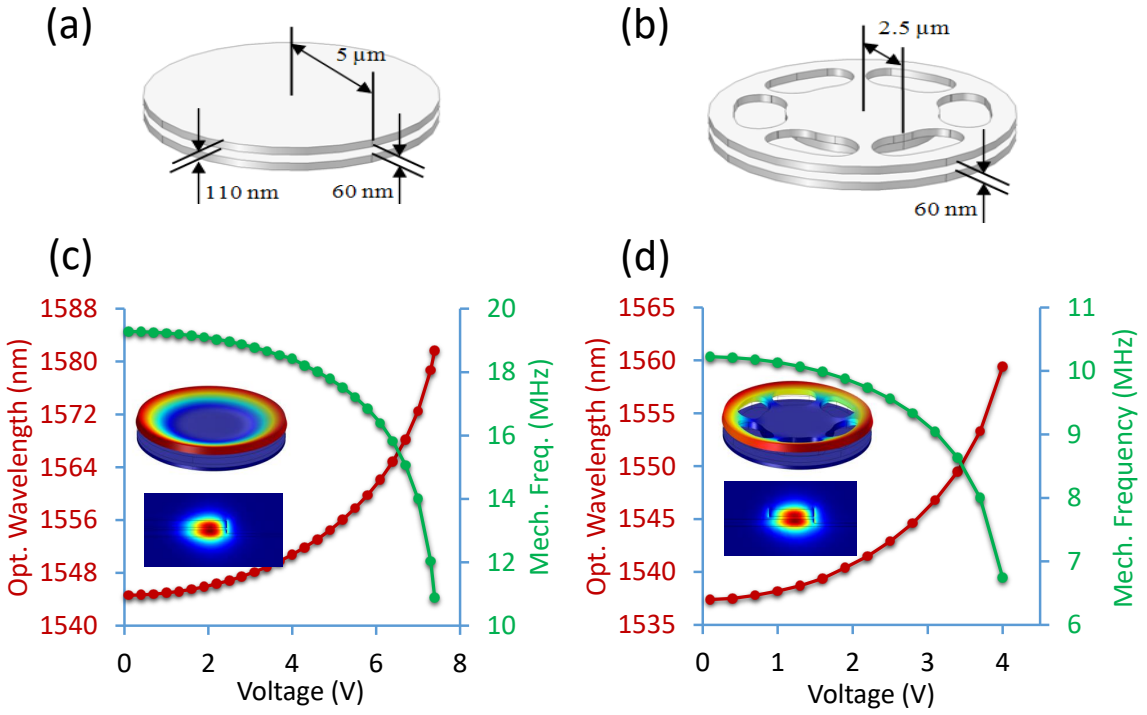


Figure 6.11: (a) and (b): Schematics of the proposed double-layer resonators for wide-band tunable optical resonators. (c) and (d): Variation of the optical wavelength (red curve, left axis) and the resonance frequency of the first mechanical flexural mode (green curve, right axis) as a function of the applied voltage between the two Si layers for a double-layer microdisk shown in 6.11(a) and a double-layer microring shown in 6.11(b), respectively. Schematics shown in 6.11(a) and 6.11(b) scaled for clarity in mode-profile demonstrations.

unpatterned structures exhibit a range of $f_{mech}$ depending on the applied voltage starting at 19 MHz and 10 MHz (corresponding to the rise times, $t_r$, of 19 ns and 35 ns, respectively), respectively for Figs. 6.11(a) and 6.11(b), green curves. One way to increase $f_{mech}$ is to extend the radius of the anchor. For example, simulations show $f_{mech} > 50$ MHz (i.e., $t_r$= 7 ns) when the radii of the anchor and the upper unpatented disk are 3.5 $\mu$m and 5 $\mu$m, respectively, and the thickness of the upper and lower Si layers being 110 nm. This mechanical resonance frequency can result in switching time constant of a few nanoseconds for the optical device. However, increasing the mechanical resonance frequency in this structure comes at the cost of losing the tuning efficiency ($\Delta\lambda/\Delta V$); which in turn can limit the tuning bandwidth for a given operating voltage. This trade-off among the tuning range, the operation voltage, and the tuning speed can be used to design devices for any

desired application by adjusting the stiffness of the upper electrode through tailoring its geometry and pattern.

In addition to the large tuning range and fast tuning speed, the proposed device has a zero static power consumption (due to the capacitive structure) and very small dynamic energy consumption of $< 60$ fJ for tuning through the whole tuning range of 35 nm (based on our simulations). The high Q of the TE-mode resonance of the proposed structures (e.g., Q $>$ 50 k [156] ) also enables very low loss tunable devices. This set of performance measures are by far superior to that of the reported tunable devices based on thermal tuning and carrier dispersion.

# CHAPTER 7
# EPILOGUE

## 7.1 Brief summary of contributions

In this dissertation, I have designed, simulated, fabricated, and characterized integrated phononic devices fabricated on silicon chips, very promising for integrated nano-electromechanical/ optomechanical systems, for enabling novel on-chip sensing and RF/optical signal processing. Here I would like to summarize my main research achievements during the course of my PhD studies.

- I have demonstrated the first platform for phononic crystal (PnC) structures that exhibits high-frequency phononic bandgaps (PnBGs) for surface acoustic waves (SAWs) in a CMOS-compatible all-dielectric pillar-based platform. These SAW-PnCs are formed by a periodic array of non-metallic piezoelectric pillars on a CMOS-compatible AlN-on-Si substrate, which reduces the overall material phononic loss by avoiding metallic pillar-based structures. My experimental results have shown a wideband PnBG (from 1.6 GHz to 1.75 GHz) in the developed PnC platform which has the potential for enabling low-loss phononic devices for any high-frequency applications including wireless communications by proper design modifications.

- I have demonstrated a new design approach for integrated PnC resonators based on confining acoustic waves in a heterogeneous waveguide-based PnC structure. In this architecture, a PnC waveguide that supports a single mode at desired resonance frequencies is terminated by two waveguide sections with no propagating mode at those frequencies (i.e., have mode-gap). This design approach can benefit both membrane-based and SAW-based architectures by confining the mode spreading in the k-domain that leads to reduced loss by minimizing the coupling to the bulk modes.

- I have studied stimulated Brillouin scattering (SBS) in SiN structures, created as a phononic line defect inside a pillar-based PnC membrane for efficient confinement of the generated acoustic phonons to the optical waveguides. The phononic defect is carefully designed to confine the transversally-resonating breathing acoustic modes inside the PnBG of the host PnC. These breathing acoustic modes can be efficiently excited by the fundamental optical modes of the waveguides. The combination of the low-loss traveling photons and the long-lasting resonating phonons in the designed SiN waveguide paves the way for the demonstration of efficient on-chip SBS devices for novel RF-photonics signal processing applications.

- I have demonstrated on-chip optomechanical oscillations in the double-layer Si platforms, enabling novel on-chip RF-photonics signal processing applications. My structures show strong optomechanical interaction owing to the high sensitivity of the resonating optical modes of the structure with respect to the gap size. Thus, these structures are very promising for different classical and quantum optomechanical studies. In addition, my theoretical studies of the double-layer structures reveal that the incorporation of an electrostatic signal for capacitive actuation can enable wide-band high-speed optical switches with high prospect for integrated optical interconnects.

## 7.2 Future directions

Indeed, designing new integrated structures, specially in CMOS-compatible platforms, allows for the co-integration of such structures with existing integrated systems and devices for achieving new on-chip functionalities, which are the natural extension of my PhD works.

On the experimental side, the SBS devices in the membrane SiN PnC are under fabrication and characterization. I am also working on the fabrication of the electrostatically-actuated double-layer structures for the demonstration of wide-band high-speed reconfig-

urable optical devices. A verity of waveguide-based surface phononic resonators are under the fabrication. However, what I would like to highlight here is the investigation of novel SBS-based surface devices fully-compatible with the popular integrated optic platforms. These devices are $Si_3N_4$ waveguides on $SiO_2$ that do not need to be released for achieving the required acoustic confinement, crucial for an efficient SBS process.

### 7.2.1 On-chip surface-based SBS devices

Surface devices have been always and will remain of great interest because of their ease of surface macro-machining and compatibility with the surface-oriented integrated optics devices and electronics. In this dissertation, I have studied membrane-based PnC structures in SiN for SBS demonstration. These structures provides highly-efficient SBS due to the tight co-localization of optical and acoustic waves inside the membrane structures. However, their fabrication is challenging because of the thin fragile SiN membrane in the structure similar to other membrane devices operating at GHz frequencies. Therefore, designing rigid surface structures solves this fabrication difficulty and makes them more suitable for real-world applications. However, the challenge is to find a surface structure compatible with integrated optics platforms that yields the co-localization of both optical and acoustic waves. SiN-on-Ox substrates provide the lowest possible optical loss compared to other popular integrated optics platforms such as SOI platforms. However the challenge in the conventional SiN waveguides on $SiO_2$ is that the generated acoustic wave is not confined to the optical region, which prevents the efficient SBS interaction. This challenge can be solved by either further additional etching of the substrate or creating slot-based surface structures. These devices are currently under investigations.

## REFERENCES


[1] M. Sigalas and E. Economou, "Elastic and acoustic wave band structure," *Journal of Sound and Vibration*, vol. 158, no. 2, pp. 377 –382, 1992.

[2] M. S. Kushwaha, P. Halevi, L. Dobrzynski, and B. Djafari-Rouhani, "Acoustic band structure of periodic elastic composites," *Physical Review Letters*, vol. 71, pp. 2022–2025, 1993.

[3] A. Khelif and A. Adibi, *Phononic crystals: Fundamentals and applications*. Springer, New York, 2016.

[4] J. D. Joannopoulos, S. G. Johnson, J. N. Winn, and R. D. Meade, *Photonic crystals: Molding the flow of light*. Princeton Univ. Press, 2008.

[5] M. Maldovan, "Sound and heat revolutions in phononics," *Nature*, vol. 503, no. 7475, pp. 209–217, 2013.

[6] B. A. Auld, *Acoustic fields and waves in solids*. John Wiley, New York, 1973.

[7] K. Tsubouchi and N. Mikoshiba, "Zero-temperature-coefficient saw devices on aln epitaxial films," *IEEE Transactions on Sonics and Ultrasonics*, vol. 32, no. 5, pp. 634–644, 1985.

[8] J. J. Campbell and W. R. Jones, "A method for estimating optimal crystal cuts and propagation directions for excitation of piezoelectric surface waves," *IEEE Transactions on Sonics and Ultrasonics*, vol. 15, no. 4, pp. 209–217, 1968.

[9] K. A. Ingebrigtsen, "Surface waves in piezoelectrics," *Journal of Applied Physics*, vol. 40, no. 7, pp. 2681–2686, 1969.

[10] P. Hess, "Surface acoustic waves in material science," *Physics Today*, vol. 55, p. 42, 2002.

[11] C. Campbell, *Surface acoustic wave devices for mobile and wireless communications*. Academic press, 1998.

[12] R. Aigner, "Saw and baw technologies for rf filter applications: A review of the relative strengths and weaknesses," in *2008 IEEE Ultrasonics Symposium*, 2008, pp. 582–589.

[13] M. Metcalfe, S. M. Carr, A. Muller, G. S. Solomon, and J. Lawall, "Resolved sideband emission of inas/gaas quantum dots strained by surface acoustic waves," *Physical Review Letters*, vol. 105, p. 037 401, 2010.

[14] M. V. Gustafsson, P. V. Santos, G. Johansson, and P. Delsing, "Local probing of propagating acoustic waves in a gigahertz echo chamber," *Nature Physics*, vol. 8, no. 4, pp. 338–343, 2012.

[15] M. V. Gustafsson, T. Aref, A. F. Kockum, M. K. Ekström, G. Johansson, and P. Delsing, "Propagating phonons coupled to an artificial atom," *Science*, vol. 346, no. 6206, pp. 207–211, 2014.

[16] M. J. A. Schuetz, E. M. Kessler, G. Giedke, L. M. K. Vandersypen, M. D. Lukin, and J. I. Cirac, "Universal quantum transducers based on surface acoustic waves," *Physical Review X*, vol. 5, p. 031 031, 2015.

[17] S.-Y. Yu, X.-C. Sun, X. Ni, Q. Wang, X.-J. Yan, C. He, X.-P. Liu, L. Feng, M.-H. Lu, and Y.-F. Chen, "Surface phononic graphene," *Nature Material*, vol. 15, no. 12, pp. 1243–1247, 2016.

[18] R. Manenti, M. J. Peterer, A. Nersisyan, E. B. Magnusson, A. Patterson, and P. J. Leek, "Surface acoustic wave resonators in the quantum regime," *Physical Review B*, vol. 93, p. 041 411, 2016.

[19] M. M.d.L. J. Santos and P. V., "Modulation of photonic structures by surface acoustic waves," *Reports on Progress in Physics*, vol. 68, no. 7, p. 1639, 2005.

[20] D. A. Fuhrmann, S. M. Thon, H. Kim, D. Bouwmeester, P. M. Petroff, A. Wixforth, and H. J. Krenner, "Dynamic modulation of photonic crystal nanocavities using gigahertz acoustic phonons," *Nature Photonics*, vol. 5, no. 10, pp. 605–609, 2011.

[21] H. Li, S. A. Tadesse, Q. Liu, and M. Li, "Nanophotonic cavity optomechanics with propagating acoustic waves at frequencies up to 12 Ghz," *Optica*, vol. 2, no. 9, pp. 826–831, 2015.

[22] J. W. S. Rayleigh, "Interaction between light and highly confined hypersound in a silicon photonic nanowire," *Proc. London Math. Soc.*, vol. 17, p. 4, 1885.

[23] E. A. Ash, R. M.D. L. Rue, and R. F. Humphryes, "Microsound surface waveguides," *IEEE Transactions on Microwave Theory and Techniques*, vol. 17, no. 11, pp. 882–892, 1969.

[24] M. I. Hussein, M. J. Leamy, and M. Ruzzene, "Dynamics of phononic materials and structures: Historical origins, recent progress, and future outlook," *Applied Mechanics Reviews*, vol. 66, no. 4, 2014.

[25] F. Meseguer, M. Holgado, D. Caballero, N. Benaches, J. Sánchez-Dehesa, C. López, and J. Llinares, "Rayleigh-wave attenuation by a semi-infinite two-dimensional elastic-band-gap crystal," *Physical Review B*, vol. 59, pp. 12 169–12 172, 1999.

[26] T. Gorishnyy, C. K. Ullal, M. Maldovan, G. Fytas, and E. L. Thomas, "Hypersonic phononic crystals," *Physical Review Letters*, vol. 94, p. 115 501, 2005.

[27] S. Mohammadi, A. A. Eftekhar, A. Khelif, W. D. Hunt, and A. Adibi, "Evidence of large high frequency complete phononic band gaps in silicon phononic crystal plates," *Applied Physics Letters*, vol. 92, no. 22, p. 221 905, 2008.

[28] T.-T. Wu, Z.-G. Huang, T.-C. Tsai, and T.-C. Wu, "Evidence of complete band gap and resonances in a plate with periodic stubbed surface," *Applied Physics Letters*, vol. 93, no. 11, p. 111 902, 2008.

[29] Y. Pennec, B. Djafari Rouhani, H. Larabi, A. Akjouj, J. N. Gillet, J. O. Vasseur, and G. Thabet, "Phonon transport and waveguiding in a phononic crystal made up of cylindrical dots on a thin homogeneous plate," *Physical Review B*, vol. 80, p. 144 302, 2009.

[30] M. Oudich, Y. Li, B. M. Assouar, and Z. Hou, "A sonic band gap based on the locally resonant phononic plates with stubs," *New Journal of Physics*, vol. 12, no. 8, p. 083 049, 2010.

[31] R. Pourabolghasem, A. Khelif, S. Mohammadi, A. Eftekhar, and A. Adibi, "Physics of band-gap formation and its evolution in the pillar-based phononic crystal structures," *Journal of Applied Physics*, vol. 116, p. 013 514, 2014.

[32] Z. Liu, X. Zhang, Y. Mao, Y. Y. Zhu, Z. Yang, C. T. Chan, and P. Sheng, "Locally resonant sonic materials," *Science*, vol. 289, no. 5485, pp. 1734–1736, 2000.

[33] R. Pourabolghasem, S. Mohammadi, A. Eftekhar, A. Khelif, and A. Adibi, "Experimental evidence of high-frequency complete elastic bandgap in pillar-based phononic slabs," *Applied Physics Letters*, vol. 105, no. 23, p. 231 908, 2014.

[34] S. Mohammadi, A. A. Eftekhar, W. D. Hunt, and A. Adibi, "High-q micromechanical resonators in a two-dimensional phononic crystal slab," *Applied Physics Letters*, vol. 94, no. 5, p. 051 906, 2009.

[35] S. Mohammadi and A. Adibi, "Waveguide-based phononic crystal micro/ nanomechanical high-Q resonators," *Journal of Microelectromechanical Systems*, vol. 21, no. 2, pp. 379–384, 2012.

[36] A. Khelif, A. Choujaa, S. Benchabane, B. Djafari-Rouhani, and V. Laude, "Guiding and bending of acoustic waves in highly confined phononic crystal waveguides," *Applied Physics Letters*, vol. 84, no. 22, pp. 4400–4402, 2004.

[37] J.-H. Sun and T.-T. Wu, "Propagation of acoustic waves in phononic-crystal plates and waveguides using a finite-difference time-domain method," *Physical Review B*, vol. 76, p. 104 304, 2007.

[38] S. Mohammadi and A. Adibi, "On chip complex signal processing devices using coupled phononic crystal slab resonators and waveguides," *AIP Advances*, vol. 1, no. 4, p. 041 903, 2011.

[39] C. T. C. Nguyen, "Mems technology for timing and frequency control," in *Proceedings of the 2005 IEEE International Frequency Control Symposium and Exposition, 2005.*, 2005, 11 pp.–.

[40] T. Alegre, A. Safavi-Naeini, M. Winger, and O. Painter, "Quasi-two-dimensional optomechanical crystals with a complete phononic bandgap," *Optics Express*, vol. 19, no. 6, pp. 5658–5669, 2011.

[41] K. E. Grutter, M. Davanco, and K. Srinivasan, "Si3n4 nanobeam optomechanical crystals," *IEEE Journal of Selected Topics in Quantum Electronics*, vol. 21, p. 4, 2015.

[42] R. Martínez-Sala, J. Sancho, J. V. Sánchez, V. Gómez, J. Llinares, and F. Meseguer, "Sound attenuation by sculpture," *Nature*, vol. 378, p. 241, 1995.

[43] R. Pourabolghasem, R. Dehghannasiri, A. A. Eftekhar, and A. Adibi, "Waveguiding effect in the gigahertz frequency range in pillar-based phononic-crystal slabs," *Physical Review Applied*, vol. 9, p. 014 013, 2018.

[44] J.-K. Yu, S. Mitrovic, D. Tham, J. Varghese, and J. R. Heath, "Reduction of thermal conductivity in phononic nanomesh structures," *Nature Nanotechnology*, vol. 5, pp. 718–721, 2010.

[45] S. Benchabane, A. Khelif, J.-Y. Rauch, L. Robert, and V. Laude, "Evidence for complete surface wave band gap in a piezoelectric phononic crystal," *Physical Review E*, vol. 73, p. 065 601, 2006.

[46] T.-T. Wu, L.-C. Wu, and Z.-G. Huang, "Frequency band-gap measurement of two-dimensional air/silicon phononic crystals using layered slanted finger interdigital transducers," *Journal of Applied Physics*, vol. 97, no. 9, p. 094 916, 2005.

[47] D. Yudistira, A. Boes, B. Graczykowski, F. Alzina, L. Y. Yeo, C. M. Sotomayor Torres, and A. Mitchell, "Nanoscale pillar hypersonic surface phononic crystals," *Physical Review B*, vol. 94, p. 094 304, 2016.

[48] B. J. Ash, S. R. Worsfold, P. Vukusic, and G. R. Nash, "A highly attenuating and frequency tailorable annular hole phononic crystal for surface acoustic waves," *Nature Communications*, vol. 8, no. 1, p. 174, 2017.

[49] H. Lee, T. Chen, J. Li, K. Y. Yang, S. Jeon, O. Painter, and K. J. Vahala, "Chemically etched ultrahigh-q wedge-resonator on a silicon chip," *Nature Photonics*, vol. 6, no. 369, 2012.

[50] H. Shin, W. Qiu, R. Jarecki, J. A. Cox, R. H. O. III, A. Starbuck, Z. Wang, and P. T. Rakich, "Tailorable stimulated brillouin scattering in nanoscale silicon waveguides," *Nature Communications*, vol. 4, no. 1944, 2013.

[51] R. Pant, C. G. Poulton, D. Y. Choi, H. Mcfarlane, S. Hile, E. Li, L. Thevenaz, B. Luther-Davies, S. J. Madden, and B. J. Eggleton, "On-chip stimulated brillouin scattering," *Optics Express*, vol. 19, p. 8285, 2011.

[52] P. Dainese1, P. S. J. Russell, N. Joly, J. C. Knight, G. S. Wiederhecker, H. L. Fragnito, V. Laude, and A. Khelif, "Stimulated brillouin scattering from multi-ghz-guided acoustic phonons in nanostructured photonic crystal fibres," *Nature Physics*, vol. 2, p. 388, 2006.

[53] M. S. Kang, A. Nazarkin, A. Brenn, and P. S. J. Russell, "Tightly trapped acoustic phonons in photonic crystal fibres as highly nonlinear artificial raman oscillators," *Nature Physics*, vol. 5, p. 276, 2009.

[54] R. V. Laer, B. Kuyken, D. V. Thourhout, and R. Baets, "Interaction between light and highly confined hypersound in a silicon photonic nanowire," *Nature Photonics*, vol. 9, p. 199, 2015.

[55] I. S. Grudinin, A. B. Matsko, and L. Maleki, "Brillouin lasing with a caf2 whispering gallery mode resonator," *Physical Review Letters*, vol. 102, p. 043 902, 2009.

[56] E. Ippen and R. Stolen, "Stimulated brillouin scattering in optical fibers," *Applied Physics Letters*, vol. 21, p. 539, 1972.

[57] A. R. Chraplyvy, "Limitations on lightwave communications imposed by optical-fiber nonlinearities," *Journal of Lightwave Technology*, vol. 8, no. 10, pp. 1548–1557, 1990.

[58] S. P. Smith, F. Zarinetchi, and S. Ezekiel, "Narrow-linewidth stimulated brillouin fiber laser and applications," *Optics Letters*, vol. 16, no. 393, 1991.

[59] F. Zarinetchi, S. P. Smith, and S. Ezekiel, "Stimulated brillouin fiber-optic laser gyroscope," *Optics Letters*, vol. 16, no. 229, 1991.

[60] Y. Okawachi, J. E. S. M. S. Bigelow, Z. Zhu, A. Schweinsberg, D. J. Gauthier, R. W. Boyd, and A. L. Gaeta, "Tunable all-optical delays via brillouin slow light in an optical fiber," *Physical Review Letters*, vol. 94, p. 153 902, 2005.

[61] Z. Zhu, D. J. Gauthier, and R. W. Boyd, "Stored light in an optical fiber via stimulated brillouin scattering," *Science*, vol. 318, p. 1748, 2007.

[62] T. F. S. Bttner, I. V. Kabakova, D. D. Hudson, R. Pant, C. G. Poulton, A. C. Judge, and B. J. Eggleton, "Phase-locking and pulse generation in multi-frequency brillouin oscillator via four wave mixing," *Scientific Reports*, vol. 4, p. 5032, 2014.

[63] H. Shin, J. A. Cox, R. Jarecki, A. Starbuck, Z. Wang, and P. T. Rakich, "Control of coherent information via on-chip photonicphononic emitterreceivers," *Nature Communications*, vol. 6, no. 6427, 2015.

[64] M. Tomes and T. Carmon, "Photonic micro-electromechanical systems vibrating at $x$-band (11-ghz) rates," *Physical Review Letters*, vol. 102, p. 113 601, 2009.

[65] W. Loh, A. A. S. Green, F. N. Baynes, D. C. Cole, F. J. Quinlan, H. Lee, K. J. Vahala, S. B. Papp, and S. A. Diddams, "Dual-microcavity narrow-linewidth brillouin laser," *Optica*, vol. 2, p. 225, 2015.

[66] D. J. Wilson, C. A. Regal, S. B. Papp, and H. J. Kimble, "Cavity optomechanics with stoichiometric sin films," *Physical Review Letters*, vol. 103, p. 207 204, 2009.

[67] H. Rokhsari, T. J. Kippenberg, T. Carmon, and K. J. Vahala, "Radiation-pressure-driven micro-mechanical oscillator," *Opt. Express*, vol. 13, no. 14, pp. 5293–5301, 2005.

[68] A. Cho, "To physicists' surprise, a light touch sets tiny objects aquiver," *Science*, vol. 309, no. 5733, pp. 366–366, 2005.

[69] K. J. Vahala, "Optical microcavities," *Nature*, vol. 424, p. 839, 2003.

[70] A. Cho, "Putting light's light touch to work as optics meets mechanics," *Science*, vol. 328, no. 5980, pp. 812–813, 2010.

[71] D. K. Armani, T. J. Kippenberg, S. M. Spillane, and K. J. Vahala, "Ultra-high-q toroid microcavity on a chip," *Nature*, vol. 421, p. 925, 2003.

[72] G. S. Wiederhecker, L. Chen, A. Gondarenko, and M. Lipson, "Controlling photonic structures using optical forces," *Nature*, vol. 462, p. 633, 2009.

[73] J. Rosenberg, Q. Lin, and O. Painter, "Static and dynamic wavelength routing via the gradient optical force," *Nature Photonics*, vol. 3, p. 478, 2009.

[74] R. Ma, A. Schliesser, P. Del'Haye, A. Dabirian, G. Anetsberger, and T. J. Kippenberg, "Radiation-pressure-driven vibrational modes in ultrahigh-q silica microspheres," *Opt. Lett.*, vol. 32, no. 15, pp. 2200–2202, 2007.

[75] G. Anetsberger, R. Rivière, A. Schliesser, O. Arcizet, and T. J. Kippenberg, "Ultralow-dissipation optomechanical resonators on a chip," *Nature Photonics*, vol. 2, p. 627, 2008.

[76] A. H. Safavi-Naeini, T. P. M. Alegre, J. Chan, M. Eichenfield, M. Winger, Q. Lin, J. T. Hill, D. E. Chang, and O. Painter, "Electromagnetically induced transparency and slow light with optomechanics," *Nature*, vol. 472, p. 69, 2011.

[77] A. Schliesser, R. Riviere, G. Anetsberger, O. Arcizet, and T. J. Kippenberg, "Resolved-sideband cooling of a micromechanical oscillator," *Nature Physics*, vol. 4, no. 5, pp. 415–419, 2008.

[78] J. Chan, T. P. M. Alegre, A. H. Safavi-Naeini, J. T. Hill, A. Krause, S. Gröblacher, M. Aspelmeyer, and O. Painter, "Laser cooling of a nanomechanical oscillator into its quantum ground state," *Nature*, vol. 478, p. 89, 2011.

[79] A. H. Safavi-Naeini, S. Gröblacher, J. T. Hill, J. Chan, M. Aspelmeyer, and O. Painter, "Squeezed light from a silicon micromechanical resonator," *Nature*, vol. 500, p. 185, 2013.

[80] T. J. Kippenberg, H. Rokhsari, T. Carmon, A. Scherer, and K. J. Vahala, "Analysis of radiation-pressure induced mechanical oscillation of an optical microcavity," *Phys. Rev. Lett.*, vol. 95, p. 033 901, 2005.

[81] M. Hossein-Zadeh, H. Rokhsari, A. Hajimiri, and K. J. Vahala, "Characterization of a radiation-pressure-driven micromechanical oscillator," *Phys. Rev. A*, vol. 74, p. 023 813, 2006.

[82] A. G. Krause, M. Winger, T. D. Blasius, Q. Lin, and O. Painter, "A high-resolution microchip optomechanical accelerometer," *Nature Photonics*, vol. 6, p. 768, 2012.

[83] M. Eichenfield, J. Chan, R. M. Camacho, K. J. Vahala, and O. Painter, "Optomechanical crystals," *Nature*, vol. 462, no. 7269, pp. 78–82, 2009.

[84] Y. Tanaka and S.-i. Tamura, "Surface acoustic waves in two-dimensional periodic elastic structures," *Physical Review. B*, vol. 58, pp. 7958–7965, 1998.

[85] T.-T. Wu, Z. Huang, and S. Lin, "Surface and bulk acoustic waves in two-dimensional phononic crystal consisting of materials with general anisotropy," *Physical Review B*, vol. 69, p. 094 301, 2004.

[86] V. Laude, M. Wilm, S. Benchabane, and A. Khelif, "Full band gap for surface acoustic waves in a piezoelectric phononic crystal," *Physical Review E*, vol. 71, p. 036 607, 2005.

[87] A. Khelif, Y. Achaoui, S. Benchabane, V. Laude, and B. Aoubiza, "Locally resonant surface acoustic wave band gaps in a two-dimensional phononic crystal of pillars on a surface," *Physical Review B*, vol. 81, p. 214 303, 2010.

[88] Y. Achaoui, A. Khelif, S. Benchabane, L. Robert, and V. Laude, "Experimental observation of locally-resonant and bragg band gaps for surface guided waves in a phononic crystal of pillars," *Physical Review B*, vol. 83, p. 104 201, 2011.

[89] M. Oudich and M. B. Assouar, "Surface acoustic wave band gaps in a diamond-based two-dimensional locally resonant phononic crystal for high frequency applications," *Journal of Applied Physics*, vol. 111, no. 1, p. 014 504, 2012.

[90] A. Khelif, Y. Achaoui, and B. Aoubiza, "Surface acoustic waves in pillars-based two-dimensional phononic structures with different lattice symmetries," *Journal of Applied Physics*, vol. 112, no. 3, p. 033 511, 2012.

[91] B. Graczykowski, S. Mielcarek, A. Trzaskowska, J. Sarkar, P. Hakonen, and B. Mroz, "Tuning of a hypersonic surface phononic band gap using a nanoscale two-dimensional lattice of pillars," *Physical Review B*, vol. 86, p. 085 426, 2012.

[92] J. V. Sánchez-Pérez, D. Caballero, R. Mártinez-Sala, C. Rubio, J. Sánchez-Dehesa, F. Meseguer, J. Llinares, and F. Gálvez, "Sound attenuation by a two-dimensional array of rigid cylinders," *Physical Review Letters*, vol. 80, pp. 5325–5328, 1998.

[93] R. Dehghannasiri, R. Pourabolghasem, A. A. Eftekhar, and A. Adibi, "Integrated phononic crystal resonators based on adiabatically-terminated phononic crystal waveguides," *AIP Advances*, vol. 6, no. 12, p. 121 603, 2016.

[94] J. Segovia-Fernandez and G. Piazza, "Thermoelastic damping in the electrodes determines $q$ of aln contour mode resonators," *Journal of Microelectromechanical Systems*, vol. 26, no. 3, pp. 550–558, 2017.

[95] M. F. Ashby, *Materials selection in mechanical design*. Butterworth-Heinemann, 2005.

[96] A. N. Cleland, *Foundations of nanomechanics*. Springer Science & Business Media, 2013.

[97] S. Ghaffari and T. W. Kenny, *Resonant mems: Fundamentals, implementation, and application*. Wiley, Weinheim, Germany, 2015, pp. 55–71.

[98] C. Zener, "Internal friction in solids ii. general theory of thermoelastic internal friction," *Physical Review*, vol. 53, pp. 90–99, 1938.

[99] C. Zener, *Elasticity and anelasticity of metals*. University of Chicago press, 1948.

[100] A. S. Nowick and B. S. Berry, *Anelastic relaxation in crystalline solids*. Academic Press, 1972, vol. 1.

[101] L. Landau and E. Lifshitz, *Theory of elasticity (3rd edition)*. Pergamon Press, Oxford, 1995.

[102] R. Lifshitz and M. L. Roukes, "Thermoelastic damping in micro- and nanomechanical systems," *Physical Review B*, vol. 61, pp. 5600–5609, 2000.

[103] S. K. De and N. R. Aluru, "Theory of thermoelastic damping in electrostatically actuated microstructures," *Physical Review B*, vol. 74, p. 144 305, 2006.

[104] S. Vengallatore, "Analysis of thermoelastic damping in laminated composite micromechanical beam resonators," *Journal of Micromechanics and Microengineering*, vol. 15, no. 12, p. 2398, 2005.

[105] W. P. Mason and H. E. Bommel, "Ultrasonic attenuation at low temperatures for metals in the normal and superconducting states," *The Journal of the Acoustical Society of America*, vol. 28, no. 5, pp. 930–943, 1956.

[106] A. Frangi, M. Cremonesi, A. Jaakkola, and T. Pensala, "Analysis of anchor and interface losses in piezoelectric mems resonators," *Sensors and Actuators A: Physical*, vol. 190, pp. 127 –135, 2013.

[107] L. W. Hung and C. T. C. Nguyen, "Capacitive-piezoelectric transducers for high- $q$ micromechanical aln resonators," *Journal of Microelectromechanical Systems*, vol. 24, no. 2, pp. 458–473, 2015.

[108] R. M. White and F. W. Voltmer, "Direct piezoelectric coupling to surface elastic waves," *Applied Physics Letters*, vol. 7, no. 12, pp. 314–316, 1965.

[109] G. Piazza, V. Felmetsger, P. Muralt, R. H. Olsson III, and R. Ruby, "Piezoelectric aluminum nitride thin films for microelectromechanical systems," *MRS bulletin*, vol. 37, no. 11, pp. 1051–1061, 2012.

[110] H. Bhugra and G. Piazza, *Piezoelectric mems resonators*. Springer, 2017.

[111] J. Bochmann, A. Vainsencher, D. D. Awschalom, and A. N. Cleland, "Nanomechanical coupling between microwave and optical photons," *Nature Physics*, vol. 9, no. 11, pp. 712–716, 2013.

[112] K. C. Balram, M. I. Davanço, J. D. Song, and K. Srinivasan, "Coherent coupling between radiofrequency, optical and acoustic waves in piezo-optomechanical circuits," *Nature Photonics*, vol. 10, no. 5, pp. 346–352, 2016.

[113] C. K. Campbell, Y. Ye, and J. J. S. Papa, "Wide-band linear phase saw filter design using slanted transducer fingers," *IEEE Transaction on Sonics and Ultrasonics*, vol. 29, no. 4, pp. 224–228, 1982.

[114] H. Yatsuda, "Design techniques for saw filters using slanted finger interdigital transducers," *IEEE Transaction on Ultrasonics, Ferroelectrics, and Frequency Control*, vol. 44, no. 2, pp. 453–459, 1997.

[115] C. Xiong, W. H. P. Pernice, and H. X. Tang, "Low-loss, silicon integrated, aluminum nitride photonic circuits and their use for electro-optic signal processing," *Nano Letters*, vol. 12, no. 7, pp. 3562–3568, 2012.

[116] J. H. Visser and A. Venema, "Silicon saw devices and electromagnetic feedthrough," in *IEEE 1988 Ultrasonics Symposium Proceedings.*, 1988, 297–301 vol.1.

[117] D. Morgan, *Surface acoustic wave filters: With applications to electronic communications and signal processing*. Academic Press, 2010.

[118] L. Y. Yeo and J. R. Friend, "Surface acoustic wave microfluidics," *Annual Review of Fluid Mechanics*, vol. 46, no. 1, pp. 379–406, 2014.

[119] B. Drafts, "Acoustic wave technology sensors," *IEEE Transactions on Microwave Theory and Techniques*, vol. 49, no. 4, pp. 795–802, 2001.

[120] K. Länge, B. E. Rapp, and M. Rapp, "Surface acoustic wave biosensors: A review," *Analytical and Bioanalytical Chemistry*, vol. 391, no. 5, pp. 1509–1519, 2008.

[121] T. Sakuma and Y. Kawanami, "Theory of the surface acoustic soliton. i. insulating solid," *Physical Review B*, vol. 29, pp. 869–879, 1984.

[122] A. P. Mayer, "Surface acoustic waves in nonlinear elastic media," *Physics Reports*, vol. 256, no. 4, pp. 237 –366, 1995.

[123] A. A. Oliner, "Waveguides for acoustic surface waves: A review," *Proceedings of the IEEE*, vol. 64, no. 5, pp. 615–627, 1976.

[124] I. M. Mason, R. M. de la Rue, R. V. Schmidt, E. A. Ash, and P. E. Lagasse, "Ridge guides for acoustic surface waves," *Electronics Letters*, vol. 7, no. 14, pp. 395–397, 1971.

[125] S. V. Biryukov, Y. V. Gulyaev, V. V. Krylov, and V. P. Plessky, *Surface acoustic waves in inhomogeneous media*. Springer-Verlag Berlin Heidelberg, 1995.

[126] S. Mahon and R. Aigner, "Bulk acoustic wave devices–why, how, and where they are going," in *CS Mantech Conference*, 2007, pp. 15–18.

[127] R. Ruby, "Review and comparison of bulk acoustic wave fbar, smr technology," in *2007 IEEE Ultrasonics Symposium Proceedings*, 2007, pp. 1029–1040.

[128] D. Neculoiu, A. Muller, G. Deligeorgis, A. Dinescu, A. Stavrinidis, D. Vasilache, A. M. Cismaru, G. E. Stan, and G. Konstantinidis, "Ain on silicon based surface acoustic wave resonators operating at 5 ghz," *Electronics Letters*, vol. 45, no. 23, pp. 1196–1197, 2009.

[129] R. C. Ruby, P. Bradley, Y. Oshmyansky, A. Chien, and J. D. Larson, "Thin film bulk wave acoustic resonators (fbar) for wireless applications," in *2001 IEEE Ultrasonics Symposium. Proceedings. An International Symposium (Cat. No.01CH37263)*, vol. 1, 2001, 813–821 vol.1.

[130] G. Piazza, P. J. Stephanou, and A. P. Pisano, "Single-chip multiple-frequency aln mems filters based on contour-mode piezoelectric resonators," *Journal of Microelectromechanical Systems*, vol. 16, no. 2, pp. 319–328, 2007.

[131] S. G. Johnson, P. R. Villeneuve, S. Fan, and J. D. Joannopoulos, "Linear waveguides in photonic-crystal slabs," *Physical Review B*, vol. 62, pp. 8212–8222, 2000.

[132] Y. Akahane, T. Asano, B.-S. Song, and S. Noda, "High-q photonic nanocavity in a two-dimensional photonic crystal," *Nature*, vol. 425, p. 944, 2003.

[133] B.-S. Song, S. Noda, T. Asano, and Y. Akahane, "Ultra-high-q photonic double-heterostructure nanocavity," *Nature Material*, vol. 4, no. 3, pp. 207–210, 2005.

[134] R. Dehghannasiri, R. Pourabolghasem, A. A. Eftekhar, and A. Adibi, "Ghz heterogeneous phononic crystal slab resonators," in *ASME International Mechanical Engineering Congress and Exposition*, 2015.

[135] R. Dehghannasiri, A. A. Eftekhar, and A. Adibi, "Raman-like stimulated brillouin scattering in sin waveguides," in *2016 Conference on Lasers and Electro-Optics (CLEO)*, 2016, pp. 1–2.

[136] R. Dehghannasiri, A. A. Eftekhar, and A. Adibi, "Raman-like stimulated brillouin scattering in phononic-crystal-assisted silicon-nitride waveguides," *Phys. Rev. A*, vol. 96, p. 053 836, 2017.

[137] R. Y. Chiao, C. H. Townes, and B. P. Stoicheff, "Stimulated brillouin scattering and coherent generation of intense hypersonic waves," *Physical Review Letters*, vol. 12, no. 592, 1964.

[138] J. Li, H. Lee, and K. J. Vahala, "Low-noise brillouin laser on a chip at 1064nm," *Optics Letters*, vol. 39, p. 287, 2014.

[139] J. Kim, M. C. Kuzyk, K. Han, H. Wang, and G. Bahl, "Non-reciprocal brillouin scattering induced transparency," *Nature Physics*, vol. 11, no. 275, 2015.

[140] M. S. Kang, A. Butsch, and P. S. J. Russell, "Reconfigurable light-driven opto-acoustic isolators in photonic crystal fibre," *Nature Photonics*, vol. 5, no. 549, 2011.

[141] D. Braje, L. Hollberg, and S. Diddams, "Brillouin-enhanced hyperparametric generation of an optical frequency comb in a monolithic highly nonlinear fiber cavity pumped by a cw laser," *Physical Review Letters*, vol. 102, p. 193 902, 2009.

[142] R. Pant, E. Li, D.-Y. Choi, C. G. Poulton, S. J. Madden, B. Luther-Davies, and B. J. Eggleton, "Cavity enhanced stimulated brillouin scattering in an optical chip for multiorder stokes generation," *Optics Letters*, vol. 36, no. 18, pp. 3687–3689, 2011.

[143] L .Thvenaz, "Slow and fast light in optical fibres," *Nature Photonics*, vol. 2, p. 474, 2008.

[144] J. Li, X. Yi, H. Lee, S. A. Diddams, and K. J. Vahala, "Electro-optical frequency division and stable microwave synthesis," *Science*, vol. 345, no. 309, 2014.

[145] P. T. Rakich, C. Reinke, R. Camacho, P. Davids, and Z. Wang, "Giant enhancement of stimulated brillouin scattering in the subwavelength limit," *Physical Review X*, vol. 2, no. 011008, 2012.

[146] W. Qiu, P. T. Rakich, H. Shin, H. Dong, M. Soljai, and Z. Wang, "Stimulated brillouin scattering in nanoscale silicon step-index waveguides: A general framework of selection rules and calculating sbs gain," *Optics Express*, vol. 21, no. 31402, 2013.

[147] E. A. Kittlaus, H. Shin, and P. T. Rakich, "Large brillouin amplification in silicon," *Nature Photonics*, vol. 10, no. 7, pp. 463–467, 2016.

[148] C. Wolff, P. Gutsche, M. J. Steel, B. J. Eggleton, and C. G. Poulton, "Impact of nonlinear loss on stimulated brillouin scattering," *Journal of the Optical Society of America B*, vol. 32, no. 9, pp. 1968–1978, 2015.

[149] Q. Li, A. A. Eftekhar, M. Sodagar, Z. Xia, A. H. Atabaki, and A. Adibi, "Vertical integration of high-q silicon nitride microresonators into silicon-on-insulator platform," *Optics Express*, vol. 21, p. 18 236, 2013.

[150] T. J. Kippenberg, A Schliesser, and M. L. Gorodetsky, "Phase noise measurement of external cavity diode lasers and implications for optomechanical sideband cooling of ghz mechanical modes," *New Journal of Physics*, vol. 15, no. 1, p. 015 019, 2013.

[151] S. S. Verbridge, J. M. Parpia, R. B. Reichenbach, L. M. Bellan, and H. G. Craighead, "High quality factor resonance at room temperature with nanostrings under high tensile stress," *Journal of Applied Physics*, vol. 99, no. 12, p. 124 304, 2006.

[152] S. S. Verbridge, H. G. Craighead, and J. M. Parpia, "A megahertz nanomechanical resonator with room temperature quality factor over a million," *Applied Physics Letters*, vol. 92, no. 1, p. 013 112, 2008.

[153] M. Yuan, M. A. Cohen, and G. A. Steele, "Silicon nitride membrane resonators at millikelvin temperatures with quality factors exceeding 108," *Applied Physics Letters*, vol. 107, no. 26, p. 263 501, 2015.

[154] R. W. Boyd, *Nonlinear optics*. Academic, San Diego, 1992.

[155] A. Kobyakov, M. Sauer, and D. Chowdhury, "Stimulated brillouin scattering in optical fibers," *Adv. Opt. Photon.*, vol. 2, no. 1, pp. 1–59, 2010.

[156] H. Moradinejad, A. H. Atabaki, A. H. Hosseinnia, A. A. Eftekhar, and A. Adibi, "Double-layer crystalline silicon on insulator material platform for integrated photonic applications," *IEEE Photonics Journal*, vol. 6, no. 6, pp. 1–8, 2014.

[157] T. Kippenberg and K. Vahala, "Cavity opto-mechanics," *Opt. Express*, vol. 15, no. 25, pp. 17 172–17 205, 2007.

[158] M. Aspelmeyer, T. J. Kippenberg, and F. Marquardt, "Cavity optomechanics," *Rev. Mod. Phys.*, vol. 86, pp. 1391–1452, 2014.

[159] M. Hossein-Zadeh and K. J. Vahala, "Photonic rf down-converter based on optomechanical oscillation," *IEEE Photonics Technology Letters*, vol. 20, no. 4, pp. 234–236, 2008.

[160] M. L. Povinelli, S. G. Johnson, M. Lončar, M. Ibanescu, E. J. Smythe, F. Capasso, and J. D. Joannopoulos, "High-q enhancement of attractive and repulsive optical forces between coupled whispering-gallery-mode resonators," *Opt. Express*, vol. 13, no. 20, pp. 8286–8295, 2005.

[161] M. L. Povinelli, M. Lončar, M. Ibanescu, E. J. Smythe, S. G. Johnson, F. Capasso, and J. D. Joannopoulos, "Evanescent-wave bonding between optical waveguides," *Optics Letters*, vol. 30, no. 22, pp. 3042–3044, 2005.

[162] I. Favero and K. Karrai, "Optomechanics of deformable optical cavities," *Nature Photonics*, vol. 3, p. 201, 2009.

[163] H. Moradinejad, M. Askari, A. H. Atabaki, Z. Xia, A. A. Eftekhar, and A. Adibi, "Miniaturized high-q silicon nitride resonators at visible wavelengths," in *2017 IEEE Photonics Conference (IPC)*, 2017, pp. 217–218.

[164] Q. Lin, J. Rosenberg, X. Jiang, K. J. Vahala, and O. Painter, "Mechanical oscillation and cooling actuated by the optical gradient force," *Phys. Rev. Lett.*, vol. 103, p. 103 601, 2009.

[165] D. A. B. Miller, "Device requirements for optical interconnects to silicon chips," *Proceedings of the IEEE*, vol. 97, no. 7, pp. 1166–1185, 2009.

[166] R. Perahia, J. D. Cohen, S. Meenehan, T. P. M. Alegre, and O. Painter, "Electrostatically tunable optomechanical zipper cavity laser," *Applied Physics Letters*, vol. 97, no. 19, p. 191 112, 2010.

[167] I. W. Frank, P. B. Deotare, M. W. McCutcheon, and M. Lončar, "Programmable photonic crystal nanobeam cavities," *Opt. Express*, vol. 18, no. 8, pp. 8705–8712, 2010.

[168] H. Cai, B. Dong, J. F. Tao, L. Ding, J. M. Tsai, G. Q. Lo, A. Q. Liu, and D. L. Kwong, "A nanoelectromechanical systems optical switch driven by optical gradient force," *Applied Physics Letters*, vol. 102, no. 2, p. 023 103, 2013.

[169] R. Dehghannasiri, A. A. Eftekhar, M. Sodagar, and A. Adibi, "Wideband-tunable optical resonators on double-layer soi platforms using electrostatic actuation," in *2014 Conference on Lasers and Electro-Optics (CLEO) - Laser Science to Photonic Applications*, 2014, pp. 1–2.

[170] R. Dehghannasiri, M. Soltani, and A. Adibi, "Efficient finite-element formulation for analysis of whispering-gallery-mode optical resonators," *J. Opt. Soc. Am. B*, vol. 34, no. 10, pp. 2259–2265, 2017.

# VITA

Razi Dehghannasiri earned his B.Sc. degree in Electrical Engineering from University of Tehran, Iran in 2011. He joined the Photonics Research Group at Georgia Tech in Fall 2012. In 2014, he earned his M.Sc. in Electrical Engineering with minor in physics. His research interests include integrated phononic crystal devices, optomechanical devices, and integrated photonic devices. He received the Colonel Oscar P. Cleaver Award for ranking first in the ECE Ph.D. preliminary exam in Fall 2012 at Georgia Tech. He is also the recipient of the Georgia Tech President's Fellowship and the NSF Honorable Mention.